Adsorption of Surfactants and Mixed Surfactants at the Hydrophilic Silica/Water Interface Studied Using Total Internal Reflection Raman Spectroscopy and Target Factor Analysis

---

A Dissertation Presented to

the Faculty of the Department of Chemistry

University of Houston

In Partial Fulfillment

of the Requirements for the Degree

Doctor of Philosophy

By

Dien Ngo

December 2016

Adsorption of Surfactants and Mixed Surfactants at the Hydrophilic Silica/Water Interface Studied Using Total Internal Reflection Raman Spectroscopy and Target Factor Analysis

Dien Ngo

APPROVED:

Dr. Steven Baldelli, Chairman

Dr. Jeremy May

Dr. Ding-Shyue (Jerry) Yang

Dr. Shoujun Xu

Dr. Stephen T. Wong

Dean, College of Natural Sciences and Mathematics

Acknowledgements

I would like to thank

- my advisor, Professor Baldelli, for his support and guidance;
- Dr. Zlata for her support when I started using TIR Raman spectroscopy in my study;
- Michelle and Daniela for editing and proofreading my dissertation;
- the Baldelli group;
- members of my ORP exam and Ph.D. defense committees;
- members of my former research group at the Institute for Tropical Technology, VAST, Vietnam, for their financial support and encouragement;
- my family and my friends for their love and support, they are the reason I am here today;
- my wife for her love and patience.

Adsorption of Surfactants and Mixed Surfactants at the Hydrophilic Silica/Water Interface Studied Using Total Internal Reflection Raman Spectroscopy and Target Factor Analysis

---

An Abstract of a Dissertation

Presented to

the Faculty of the Department of Chemistry

University of Houston

In Partial Fulfillment

of the Requirements for the Degree

Doctor of Philosophy

By

Dien Ngo

December 2016

Abstract

Adsorption of dimethyldodecylamine oxide (DDAO), Triton X-100 (TX-100), and their mixtures at the hydrophilic silica/water interface has been studied using total internal reflection (TIR) Raman spectroscopy and target factor analysis (TFA). The use of a vibrational spectroscopic technique gives rise to information about the adsorbed layer at the molecular level. The combination of a linear technique like TIR Raman and TFA helps determine the contribution of each surfactant in the mixed adsorbed layer on the silica surface.

The first part of the study is on the adsorption of pure surfactants, DDAO and TX-100, on the silica surface with and without 0.20 M NaCl in the bulk solutions. The alkyl chains of DDAO were found to be in a liquid-like medium and were not significantly affected by the presence of sodium chloride. The conformation and orientation of the alkyl chains of DDAO were generally independent of surfactant concentrations. The DDAO adsorption isotherms, however, were clearly affected by the addition of NaCl to the surfactant solution. Before the intersection point between the isotherm curves obtained with and without 0.20 M NaCl, the adsorbed amount of DDAO on the silica surface is higher without the presence of NaCl. However, after the intersection point, the adsorption isotherm of DDAO with NaCl is higher than that without NaCl. The adsorption isotherms of TX-100 show an S-shape and a dramatic increase of the adsorbed amount due to the co-existence of both monomers and aggregates at the interface.

Mixtures of DDAO and TX-100 were investigated in the second part of the study. The adsorption of TX-100 from solutions without 0.20 M NaCl on the silica surface was greatly enhanced in the mixtures when it was at very low concentrations. The adsorption of DDAO in this case, however, was only clearly enhanced at its low bulk concentration. The adsorption measurements of mixed surfactants with 0.20 M NaCl in the bulk solution demonstrated the role of pre-

adsorbed DDAO in enhancing the adsorption of TX-100 at the interface. TFA is very helpful in determining the contribution of each surfactant to the mixed spectra and in understanding the adsorption mechanism of mixed surfactants.

Contents

1 Introduction **1**

1.1 Motivation and goals of the study 1

1.2 Applications of TIR Raman spectroscopy 5

2 Theoretical Background **7**

2.1 Surfactants 7

2.1.1 Classification of surfactants 7

2.1.2 Micelles 8

2.1.3 Mixed surfactants 10

2.2 Silica surface 13

2.2.1 Chemistry of silica 13

2.2.2 Adsorption on silica surfaces 14

2.3 Reflection and refraction at interfaces 19

2.4 Total internal reflection and evanescent field 21

2.5 Internal reflection in a two-phase system 24

2.6 Raman spectroscopy 25

2.6.1 Classical theory of Raman scattering 25

2.6.2 Quantum mechanical theory of Raman scattering 28

2.7 Target factor analysis 30

2.8 Adsorption isotherm 32

3 Experiments **34**

3.1 TIR Raman setup 34

3.2 Raman cell 38

3.3 Calibration of the TIR Raman setup 39

3.4 Sample preparation of TIR Raman experiments 42

3.5 Raman measurement 42

3.6 Data processing of Raman spectra 43

3.6.1 Data preprocessing 43

3.6.2 Target factor analysis 45

3.7 Raman experiments with ITO coating 49

3.8 Sum frequency generation spectroscopy measurements 52

3.9 Conductivity measurements 53

4 Adsorption of Pure Surfactants **56**

4.1 Adsorption of DDAO without added salt 56

4.1.1 DDAO spectra 56

4.1.2 Adsorption isotherm 65

4.1.3 Adsorption mechanism 66

4.2 Adsorption of DDAO with added NaCl 68

4.2.1 DDAO Spectra 68

4.2.2 Adsorption isotherm 74

4.3 Adsorption of TX-100 77

4.3.1 TX-100 spectra 77

4.3.2 Adsorption isotherm 79

5 Adsorption of mixtures of DDAO and TX-100 **82**

5.1 Adsorption of mixtures without added salt 82

5.1.1 Adsorption of mixtures at low concentration of DDAO . . 82

5.1.2 Adsorption of mixtures at higher concentration of DDAO . 92

5.1.3 Adsorption mechanism 95
5.2 Adsorption of mixtures with added NaCl 97
5.2.1 Adsorption of mixtures at low concentration of DDAO . . 97
5.2.2 Adsorption isotherm 99
5.2.3 Adsorption kinetics 102
5.2.4 Adsorption of mixtures at high concentrations of DDAO . 105

6 Conclusions **107**

Appendix A 1-Hexadecyl-3-Methylimidazolium Chloride **109**

Appendix B Adsorption on the ITO Surface **113**

List of Figures

1.1 The chemical structures of DDAO (above) and TX-100 (below) (n=9-10) used in the study. 4

1.2 Example of using target factor analysis (TFA) to decompose a mixed spectrum of DDAO and TX-100 into single component spectra: (left) mixed spectrum; (right) single component spectra. The mixed surfactant solution contained 0.30 mM DDAO and 1.08 mM TX-100. 5

2.1 Schematic illustration of the silica surface in contact with water. The in-plane and out-of-plane silanols are shown in black and blue, respectively.[52] 14

2.2 The two-step adsorption model: (A) the general shape of the adsorption isotherm and (B) the proposed model for the adsorption. Adapted from reference 62. 16

2.3 The four-region model: (A) the general shape of the adsorption isotherm and (B) the proposed model for the adsorption. Adapted from reference 62. 18

2.4 Reflection and refraction of light at an interface: $E_i^{(p)}$ is the component of the electric field E parallel to the incident plane, $E_r^{(p)}$ is the reflected part of $E_i^{(p)}$, and k is the wavevector. n_i and n_t are the refractive indices of the incidence and transmission media.[81] . 20

2.5 The total internal reflection of light at an interface: $E_i^{(p)}$ is the the component of the electric field E parallel to the incident plane, $E_r^{(p)}$ is the reflected part of $E_i^{(p)}$, and k is the wavevector. n_i and n_t are the refractive indices of the incidence and transmission media.[81] 22

2.6 Variation of the penetration depth of the evanescent wave into the transmitted medium with respect to the incident angle of the electric field. 23

2.7 Variation of the mean-squared electric fields at the interface with respect to the incident angle of the electric field.[82] 25

2.8 Energy level diagram for Stokes Raman, Rayleigh, and Anti-Stokes Raman scattering. 28

3.1 TIR Raman setup. M_{1-5} are mirrors. 35

3.2 Part of the TIR Raman setup. 36

3.3 Spectrograph and CCD camera of the TIR Raman setup. 37

3.4 Illustration of the Raman cell and sample pumping system. 39

3.5 Raman spectrum of mixture of 50/50 toluene - acetonitrile. 40

3.6 Raman spectrum of Cyclohexane. 40

3.7 Raman spectrum of mixture of 50/50 toluene-acetonitrile.[88] . . . 41

3.8 Raman spectrum of cyclohexane.[88] 41

3.9 Acquisition setup 44

3.10 TIR Raman spectra: (A) water and mixed sample spectra; (B) background subtracted and baseline corrected spectra of a mixed sample of TX-100 and DDAO. The bulk solution contained 0.30 mM DDAO and 0.20 mM TX-100. The ALS technique was used for the baseline correction.[89] 45

3.11 Asymmetric least-squares baseline correction of the background corrected Raman spectrum of DDAO obtained from the S_y-polarized measurement. 46
3.12 The columns of the abstract row matrix plotted versus wavenumber. These abstract columns were obtained from the principal factor analysis of Raman spectra of DDAO and TX-100 mixtures. The DDAO concentration was 0.30 mM and the TX-100 concentration was varied. 47
3.13 Component weights of components 1 and 2 plotted versus log([TX-100]/mM). These abstract rows were obtained from the principal factor analysis of Raman spectra of DDAO and TX-100 mixtures. The DDAO concentration was 0.30 mM and the TX-100 concentration was varied. 47
3.14 Predicted (refined) and target S_y-polarized Raman spectra of DDAO used in the target factor analysis of pure DDAO spectra. 49
3.15 Schematic illustration of the TIR Raman experiment with ITO coating: (1) fused silica IR grade hemispherical prism, (2) index matching fluid, (3) glass substrate, (4) ITO coating, (5) aqueous solution. 50
3.16 Schematic illustration of the TIR Raman experiment with the ITO coating: (1) fused silica IR grade hemispherical prism, (2) ITO coating, (3) aqueous solution. 51
3.17 The Raman cell used in the measurements with the ITO coating: (CE) counter electrode, (RE) reference electrode. The working electrode was the ITO coating on the flat side of prism. 52
3.18 Geometry for SFG experiments. 53

3.19 Schematic illustration of the electrochemical setup used in conductivity measurements of surfactant solutions. The two electrodes were flat platinum foil. 54
3.20 Photograph of the conductivity measurement cell. 54
3.21 New conductivity measurement cell. 55

4.1 Background subtracted and baseline corrected TIR Raman spectra of DDAO at the silica/water interface with various DDAO bulk concentrations. Spectra were collected under S_x and S_y polarization combinations. 58
4.2 Background subtracted and baseline corrected TIR Raman spectra of DDAO at the silica/water interface with various DDAO bulk concentrations. Spectra were collected under P_x and P_y polarization combinations. 59
4.3 S_x-polarized Raman spectrum of DDAO at 1.81 mM bulk concentration fitted to Gaussian functions. 60
4.4 Relative peak heights of asymmetric (d^-) and symmetric (d^+) methylene stretches obtained from S_x-polarized Raman spectra and plotted as a function of DDAO concentration. 64
4.5 Relative intensities of the d^- band in the S_x- and P_x-polarized spectra. 64
4.6 Adsorption isotherm of DDAO at the silica/water interface obtained from integrated areas of the C-H stretching region (2800-3000 cm^{-1}) of DDAO spectra collected under S_y polarization combination. 66

4.7 Background subtracted and baseline corrected TIR Raman spectra of DDAO at the silica/water interface with various DDAO bulk concentrations. Spectra were collected under S_x and S_y polarization combinations. The solution concentration of NaCl was 0.20 M. 69

4.8 Background subtracted and baseline corrected TIR Raman spectra of DDAO at the silica/water interface with various DDAO bulk concentrations. Spectra were collected under P_x and P_y polarization combinations. The solution concentration of NaCl was 0.20 M. 70

4.9 S_x-polarized Raman spectra of DDAO at the silica/water interface fitted to Gaussion functions. DDAO solution concentration was 1.80 mM. 71

4.10 Relative peak heights of asymmetric (d^-) and symmetric (d^+) methylene stretches obtained from S_x-polarized Raman spectra and plotted as a function of DDAO concentration. 74

4.11 Relative intensities of the d^- band in the S_x- and P_x-polarized spectra as a function of DDAO concentration. 75

4.12 Adsorption isotherms of DDAO at the silica/water interface with and without 0.20 M NaCl in the aqueous solutions. 76

4.13 Background subtracted and baseline corrected TIR Raman spectra of TX-100 at the silica/water interface with various TX-100 bulk concentrations. Spectra were obtained from S-polarized measurements. 78

4.14 Background subtracted and baseline corrected TIR Raman spectra of TX-100 at the silica/water interface with various TX-100 bulk concentrations. Spectra were obtained from S-polarized measurements. NaCl concentration was 0.20 M. 78

4.15 Component weights of TX-100 with and without 0.20 M NaCl in the aqueous solutions. These values are from target factor analysis of sets of TX-100 spectra. 80
4.16 Adsorption isotherms of TX-100 at the silica/water interface with and without 0.20 M NaCl in the aqueous solutions. 80
4.17 Adsorption isotherms of TX-100 at the silica/water interface: (A) with 0.20 M NaCl and (B) without 0.20 M NaCl in the bulk solution. The solid lines represent the isotherms fitted to the Frumkin model. The isotherm here is expressed in term of surface excess. The open circles were not used in the fittings. 81

5.1 Background subtracted and baseline corrected TIR Raman spectra of DDAO and TX-100 mixtures at DDAO bulk concentration of 0.30 mM and varied concentrations of TX-100. 83
5.2 S-polarized Raman spectrum of DDAO at the silica/water interface with a bulk concentration of 0.30 mM. 83
5.3 Target and refined spectra of DDAO and TX-100. The target spectra were obtained from S-polarized Raman experiments without a polarizer in the setup. 85
5.4 Component weights of TX-100 and DDAO in the mixtures as a function of log([TX-100]/mM). The bulk concentration of DDAO was 0.30 mM. 85
5.5 Integrated CH areas of TX-100, DDAO and mixed spectra plotted as a function of log([TX-100]/mM). The integrated CH region is from 2800 to 3000 cm^{-1}. The dashed line shows integrated values of pure DDAO at the silica/water interface with a bulk concentration of 0.30 mM. 86

5.6 Adsorption isotherms of TX-100 in single and mixed systems as a function of log([TX-100]/mM). The isotherm here is expressed in terms of surface excess. TIR Raman experiments of the mixtures were performed with constant concentration of DDAO (0.30 mM) and varied concentration of TX-100. 88

5.7 Adsorption kinetics of mixtures with two different bulk concentrations of TX-100: (A) 0.06 mM; (B) 0.15 mM. The bulk concentration of DDAO was fixed at 0.30 mM. 89

5.8 Adsorption kinetics of mixtures with two different bulk concentrations of TX-100: (C) 0.23 mM; (D) 0.30 mM. The bulk concentration of DDAO was fixed at 0.30 mM. 90

5.9 Adsorption kinetics of mixtures with two different bulk concentrations of TX-100: (E) 1.08 mM; (F) 18.98 mM. The bulk concentration of DDAO was fixed at 0.30 mM. 91

5.10 Background subtracted and baseline corrected TIR Raman spectra of DDAO and TX-100 mixtures at DDAO bulk concentration of 1.00 mM and varied concentrations of TX-100. 92

5.11 Component weights of DDAO and TX-100 in mixed surfactants. DDAO bulk concentration was 1.00 mM and TX-100 concentration was varied. 94

5.12 Integrated CH areas of TX-100, DDAO and mixed spectra obtained after target factor analysis and plotted as a function of log([TX-100]/mM). The integrated CH region is from 2800 to 3000 cm^{-1}. The dashed line shows integrated values of pure DDAO at the silica/water interface with a bulk concentration of 1.00 mM. . 94

5.13 Adsorption isotherms of TX-100 in single and mixed systems as a function of log([TX-100]/mM). The isotherm here is expressed in term of surface excess. TIR Raman experiments of the mixtures were performed with two different concentrations of DDAO (0.30 mM and 1.00 mM) and varied concentrations of TX-100. 95
5.14 Illustration of mixed surfactants at the silica-water interface without NaCl. TX-100 and DDAO molecules are represented by surfactants with blue and red headgroups, respectively. TX-100 concentration is increased from left to right. 96
5.15 Background subtracted and baseline corrected TIR Raman spectra of DDAO and TX-100 mixtures at DDAO bulk concentration of 0.30 mM and varied concentrations of TX-100. Sodium chloride was 0.20 M in the surfactant solution. 98
5.16 S-polarized TIR Raman spectrum of DDAO at the silica/water interface. The solution concentrations of DDAO and NaCl were 0.30 mM and 0.20 M, respectively. 98
5.17 Component weights of TX-100 and DDAO in mixed surfactants plotted as functions of log([TX-100]/mM). The solution concentrations of DDAO and NaCl were 0.30 mM and 0.20 M, respectively. 99
5.18 Integrated CH areas of TX-100, DDAO and mixed spectra obtained after target factor analysis and plotted as a function of log([TX-100]/mM). The integrated CH region is from 2800 to 3000 cm^{-1}. The dashed line shows integrated values of pure DDAO at the silica/water interface with a bulk concentration of 0.30 mM. . 100

5.19 Adsorption isotherms of TX-100 in single and mixed systems as a function of log([TX-100]/mM). The isotherm here is expressed in terms of surface excess. TIR Raman experiments of the mixtures were performed with 0.30 mM DDAO and varied concentration of TX-100. The NaCl concentration was 0.20 M. 101

5.20 Adsorption kinetics of mixtures with two different bulk concentrations of TX-100: (A) 0.10 mM; (B) 0.40 mM. The bulk concentrations of DDAO and NaCl were fixed at 0.30 mM and 0.20 M, respectively. 103

5.21 Adsorption kinetics of mixtures with two different bulk concentrations of TX-100: (C) 2.44 mM; (D) 18.96 mM. The bulk concentrations of DDAO and NaCl were fixed at 0.30 mM and 0.20 M, respectively. 104

5.22 TIR Raman spectra of mixtures of TX-100 with DDAO. TX-100 bulk concentration was fixed at 1.05 mM. DDAO bulk concentrations were 1.06 mM and 2.00 mM in the first and second mixtures, respectively. 105

5.23 Extracted spectra of DDAO and TX-100 from mixtures of TX-100 with high DDAO concentrations. TX-100 bulk concentration was fixed at 1.05 mM. DDAO bulk concentrations were 1.06 mM and 2.00 mM in the first and second mixtures, respectively. NaCl concentration was 0.20 M. 106

A.1 1-hexadecyl-3-methylimidazolium chloride 109

A.2 Background subtracted and baseline corrected TIR Raman spectra of 1-hexadecyl-3-methylimidazolium chloride at the silica/water interface with various solution concentrations. Spectra were collected under the S_x and S_y polarization combinations. 110

A.3 Background subtracted and baseline corrected TIR Raman spectra of 1-hexadecyl-3-methylimidazolium chloride at the silica/water interface with various solution concentrations. Spectra were collected under the P_x and P_y polarization combinations. 111

A.4 Integrated CH stretching area of S_y-polarized Raman spectra of 1-hexadecyl-3-methylimidazolium chloride at the hydrophilic silica/water interface as a function of concentration. 112

B.1 Cyclic Voltammogram of the ITO coating at a scan rate of 50 mV/s. The measurements were done in 0.1 M KCl solution. . . . 113

B.2 The Raman spectra of cetyl trimethylammonium bromide (CTAB) at the ITO/water interface. 114

List of Tables

3.1 Acquisition setup 43

4.1 Peak assignments of DDAO Raman spectra[62;100;101] 60

4.2 Vibrational modes from fitting S_x-polarized Raman spectra of DDAO at the silica/water interface 62

4.3 Full width at half maximum (FWHM) of vibrational modes from fitting S_x-polarized Raman spectra of DDAO at the silica/water interface 63

4.4 Peak assignments of DDAO Raman spectra[62;100;101] 71

4.5 Vibrational modes from fitting S_x-polarized Raman spectra of DDAO at the silica/water interface 72

4.6 Full width at half maximum (FWHM) of vibrational modes from fitting S_x-polarized Raman spectra of DDAO at the silica/water interface 73

4.7 Parameters obtained from fitting adsorption isotherms of TX-100 to the Frumkin model. 81

5.1 Results obtained from target testing of DDAO and TX-100 mixtures. DDAO concentration was of 0.30 mM and TX-100 concentration was varied. 84

5.2 Results obtained from target testing of DDAO and TX-100 mixtures. DDAO concentration was of 1.00 mM and TX-100 concentration was varied. 93
5.3 Results obtained from target testing of DDAO and TX-100 mixtures. DDAO concentration was 0.30 mM and TX-100 concentration was varied. The NaCl concentration in the mixtures was 0.20 M. 99

Chapter 1

Introduction

1.1 Motivation and goals of the study

Dimethyldodecylamine oxide (DDAO) belongs to the group of amine oxides that can exist in both non-ionic and cationic forms in aqueous solutions. The two forms are in equilibrium according to the following equation:[1]

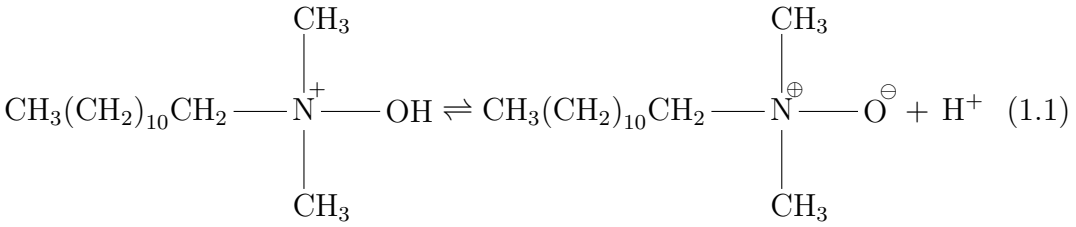

$$CH_3(CH_2)_{10}CH_2-N^{+}(CH_3)_2-OH \rightleftharpoons CH_3(CH_2)_{10}CH_2-N^{\oplus}(CH_3)_2-O^{\ominus} + H^+ \quad (1.1)$$

The equilibrium constant of DDAO is defined as below:

$$K_a = \frac{[B][H^+]}{[A]} = 10^{-4.7} \quad (1.2)$$

where A and B are the acidic and basic forms of DDAO, respectively.[2] The ratio of the two forms of DDAO thus depends on concentration, pH, and ionic strength of the solution.

The short alkyl chain amine oxide, trimethylamine oxide (TMAO), is well known as a protein stabilizer while the long alkyl chain amine oxides have been used in commercial products with many different functions.[3] They have been

used as foam boosters in light-duty detergents and shampoos,[4] and as hair conditioners.[5] In addition, amine oxides are component of bar soaps,[6] fabric softeners,[7] and DNA-condensing agents.[8] In those applications amine oxides play an important role that determines the product quality.

Amine oxides can form hydrogen bonds with water. The N-O bond is highly polar and acts as a hydrogen-bond acceptor. According to theoretical calculations an amine oxide molecule can form up to three hydrogen bonds with water molecules.[9;10] An FT-IR study by Maeda et al. confirmed the existence of a hydrogen bond between the two headgroups of the non-ionic-cationic pair.[11] It is the ability of amine oxides to form hydrogen bonds in their aqueous solutions that determines their many important applications.[3;4;6]

Adsorption studies of amine oxides at the solid/liquid interface have been done using several techniques. Claesson et al. used a surface force apparatus (SFA) for a study of the interaction between DDAO surfactant layers adsorbed on a mica surface.[12] It was from this study that a thermodynamically unstable monolayer was first formed on the mica surface and a stable bi-layer was built up after leaving the mica surface in contact with the DDAO solution overnight. The authors concluded that the DDAO adsorption on the mica surface was caused by electrostatic interactions between the cationic form of DDAO and the negatively charged mica surface. This conclusion was supported by a similar experiment with dimethyldodecylphosphine oxide (DDPO). DDPO molecules are far less protonated than DDAO and were found not to adsorb on the mica surface. DDAO molecules close to the mica surface were also proposed to have a higher ionization than those in the bulk solution.[13] In another study using microcalorimetric experiments, adsorption of three different alkyldimethylamine oxides CnDAO (n = 8, 10, and 12) were considered at natural pH.[1] This study revealed that at dilute concentrations the adsorption of surfactants is exothermic and enthalpically driven. The protonated amine oxide molecules and negatively charged surface

$\equiv SiO^-$ groups (siloxides) were found to reserve some of their counterions and hydrated water during their interactions.

Synergistic effects of alkyldimethylamine oxide are also an interesting property. An adsorption investigation of a mixture of DDAO with dodecyl maltoside ($C_{12}G_2$) at the silica/water interface revealed that DDAO enhanced the adsorption of its co-surfactant significantly.[2] The adsorbed amount of ($C_{12}G_2$) on the hydrophilic silica surface is negligible without DDAO. This adsorption enhancement was believed to occur via hydrophobic interactions between the hydrophobic tails of readily adsorbed DDAO molecules and ($C_{12}G_2$) molecules. Alkyldimethylamine oxides can be used with cationic, anionic, non-ionic, and zwitterionic surfactants. Their mixtures with anions, for example, are more surface-active than single components of the mixtures.[14]

Although being a class of surface active agents with many important practical applications, most studies of alkyldimethylamine oxides are concerned with their bulk solution properties such as micelle size,[15–17] hydrogen bonding,[11;18] and ionization.[19–21] A limited number of studies, mentioned above, were performed to obtain information on the adsorption behavior of surfactant molecules at the solid/liquid interface. The techniques used in those studies were not aimed to give information at the molecular level. The understanding of adsorption process is incomplete without knowledge of adsorbed layer structure, vibrational characteristics, and conformational changes. Therefore, a different technique that can acquire this information must be used.

This study has used total internal reflection (TIR) Raman spectroscopy and target factor analysis (TFA) to investigate the adsorption of DDAO, TX-100 (Figure 1.1), and their mixtures at the silica/water interface. TIR Raman spectroscopy is a linear vibrational technique, in which the intensity is proportional to the concentration of molecules. It can give us molecular level information such as molecular vibrations, conformation and orientation of hydrocarbon chains of

surfactant molecules at the interface. In practical applications, a small amount of DDAO is often added to detergent mixtures to modify the performance of the detergents. The combination of TIR Raman and TFA will help to understand the role of DDAO in the adsorption of its mixtures with TX-100 on the silica surface.

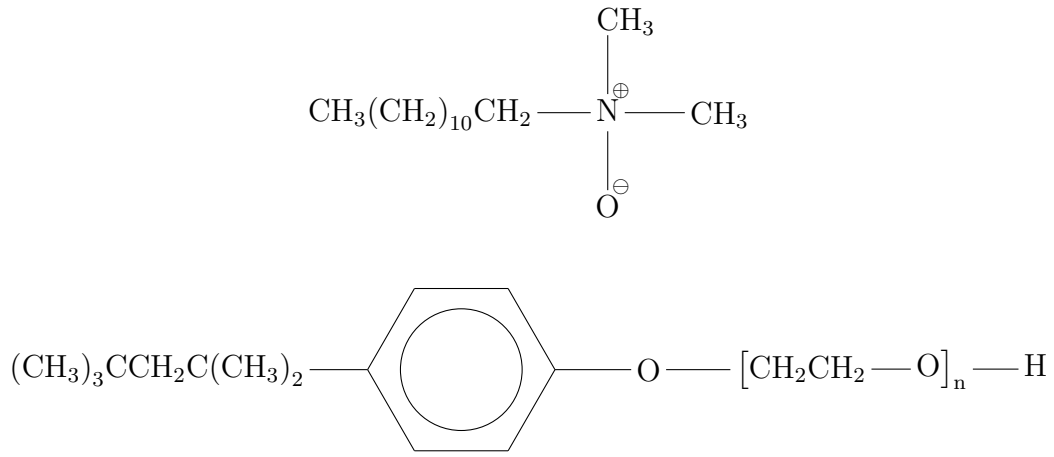

Figure 1.1. The chemical structures of DDAO (above) and TX-100 (below) (n=9-10) used in the study.

The total Raman signal of the probed volume is a linear sum of the Raman scattering from all the molecules in that volume. When the probed volume contains different kinds of molecules and these molecules have different spectral features, their contributions to the overall Raman spectrum can be separated by using TFA.[22] Being a chemometric method, TFA is very useful in studying chemical systems involving more than one component. It is similar to principal component analysis (PCA), however, the outcome from TFA is physically meaningful due to a target transformation step using the real, pure surfactant spectra as targets. Studies of mixed chemical systems using vibrational spectroscopy often use deuterated samples to reduce or remove the strong overlap of component spectra.[23–25] This approach, however, is expensive and complicated in many experiments. Target factor analysis, as well as other chemometric

techniques, eliminates the deuteration problem and is very powerful when the application of deuteration is essentially impossible.[26;27] TFA is effective in noise filtering and signal retrieving when dealing with a spectrum of low signal to noise ratio. An example of target factor analysis used to decompose a mixed spectrum of DDAO and TX-100 into single component spectra is shown in Figure 1.2.

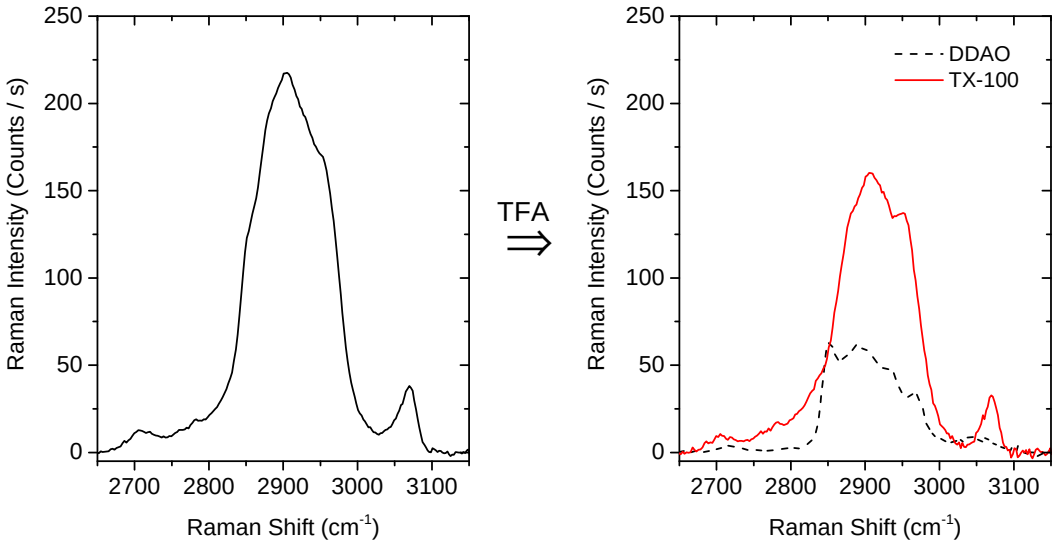

Figure 1.2. Example of using target factor analysis (TFA) to decompose a mixed spectrum of DDAO and TX-100 into single component spectra: (left) mixed spectrum; (right) single component spectra. The mixed surfactant solution contained 0.30 mM DDAO and 1.08 mM TX-100.

1.2 Applications of TIR Raman spectroscopy

In the current study, Raman measurements have been performed using the total internal reflection configuration. The evanescent wave generated at the silica/water interface excites molecules in the interfacial region and causes Raman scattering. TIR Raman spectroscopy has been used to study various kinds of chemical systems,[28–30] and its applications have been reviewed in detail by Woods et al.[31] The first TIR Raman experiment was performed at the interface between a hemispherical flint glass and liquid carbon disulfide CS_2.[32]

Although the Raman signal was weak, the possibility of performing Raman experiments using the TIR geometry was demonstrated. The authors also suggested ways to improve the Raman signal and future uses of TIR Raman. In the second study, TIR Raman spectroscopy was coupled with electrochemical measurements to monitor adsorbed dye layers at electrode-solution interface.[33] A thin layer of transparent SnO_2 was deposited on a quartz prism and was used as the working electrode. The potential of the SnO_2 surface was controlled and Raman signal was successfully recorded. Iwamoto and co-workers studied polymer films on a sapphire surface and demonstrated that TIR Raman spectroscopy has advantages over attenuated total reflection infrared (ATR-IR) spectroscopy in the analysis of surface layers of much thinner thicknesses.[34] The method was later demonstrated with different internal reflection elements (IRE) in studies of polymer films.[35] Adsorption of dye molecules at the liquid/liquid interfaces have also been detected by this total internal reflection spectroscopic method.[36;37] Polarized TIR Raman measurements have been shown to be useful in studies of thin films of organic molecules. They can detect changes in conformation and orientation of molecules in the film as well as can reveal phase transitions with respect to temperature.[38;39] TIR Raman spectroscopy has recently been utilized in measurements of adsorption kinetics of surfactants and mixed surfactants at the solid/liquid interface.[26;40] The spectra could be recorded every second with good signal-to-noise ratio. The Smith group has developed a scanning angle total internal reflection Raman spectrometer with an incident angle range of 25.5^{o}-75.5^{o}, and have utilized the setup in several studies.[41;42] Tribology has also applied TIR Raman spectroscopy to studies of friction-induced material transfer and oils in a lubricated contact.[43;44]

Chapter 2

Theoretical Background

2.1 Surfactants

2.1.1 Classification of surfactants

Surfactants are amphiphilic molecules that have both lyophobic and lyophilic functional groups in their structures.[14] The lyophilic group (headgroup) has strong interactions with the solvent, while the interaction between the lyophobic group (tail) and the solvent is insignificant. In an aqueous solution of surfactant molecules, the lyophobic and lyophilic groups are termed hydrophobic and hydrophilic groups, respectively. Surfactant molecules in water may distort the solvent structure which will lead to an increase of the free energy of the system. The solvent, in order to minimize the distortion, will expel surfactant molecules out of its bulk solution. Due to the different interactions of the hydrophobic and hydrophilic groups with water, at the air/water interface the hydrophobic group will orient away from water while the hydrophilic will orient towards it.[14] Depending on the chemical structure of the headgroups, surfactants can be classified as cationic, anionic, non-ionic or zwitterionic.

Cationic surfactants. The headgroups of these surfactants have positive charge, and include molecules such as cetyl trimethylammonium bromide (CTAB), primary amine salts ($RNH_3^+X^-$), and cetyl trimethylammonium p-

toluene-sulfonate. Amine oxides are considered cationic or non-ionic surfactants depending on the solution pH. Cationic surfactants are found in various applications, such as corrosion inhibitors for metal surfaces and emulsifying agents in acidic solutions.

Anionic surfactants. The lyophilic group of an anionic surfactant bears a negative charge. Sodium dodecyl sulfate (SDS), sodium stearate, and alkylbenzene sulfonate ($RC_6H_4SO_3^-Na^+$) are typical examples of this class of surface-active agents. Anionic surfactants have been used as soap, anti-static agents, hair care and skin care detergents, among other applications.

Non-ionic surfactants. The lyophilic groups of these molecules have no net charge, and include examples such as alkylphenol ethoxylates ($RC_6H_4-(OC_2H_4)_xOH$), alcohol ethoxylates ($R(OC_2H_4)_xOH$), and long-chain carboxylic acid esters. Alkylphenol ethoxylates have been used as water/oil emulsifying agents, co-solvents, and cosmetic emulsions. Other non-ionic surfactants are detergents in laundry products, cosmetic emulsifiers, and so on.

Zwitterionic. These are surfactants consisting of both negative and positive charges in their molecules. Long-chain amino acids ($RN^+H_2CH_2COO^-$), sulfobetaines ($RN^+(CH_3)_2CH_2CH_2SO_3^-$), and imidazoline carboxylates are examples of this surfactant class. Zwitterionic surfactants exist in corrosion inhibitors, cosmetics, fabric softeners, among other products.

2.1.2 Micelles

The general chemical potential of an aggregate of size N in solution is defined in Equation 2.1,[45] where X_N is generally the activity (or concentration in dilute solutions) of molecules in aggregates. It is expressed here in terms of mole fraction. The mean chemical potential of a molecule in the aggregate is μ_N and μ_N^o is the standard chemical potential (the mean interaction free energy per

molecule). When N is equal to 1, Equation 2.1 describes the chemical potential of a monomer in solution. Taking the difference between μ_1 and μ_N we obtain Equation 2.2 for the activity X_N.

$$\mu = \mu_N = \mu_N^o + \frac{kT}{N} log(\frac{X_N}{N}) \tag{2.1}$$

$$X_N = N\{X_1 exp[(\mu_1^o - \mu_N^o)/kT]\}^N \tag{2.2}$$

Molecular aggregates can have different kinds of structures such as cylinders, discs, and spheres and their mean interaction free energy per molecule is shown in Equation 2.3. μ_∞^o indicates the bulk energy per molecule while α is a positive constant that is decided by the magnitude of the intermolecular interactions. The shape of the aggregates determines the value of p. Equation 2.3 tells us that the mean value of μ_N^o decreases as N increases.

$$\mu_N^o = \mu_\infty^o + \frac{\alpha kT}{N^p} \tag{2.3}$$

From Equations 2.2 and 2.3 we have the following equation,

$$X_N = N\{X_1 exp[(\mu_1^o - \mu_N^o)/kT]\}^N = N\{X_1 exp[\alpha(1 - 1/N^p)]\}^N \approx N[X_1 e^\alpha]^N \tag{2.4}$$

At low monomer concentration when $X_1 e^\alpha \ll 1$, X_N decreases as N increases. This means that at sufficiently low monomer concentrations, the bulk solution will be dominated by the isolated monomers. X_N is always less than 1 such that X_1 cannot exceed $e^{-\alpha}$. The concentration at which X_1 approaches $exp[(\mu_1^o - \mu_N^o)/kT]$ or $e^{-\alpha}$ is called the critical micelle concentration (cmc) and is shown in Equation 2.5. A solution with a concentration higher than the cmc will form aggregates and the mole fraction of the monomer will be equal to or

below the $e^{-\alpha}$ value.

$$\text{cmc} = exp[(\mu_1^{\text{o}} - \mu_N^{\text{o}})/kT] = e^{-\alpha} \tag{2.5}$$

2.1.3 Mixed surfactants

This section describes the pseudo-phase separation model that includes interactions between different components of the micelle in the formulation. The model has been used quite successfully to describe various mixtures of nonionic and ionic surfactants. The derivations in this section are based on the works of Holland and Rubingh,[46;47] considering only solutions that contain mixed micelles.

In a solution of N components the chemical potential of the ith component (μ_i) out of the mixed micelles is given by Equation 2.6. The standard chemical potential and free monomeric concentration of the ith component are μ_i^{o} and C_i^m, respectively. The activity coefficient is considered one in writing the following equation.

$$\mu_i = \mu_i^{\text{o}} + RTlnC_i^m \tag{2.6}$$

When the ith component is in the mixed micelles, the chemical potential (μ_i^*) is given as below,

$$\mu_i^* = \mu_i^{*\text{o}} + RTlnf_i x_i \tag{2.7}$$

where f_i and x_i are the activity coefficient and mole fraction of the ith component in the mixed micelles, respectively, and $\mu_i^{*\text{o}}$ is the standard chemical potential of the ith component in the mixed micelles. For micelles of pure ith component, $\mu_i^{*\text{o}}$ can be related to the critical micelle concentration (C_i) of pure surfactant i and to μ_i^{o} as given below

$$\mu_i^{*\text{o}} = \mu_i^{\text{o}} + RTlnC_i \tag{2.8}$$

When the chemical system is at equilibrium, the chemical potential of the ith component inside the micelles is equal to that outside of the micelles. From Equations 2.6-2.8, at equilibrium we have

$$C_i^m = x_i f_i C_i \tag{2.9}$$

or

$$x_i = \frac{C_i^m}{f_i C_i} \tag{2.10}$$

where x_i is the mole fraction of component i in the mixed micelles with the constraint

$$\sum_{i=1}^{N} x_i = 1 \tag{2.11}$$

The cmc of the mixed surfactant solution can be expressed as Equation 2.12.

$$C^* = \frac{1}{\sum_{i=1}^{N} \frac{\alpha_i}{f_i C_i}} \tag{2.12}$$

This equation is obtained by a combination of Equation 2.10 and 2.11 using the relation $C_i^m = \alpha_i C^*$. α_i is the mole fraction of surfactant i in the mixed solution. The mole fraction, x_i, can also be represented by the following equation

$$x_i = \frac{\alpha_i C - C_i^m}{C - \sum_{i=1}^{N} C_i^m} \tag{2.13}$$

where the numerator and the denominator are the concentration of surfactant i and the total concentration of all components in the mixed micelles, respectively. Equations 2.9 and 2.13 are combined to give Equation 2.14. The solution of Equation 2.14 will allow us to obtain values of x_i and C_i^m.

$$\sum_{i=1}^{N} \frac{\alpha_i C}{C + f_i C_i - \sum_{i=1}^{N} C_i^m} = 1 \tag{2.14}$$

The activity coefficients of the two components i and j in the mixed micelles at the cmc can be related using Equation 2.9 and the relation $C_i^m = \alpha_i C^*$, producing the following equations,

$$f_i = \frac{\alpha_i C^*}{x_i C_i} \tag{2.15}$$

$$f_j = \frac{\alpha_j C^*}{x_j C_j} \tag{2.16}$$

which can be rearranged to give Equation 2.17.

$$x_i = \frac{\alpha_i C_j f_j x_j}{C_i \alpha_j f_i} \tag{2.17}$$

Let us define β and W as interaction parameter and pairwise interaction between two components in the mixed surfactant solution, respectively. The interaction parameters can be related to the pairwise interactions by using a simple regular solution approximation for which the relationship is given in Equation 2.18.

$$\beta_{ij} = \frac{N(W_{ii} + W_{jj} - 2Wij)}{RT} \tag{2.18}$$

When we consider binary non-ideal mixtures of surfactants, the activity coefficients can be related to the interaction parameter via the following equations,

$$f_1 = e^{\beta_{12}(1-x_1)^2} \tag{2.19}$$

$$f_2 = e^{\beta_{12}x_1^2} \tag{2.20}$$

where x_1 is the mole fraction of component 1 in the mixed solution. These two equations are modified to obtain Equation 2.21.

$$\frac{lnf_1}{lnf_2} = \frac{(1-x_1)^2}{x_1^2} \tag{2.21}$$

Using Equations 2.15 and 2.16, and keeping in mind that $x_1 + x_2 = 1$, we obtain

$$x_1^2 ln(\frac{\alpha_1 C_{12}^*}{x_1 C_1}) = (1 - x_1^2) ln(\frac{\alpha_2 C_{12}^*}{(1 - x_1) C_2}) \tag{2.22}$$

where C_{12}^* is the cmc of the mixed surfactant solution. The interaction parameter β_{12} is obtained from Equations 2.15 and 2.19 and is expressed as

$$\beta_{12} = \frac{ln(\alpha_1 C_{12}^* / x_1 C_1)}{(1 - x_1^2)} \tag{2.23}$$

For an N-component system in which β_{12} is the net interaction parameter between components i and j, and x_j is the mole fraction of the jth component, the activity coefficients can generally be expressed by the following equation

$$ln f_i = \sum_{j=1(j \neq i)}^{N} \beta_{ij} x_j^2 + \sum_{j=1(j \neq i \neq k)}^{N} \sum_{k=1}^{j-1} (\beta_{ij} + \beta_{ik} - \beta_{jk}) x_j x_k \tag{2.24}$$

2.2 Silica surface

2.2.1 Chemistry of silica

The chemistry of the silica surface has been studied by many different experimental techniques.[48–51] These studies confirm that there are two different kinds of silanol groups on a silica surface in contact with water. The out-of-plane silanol is more acidic and donates its hydrogen atom in forming hydrogen bonds with the surrounding water molecules. The in-plane silanol is more basic and is a hydrogen bond acceptor with respect to the water solvent. The two types of silanol can also form a hydrogen bond to each other. Figure 2.1 shows a schematic illustration of the surface silanol groups when they are in contact with water.[52] The acid-base equilibrium of the silanols can be expressed by Equation 2.25 below.[53]

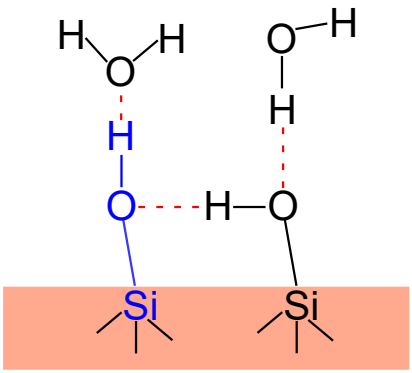

Figure 2.1. Schematic illustration of the silica surface in contact with water. The in-plane and out-of-plane silanols are shown in black and blue, respectively.[52]

$$-\mathrm{SiOH} + \mathrm{H_2O} \rightleftharpoons -\mathrm{SiO^-} + \mathrm{H_3O^+} \tag{2.25}$$

Second harmonic generation (SHG) experiments reported that the more acidic silanols have a pK_a value of 4.5 while the more basic ones have a pK_a value of 8.5.[48] The silica surface is fully protonated at a solution pH < 2 and as the pH increases, the silanols become depronated. The ionic strength of an aqueous solution was reported to affect the pK_a values, surface charge, and the strength of the effects depend on the added electrolytes.[54–56]

Theoretical calculations were also performed to determine pK_a values and to study the effects of electrolytes on the physical properties of the silica surface.[52;57–59] While the pK_a of the basic sites is the same as the one obtained from experiments, the pK_a of the more acidic silanols is higher than the experimental value.[52]

2.2.2 Adsorption on silica surfaces

Cationic surfactants. Adsorption of cationic surfactants on the silica surface has been studied using many different methods such as depletion measurements,[60;61] Raman spectroscopy,[40;62] neutron reflection,[63;64] ellipsometry,[65;66] sum frequency generation (SFG) spectroscopy,[67;68] and atomic force mi-

croscopy.[69;70] There are two models that are often used to describe the adsorption of cationic surfactants to negatively charged surfaces. The first model is a two-step model characterized by two plateau regions and the second is a four-region model. In these models, electrostatic and hydrophobic interactions play crucial roles in the adsorption process of surfactants. These two models, however, differ on points related to the relative importance of the electrostatic interaction at very low concentrations and to the step in which hemi-micelles are formed.

According to the two-step model (Figure 2.2), at very low solution concentrations, the adsorption of surfactant at the silica/water interface is driven by electrostatic interactions between the positively charged head group of the surfactant molecule and the negatively charged silica surface. In the first region (I), the interactions between adsorbed molecules are negligible and the adsorbed amount increases linearly with the solution concentration. Adsorption in the second region (II) is driven by the electrostatic interaction until the surface charge has been neutralized. The onset of region (III) occurs when the surfactant concentration is high enough for the formation of hemi-micelles. In this region the hydrophobic interactions between the alkyl chains of the surfactant species and the water molecules drive the adsorption process. Region (IV) occurs above the critical micelle concentration, and is when full aggregates (admicelles) are formed and the silica surface is saturated with surfactant molecules.[71;72]

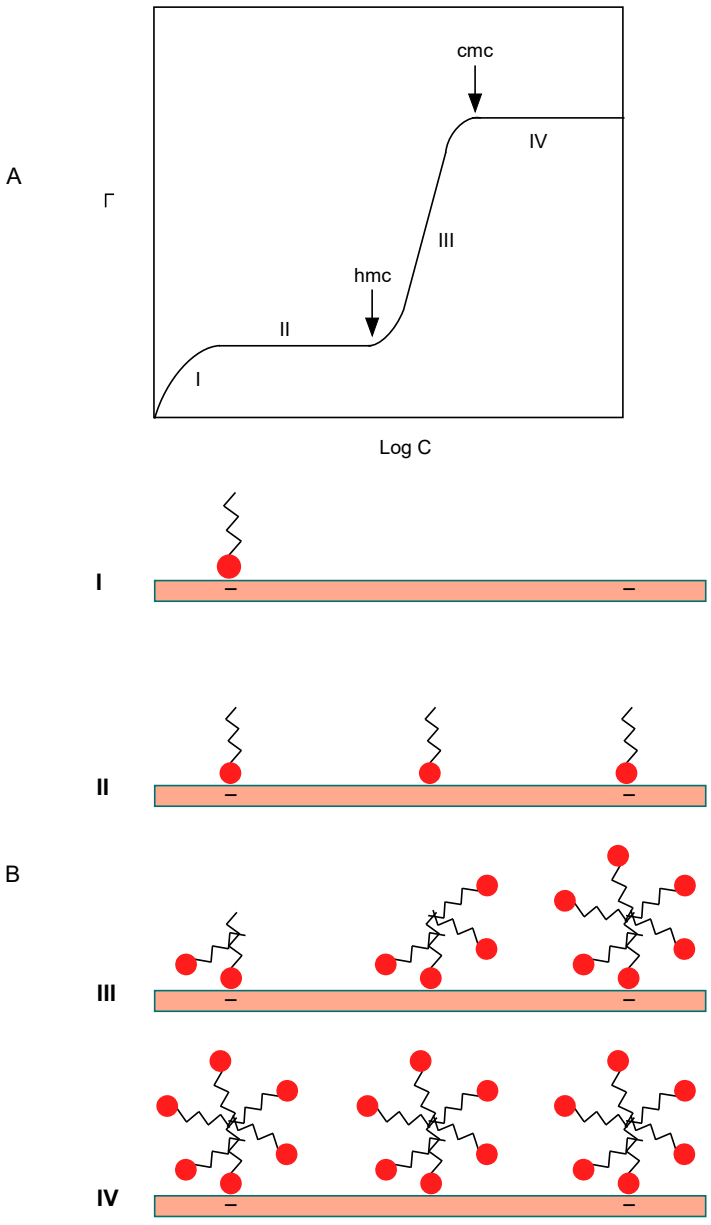

Figure 2.2. The two-step adsorption model: (A) the general shape of the adsorption isotherm and (B) the proposed model for the adsorption. Adapted from reference 62.

The four-region model (Figure 2.3) was proposed by Somasundaran and Fuerstenau to describe the adsorption isotherms plotted using a log-log scale.[71;73] The use of the four-region model with a log-log scale is useful in studying adsorption isotherms at low surface coverages. According to this model, adsorption in region (I) is driven by electrostatic interactions and the hydrocarbon chains face

towards the bulk solution while the head-groups are in contact with the surface. Surfactant aggregates are formed in region (II) due to strong lateral interactions between molecules at the interface. The neutralization of surface charges leads to the transition between regions (II) and (III). The formation of a bilayer starts in region (III) and is complete with the plateau in region (IV). After the formation of a full bilayer, the surface excess does not increase with the increase of bulk surfactant concentration.

Anionic surfactants. Adsorption of anionic surfactants on the negatively charged silica surface is negligible due to charge repulsion.[74–77] The adsorption, however, can be enhanced by the addition of salts or cationic and non-ionic surfactants to the solution. Dodecyltrimethylammanium bromide (DTAB) and sodium dodecylbenzenesulfonate (SDBS) were proposed to form ion-pairs when they adsorbed on the silica surface, thereby enhancing the adsorption of SDBS.[76] The formation of ion-pairs was proven by the fact that the surface excess of DTAB and SDBS were equal. The non-ionic surfactants enhance the adsorption of anionic surface active agents via headgroup-headgroup interactions or hydrocarbon chain-chain interactions.[77]

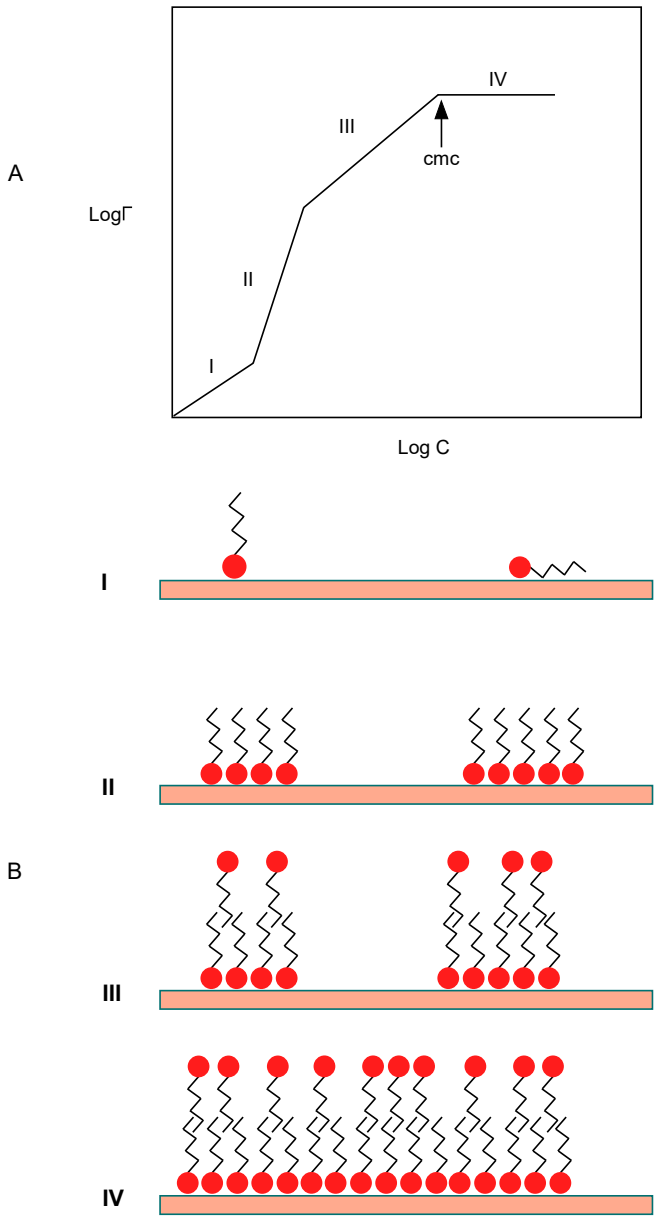

Figure 2.3. The four-region model: (A) the general shape of the adsorption isotherm and (B) the proposed model for the adsorption. Adapted from reference 62.

Non-ionic surfactants. Adsorption of non-ionic surfactants onto the hydrophilic silica surface occurs through the hydrogen bond between the surfactant headgroup and the silica surface.[40;78–80] The non-ionic surfactants that have oxyethylene groups often show an S-shaped isotherm curve.[40] For these surfactant molecules adsorption may also occur via electrostatic interactions be-

tween the negatively charged solid surface and the protonated oxygen atom in the oxyethylene group. The oxygen atom takes a proton from the water, leading to an increase in the solution pH during the adsorption process.[14]

2.3 Reflection and refraction at interfaces

The superposition of two orthogonally polarized plane waves can always be used to describe a polarized plane wave with the following form:[81]

$$E = E_0 exp(ikr - i\omega t) \tag{2.26}$$

$$E_0 = E^{(p)} + E^{(s)} \tag{2.27}$$

where k is the wave vector of the plane wave, and p or s indicate the polarization of the plane wave parallel or perpendicular to the plane of incidence, respectively. Figure 2.4 shows the reflection and refraction of a p-polarized plane wave at the interface between two media of refractive indices n_i and n_t, respectively. In the illustration in Figure 2.4 the transmission medium has a higher refractive index than the incidence medium.

At the boundary we have:

$$k_1 = (k_x, k_y, k_{z_1}) \tag{2.28}$$

$$k_2 = (k_x, k_y, k_{z_2}) \tag{2.29}$$

where k_x and k_y, the transverse components of the wavevector k, are conserved. The longitudinal wavenumbers can be calculated according to the following equations.[81]

$$k_{z_1} = \sqrt{k_1^2 - (k_x^2 + k_y^2)} \tag{2.30}$$

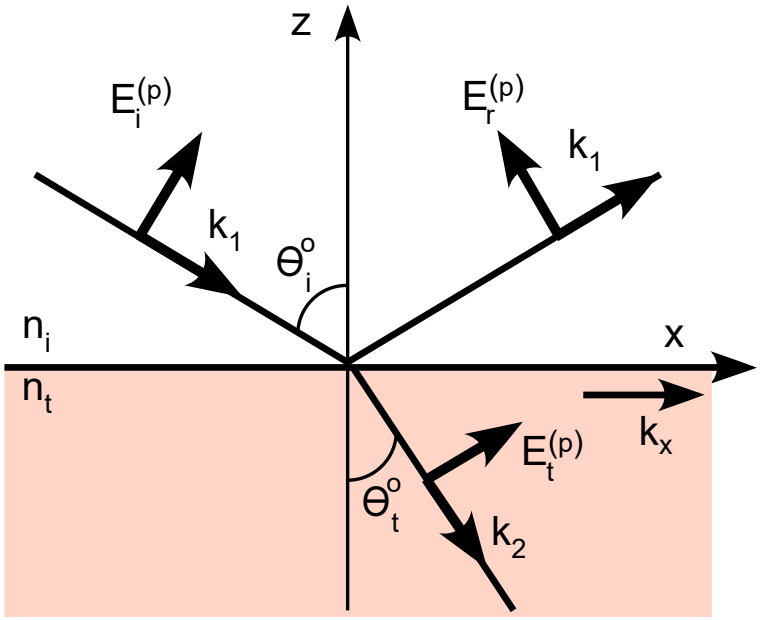

Figure 2.4. Reflection and refraction of light at an interface: $E_i^{(p)}$ is the component of the electric field E parallel to the incident plane, $E_r^{(p)}$ is the reflected part of $E_i^{(p)}$, and k is the wavevector. n_i and n_t are the refractive indices of the incidence and transmission media.[81]

$$k_{z_2} = \sqrt{k_2^2 - (k_x^2 + k_y^2)} \tag{2.31}$$

From the boundary conditions, the magnitudes of the reflected and transmitted fields can be related to the Fresnel reflection and transmission coefficients given in Equations 2.32-2.34.[81] These Fresnel coefficients are polarization dependent and can be related to the incident angle.

$$E_{ir}^{(p)} = E_i^{(p)} r^p(k_x, k_y) = E_i^{(p)} \frac{\varepsilon_2 k_{z_1} - \varepsilon_1 k_{z_2}}{\varepsilon_2 k_{z_1} + \varepsilon_1 k_{z_2}} \tag{2.32}$$

$$E_t^{(p)} = E_i^{(p)} t^p(k_x, k_y) = E_i^{(p)} \frac{2\varepsilon_2 k_{z_1}}{\varepsilon_2 k_{z_1} + \varepsilon_1 k_{z_2}} \tag{2.33}$$

$$E_{ir}^{(s)} = E_i^{(s)} r^s(k_x, k_y) = E_i^{(s)} \frac{\mu_2 k_{z_1} - \mu_1 k_{z_2}}{\mu_2 k_{z_1} + \mu_1 k_{z_2}} \tag{2.34}$$

$$E_t^{(s)} = E_i^{(s)} t^s(k_x, k_y) = E_i^{(s)} \frac{2\mu_2 k_{z_1}}{\mu_2 k_{z_1} + \mu_1 k_{z_2}} \tag{2.35}$$

where ε and μ are the dielectric and magnetic permeability constants, respectively.

2.4 Total internal reflection and evanescent field

An evanescent wave is used as the excitation source in the TIR Raman experiment. This section will present how the evanescent wave can be generated at the interface between two media of different refractive indices. The transmitted field vector shown in Figure 2.4 can be written in the complex form shown in Equation 2.36. The mathematical formulas for the electric field components are shown in the previous section. The elements of the column matrix in Equation 2.36 are the x, y, and z components of the transmitted electric field amplitude. The longitudinal wavenumbers can be expressed as functions of the incident angle θ_i and are shown in Equation 2.37.[81]

$$E_t = \begin{bmatrix} -E_i^{(p)} t^p(k_x) k_{z_2}/k_2 \\ E_i^{(s)} t^s(k_x) \\ E_i^{(p)} t^p(k_x) k_x/k_2 \end{bmatrix} e^{ik_x x + ik_{z_2} z} \tag{2.36}$$

The derivation of Equation 2.37 uses the $k_x = k_1 sin\theta_i$ and $k_1 n_i = k_2 n_t$ relationships. The relative refractive index $\tilde{n}$ is the ratio of the refractive indices of the incidence and transmission media. When $\tilde{n}$ is larger than one, an increase in the incident angle θ_i will eventually lead to a negative value of $\sqrt{1 - \tilde{n}^2 sin^2\theta_i}$. The incident angle at which the square root vanishes is called the critical incident angle and is defined in Equation 2.38.[81]

$$k_{z_1} = k_1\sqrt{1 - sin^2\theta_i},\ k_{z_2} = k_2\sqrt{1 - \tilde{n}^2 sin^2\theta_i} \tag{2.37}$$

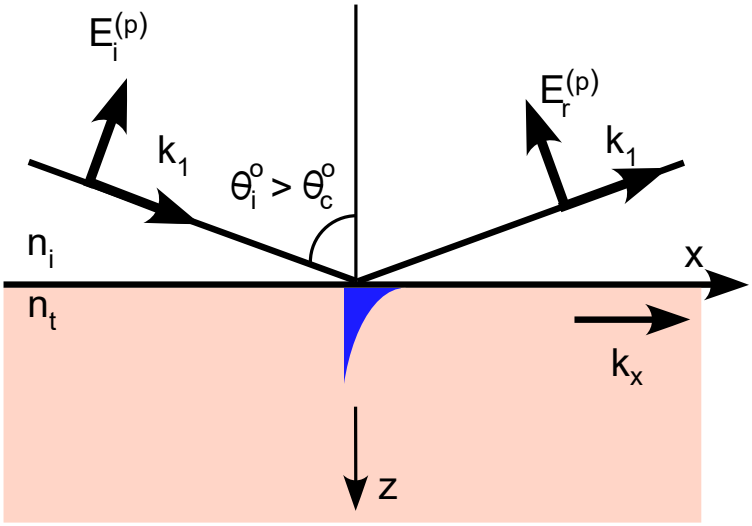

Figure 2.5. The total internal reflection of light at an interface: $E_i^{(p)}$ is the the component of the electric field E parallel to the incident plane, $E_r^{(p)}$ is the reflected part of $E_i^{(p)}$, and k is the wavevector. n_i and n_t are the refractive indices of the incidence and transmission media.[81]

$$\theta_c = arcsin(1/\tilde{n}) \tag{2.38}$$

The transmitted electric field at an incident angle higher than θ_c is given in Equation 2.39 as a function of the incident angle. The k_{z_2} is then imaginary and the transmitted wave decays into the second medium with a decay constant γ, defined in Equation 2.40. This wave is called the evanescent wave and it propagates along the surface. The penetration depth of the evanescent wave into the transmission medium depends on the wavelength of the electric field and the refractive indices of the two media (Equation 2.41).[81]

$$E_t = \begin{bmatrix} -iE_i^{(p)} t^p(\theta_i)\sqrt{\tilde{n}^2 sin^2\theta_i - 1} \\ E_i^{(s)} t^s(\theta_i) \\ E_i^{(p)} t^p(\theta_i)\tilde{n} sin\theta_i \end{bmatrix} e^{isin\theta_i k_1 x} e^{-\gamma z} \tag{2.39}$$

$$\gamma = k_2\sqrt{\tilde{n}^2 sin^2\theta_i - 1} \tag{2.40}$$

$$d_p = \frac{\lambda}{2\pi\sqrt{n_i^2 sin^2\theta_i - n_t^2}} \tag{2.41}$$

Figure 2.6 shows an example of the variation in penetration depth of an evanescent wave generated at the silica/water interface. The wavelength of the incident electric field is 532 nm and the indices of refraction of silica and water are 1.46 and 1.33, respectively. The critical incident angle is about 65.8° in this example.

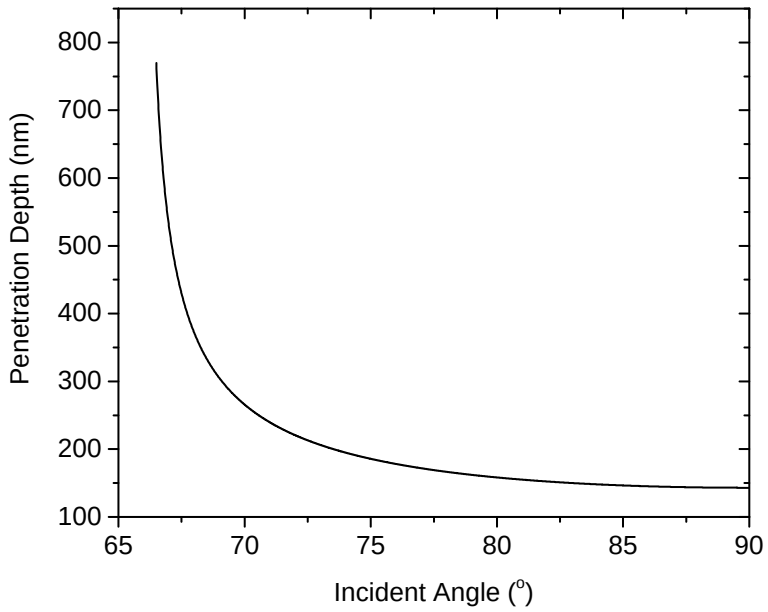

Figure 2.6. Variation of the penetration depth of the evanescent wave into the transmitted medium with respect to the incident angle of the electric field.

Calculations can prove that, for a non-absorbing medium, the z-component of the Poynting vector vanishes while the value of the x-component is non-zero when the incident angle is above θ_c. The formulas of these components are given in Equations 2.42-2.43.[81] Thus, the evanescent wave does not carry energy into the transmission medium, but rather transports the energy along the surface.

$$\langle S \rangle_z = \frac{1}{2} Re(E_x H_y^* - E_y H_x^*) \tag{2.42}$$

$$\langle S \rangle_x = \frac{1}{2} \sqrt{\frac{\varepsilon_2 \mu_2}{\varepsilon_1 \mu_1}} sin\theta_i \left(|t^s|^2 |E_i^{(s)}|^2 + |t^p|^2 |E_i^{(p)}|^2 \right) e^{-2\gamma z} \tag{2.43}$$

2.5 Internal reflection in a two-phase system

The current study involves an absorbed layer of surfactant(s) at the silica/water interface. The thickness of the layer is negligible in comparison to the wavelength used (532 nm) so that the system in the study is considered a two-phase system. The laser beam travels from the silica phase toward the water phase and is totally reflected when the incident angle is higher than the critical angle. The intensity of the Raman scattering is proportional to the square of the evanescent field. The mean-squared electric fields at the interface are given by Equations 2.44-2.46, in which $\xi_t = (n_t^2 - n_i^2 sin\theta_i^2)^{1/2}$.[82] These fields are calculated relative to the incident field and their variations with respect to the incident angle are shown in Figure 2.7. The mean-squared values are largest at the critical angle for the y and z components and vanishes for the x component, thereby enhancing the Raman signal in the TIR Raman experiments. The Raman measurements are often performed at an incident angle that is several degrees above the critical value so that the surface signal is distinguished from the bulk signal and the enhancement is still in effect. If TIR Raman measurements are performed at an incident angle too close to the critical angle, the penetration depth is too large and the contribution of the bulk solution to the total Raman signal is significant at low surfactant concentrations. Due to the size of the focused laser beam, part of the beam will not be totally reflected when an incident angle too close to the critical angle is selected. However, if the experiments are performed at an incident angle much higher than the critical angle, the magnitude of the evanescent wave will be smaller than that of the incident field and the measurement sensitivity will be reduced.

$$\left\langle E_y^2 \right\rangle = |t_s|^2 exp(4\pi \frac{z}{\lambda} Im\xi_t) \tag{2.44}$$

$$\left\langle E_x^2 \right\rangle = |\frac{\xi_t}{n_t} t_p|^2 exp(4\pi \frac{z}{\lambda} Im\xi_t) \tag{2.45}$$

$$\left\langle E_z^2 \right\rangle = |\frac{n_i sin\theta_i}{n_t} t_p|^2 exp(4\pi \frac{z}{\lambda} Im\xi_t) \tag{2.46}$$

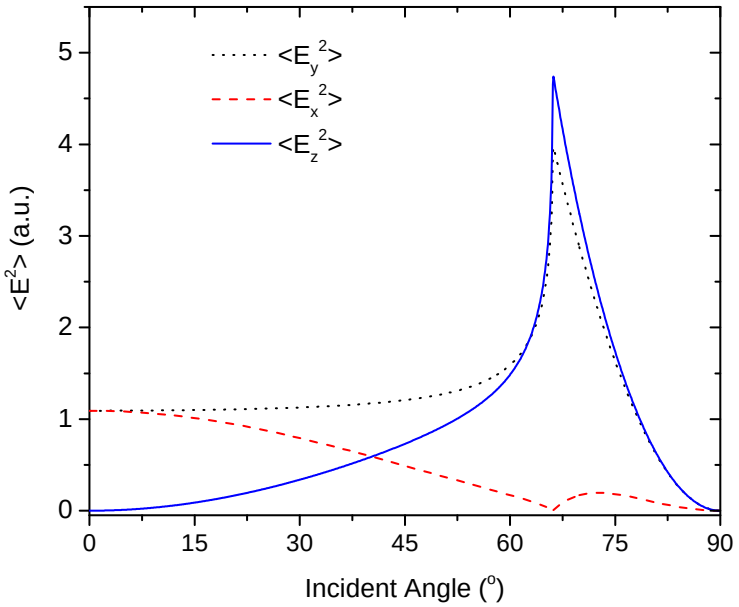

Figure 2.7. Variation of the mean-squared electric fields at the interface with respect to the incident angle of the electric field.[82]

2.6 Raman spectroscopy

2.6.1 Classical theory of Raman scattering

Theory. When a molecule interacts with an electromagnetic field, the total time-dependent induced electric dipole moment of the molecule is given by Equation 2.47,[83] where $p^{(n)}$ is the nth-order component of the total induced electric dipole moment. TIR Raman spectroscopy is a linear technique that deals with the first order induced dipole moment. The theory presented here is for linear Raman only.

$$p = p^{(1)} + p^{(2)} + p^{(3)} + ... \tag{2.47}$$

The first-order induced electric dipole moment ($p^{(1)}$) can be related to the incident electric field (E) of frequency ω by using Equation 2.48. The polarizability tensor of the molecule is α. It is first-order (second-rank) and is generally a function of the nuclear coordinates and the molecular vibrational frequencies. The relationship between the induced electric dipole and the incident field can be written in matrix form as given by Equation 2.49.[83] The components of Cartesian coordinates x, y, and z and $\alpha_{\rho\sigma}$'s are the components of the polarizability tensor.

$$p^{(1)} = \alpha \cdot E \tag{2.48}$$

$$\begin{bmatrix} p_x \\ p_y \\ p_z \end{bmatrix} = \begin{bmatrix} \alpha_{xx} & \alpha_{xy} & \alpha_{xz} \\ \alpha_{yx} & \alpha_{yy} & \alpha_{yz} \\ \alpha_{zx} & \alpha_{zy} & \alpha_{zz} \end{bmatrix} \times \begin{bmatrix} E_x \\ E_y \\ E_z \end{bmatrix} \tag{2.49}$$

The current scattering theory considers a molecule without any rotation. The nuclei of the molecule are allowed to vibrate around their equilibrium positions which will alter its polarizability. A Taylor expansion of each component of the tensor with respect to the normal coordinates of the vibration can be used to represent the variation (Equation 2.50).[83] The subscript 0 indicates the value at the equilibrium configuration of the molecule, while Q_k, Q_l, etc. are the normal coordinates of vibration associated with the molecular vibrational frequencies ω_k, ω_l, etc., respectively. Only the first-order derivative is considered here and the relationship between one component of the polarizability tensor and the normal coordinate Q_k is given in Equation 2.51.[83] The subscripts ρ, σ are removed from this equation. The first derivative of the tensor component with respect to the normal coordinate Q_k at the equilibrium position is $\alpha_k^{'}$.

$$\alpha_{\rho\sigma} = (\alpha_{\rho\sigma})_0 + \sum_k \left(\frac{\partial \alpha_{\rho\sigma}}{\partial Q_k}\right)_0 Q_k + \frac{1}{2}\sum_{k,l}\left(\frac{\partial^2 \alpha_{\rho\sigma}}{\partial Q_k \partial Q_l}\right)_0 Q_k Q_l + ... \tag{2.50}$$

$$\alpha_k = \alpha_0 + \alpha_k^{'} Q_k \tag{2.51}$$

$$\alpha_k^{'} = \left(\frac{\partial \alpha_{\rho\sigma}}{\partial Q_k} \right)_0 \tag{2.52}$$

The normal coordinate and the incident electric field are expressed in Equations 2.53-2.54, respectively. The frequency of Q_k is ω_k and δ_t is a phase factor. When writing Equation 2.53 we assume a simple harmonic motion.

$$Q_k = Q_{k_0} cos(\omega_k t + \delta_t) \tag{2.53}$$

$$E = E_0 cos\omega t \tag{2.54}$$

From Equations 2.48, 2.51, 2.53, and 2.54 we obtain a new expression for $p^{(1)}$ given in Equation 2.55.[83]

$$p^{(1)} = \alpha_0 E_0 cos\omega t + \frac{1}{2} \alpha_k^{'} E_0 Q_{k_0} \{ cos[(\omega + \omega_k)t + \delta] + cos[(\omega - \omega_k)t - \delta] \} \tag{2.55}$$

The first term on the right-hand side describes the Rayleigh scattering that is elastic and independent of the molecular vibrations. The second and third terms show that the scattered photons have a frequency that is different from that of the incident electric field. The scattering process associated with the frequency $\omega + \omega_k$ is called the anti-Stokes Raman scattering, while the one associated with $\omega - \omega_k$ is termed the Stokes Raman scattering. The Raman scattering is inelastic and frequency dependent. Figure 2.8 is an energy level diagram showing the Stokes Raman, Rayleigh, and anti-Stokes Raman scattering.

Vibrational selection rule. Equations 2.52 and 2.55 divulge that for a vibrational mode corresponding to the normal coordinate Q_k to be Raman active $\alpha_k^{'}$ should be non-zero.[83;84] This condition means that the first derivative of at least one component of the Raman tensor with respect to a normal coordinate

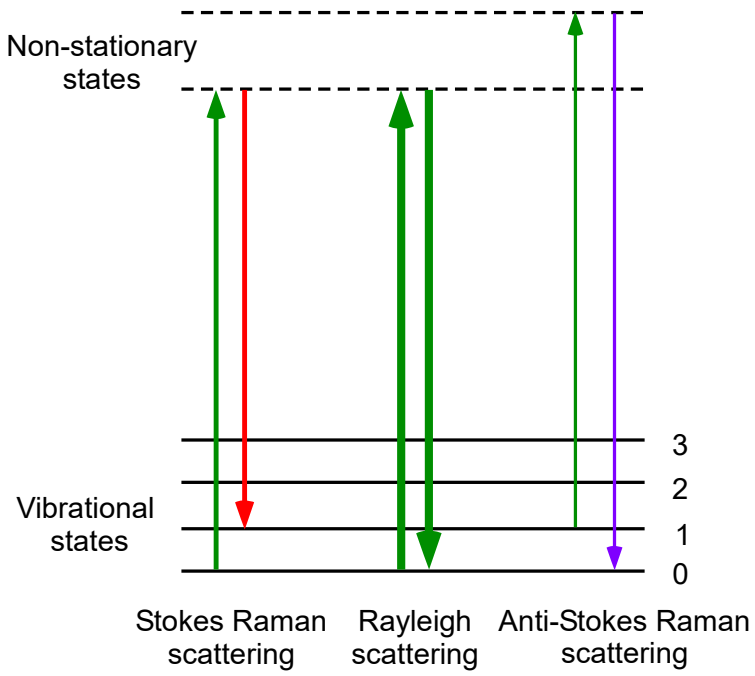

Figure 2.8. Energy level diagram for Stokes Raman, Rayleigh, and Anti-Stokes Raman scattering.

is non-zero when the atoms pass their equilibrium position.

2.6.2 Quantum mechanical theory of Raman scattering

Theory. In the quantum mechanical theory of Raman scattering, the molecules are treated quantum mechanically while the electromagnetic fields are treated classically. The transition electric dipole is used instead of the induced electric dipole. The total transition electric dipole moment for the transition from the initial state i to the final state f can be represented by Equation 2.56,[83] where $(p^{(n)})_{fi}$ is the nth-order component of the total dipole moment. Let $\psi_i^{'}$ and $\psi_f^{'}$ be the perturbed time-dependent wave functions of the molecule in the initial and final states, respectively. Their mathematical forms are given in Equations 2.57 and 2.58.[83] The unperturbed initial and final states of the molecule are ψ_i^0 and ψ_f^0, respectively, while ψ_i^n and ψ_f^n indicate the nth-order modification to the

ψ_i^0 and ψ_f^0 wave functions, respectively.

$$(p)_{fi} = (p^{(1)})_{fi} + (p^{(2)})_{fi} + (p^{(3)})_{fi} + ... \tag{2.56}$$

$$\psi_i^{'} = \psi_i^0 + \psi_i^1 + ... + \psi_i^n \tag{2.57}$$

$$\psi_f^{'} = \psi_f^0 + \psi_f^1 + ... + \psi_f^n \tag{2.58}$$

The current study is concerned only with the transition electric dipole moment up to the first order and is expressed by Equation 2.59,[83] in which $\hat{p}$ is the electric dipole moment operator. The perturbation is caused by the time-dependent electric field of frequency ω.

$$(p)_{fi} = \left\langle \psi_f^{'} | \hat{p} | \psi_i^{'} \right\rangle = \left\langle \psi_f^0 | \hat{p} | \psi_i^1 \right\rangle + \left\langle \psi_f^1 | \hat{p} | \psi_i^0 \right\rangle \tag{2.59}$$

The $(\alpha_{\rho\sigma})_{fi}$ component of the general polarizability tensor $(\alpha)_{fi}$ is given in Equation 2.60,[83] where ψ_i, ψ_r, ψ_f are the wave functions of states i, r, f, respectively. The components of the electric dipole moment operator are $\hat{p}_\rho$ and $\hat{p}_\sigma$, and Γ_r is defined as the line width of the transition. A relationship that is important to note is $\omega_{fi} = \omega_{ri} - \omega_{rf} = (\omega_r - \omega_i) - (\omega_r - \omega_f)$. If ω_{fi} is negative or positive, anti-Stokes or Stokes Raman scattering occurs. A zero value of ω_{fi} tells us about the occurrence of Rayleigh scattering. Opposite signs of $i\Gamma_r$ are used to satisfy the fundamental physical principles.[83]

$$(\alpha_{\rho\sigma})_{fi} = \frac{1}{\hbar} \sum_{r \neq i,\, f} \{ \frac{\langle \psi_f | \hat{p}_\rho | \psi_r \rangle \langle \psi_r | \hat{p}_\sigma | \psi_i \rangle}{\omega_{ri} - \omega - i\Gamma_r} + \frac{\langle \psi_f | \hat{p}_\sigma | \psi_r \rangle \langle \psi_r | \hat{p}_\rho | \psi_i \rangle}{\omega_{rf} + \omega + i\Gamma_r} \} \tag{2.60}$$

Vibrational selection rule. The component of the transition polarizability tensor can be written in the form of Equation 2.61. For a vibrational transition to be Raman active, at least one of the components of the transition polarizability tensor represented generally by Equation 2.61 must be non-zero.[83]

This condition means that the triple products $\Gamma(\psi_f) \times \Gamma(\alpha_{\rho\sigma}) \times \Gamma(\psi_i)$ contain the totally symmetric representation A_1 (Equation 2.62)

$$(\alpha_{\rho\sigma})_{fi} = \langle \psi_f | \hat{\alpha}_{\rho\sigma} | \psi_i \rangle \tag{2.61}$$

$$A_1 \subset \Gamma(\psi_f) \times \Gamma(\alpha_{\rho\sigma}) \times \Gamma(\psi_i) \tag{2.62}$$

2.7 Target factor analysis

Target Factor Analysis. TFA is applicable to data that can be written in the form of a linear combination of different parameters. TIR Raman spectroscopy is a linear vibrational technique, making the application of TFA to obtained spectra possible. By finding principal components contributing to the measured results, a data matrix $D_{r\times c}$ is decomposed into the sum of a reduced data matrix ($\bar{D}_{r\times c}$) and an error matrix ($E_{r\times c}$) associated with experimental measurements (Equation 2.63).[22]

$$D_{r\times c} = \bar{D}_{r\times c} + E_{r\times c} \tag{2.63}$$

As a result of the decomposition process, the reduced data matrix ($\bar{D}_{r\times c}$) can be written in the following form:[85]

$$\bar{D}_{r\times c} = \bar{U}_{r\times n}\bar{S}_{n\times n}\bar{V}'_{c\times n} = \bar{R}_{r\times n}\bar{C}_{n\times c} \tag{2.64}$$

where r and c are the number of rows and columns of the data matrix, respectively. The number of real components that are responsible for the data matrix is denoted as n. The prime symbol indicates a transpose of the matrix. In the current research, n is equal to one for single component systems and is equal to two for the mixed surfactant system of DDAO and TX-100. The reduced

row ($\bar{R} = \bar{U}\bar{S}$) and column ($\bar{C} = \bar{V}'$) matrices (also called the abstract row and column matrices) are mathematical solutions of the decomposition process and have no physical meaning. They need to be transformed into data that gives insight about the chemical system. The required transformation is done via a target transformation that is of special interest in chemistry.[22] Matrix $\bar{D}$ can be rewritten as

$$\bar{D} = \bar{R}\bar{C} = \bar{R}TT^{-1}\bar{C} = \hat{X}\hat{Y} \tag{2.65}$$

where

$$\hat{X} = \bar{R}T \tag{2.66}$$

$$\hat{Y} = T^{-1}\bar{C} \tag{2.67}$$

In Equation 2.65, T is the transformation matrix consisting of different vectors t_l, and $\hat{X}$ and $\hat{Y}$ are new row and column matrices, respectively, that are physically meaningful. The lth column of the new row matrix $\hat{X}$ in Equation 2.66 is obtained using the following equation:

$$\hat{x}_l = \bar{R}t_l \tag{2.68}$$

The least-squares procedure to obtain the best transformation vector t_l is described in detail in the book by Malinowski.[22] According to this procedure, a set of target (test) vectors x_l are first obtained from experimental measurements. To find the best transformation vector t_l the least-squares procedure is used to minimize the deviation between x_l and $\hat{x}_l$, the predicted test vector corresponding to the test (target) vector x_l. After several mathematical derivations, the transformation vector obtained is

$$t_l = (\bar{R}'\bar{R})^{-1}\bar{R}'x_l \tag{2.69}$$

From the procedure used, each vector t_l of the transformation matrix T is obtained independently from other vectors of T. It is also from this procedure that any suspected target vector corresponding to a possible component of a mixture can be tested and verified. The criterion for determining if a target vector is a real component of the data matrix is discussed in the data processing section.

2.8 Adsorption isotherm

The adsorption of pure surfactants at the silica/water interface can be described by the Langmuir model (Equation 2.70).[86] In the Langmuir equation, Γ_∞ is the maximum adsorbed amount and c is the bulk surfactant concentration. The Langmuir constant, K_L, is the ratio of the adsorption and desorption rate constants.

$$\frac{\Gamma}{\Gamma_\infty} = \frac{K_L c}{1 + K_L c} \tag{2.70}$$

The Langmuir mode, however, does not take into account the interactions between adsorbed molecules. In an attempt to improve the Langmuir modes, Frumkin introduced a parameter ω to account for the interactions between two adsorbed molecules on the surface. The modified Langmuir isotherm (Frumkin isotherm) is described by Equation 2.71. A value of $\omega > 4$ indicates phase separation at the interface.[40]

$$\frac{\Gamma}{\Gamma_\infty} = \frac{K_L e^{\omega\Gamma/\Gamma_\infty} c}{1 + K_L e^{\omega\Gamma/\Gamma_\infty} c} \tag{2.71}$$

Equation 2.71 can be rearranged to obtain the form given in Equation 2.72. In the current study, the parameters Γ_∞, K_L, and ω are obtained by fitting

the adsorption isotherm to Equation 2.72.

$$c = \frac{\Gamma}{K_L(\Gamma_\infty - \Gamma)})e^{(-\omega\Gamma/\Gamma_\infty)} \tag{2.72}$$

Chapter 3

Experiments

3.1 TIR Raman setup

The basic components of the TIR Raman setup are shown in Figure 3.1. In this setup, a 532 nm continuous wave beam from a diode-pumped, solid-state laser passes through a half-wave plate and after reflecting from several mirrors, is focused on the solid/water interface using a biconvex lens (f = +60 mm). The diameter of the incident beam is 2.25 ± 0.23 mm at the laser head and is 4.50 ± 0.45 mm at the biconvex lens.[87] The scattering photons are collected by a collection system consisting of a 50x ultra long working distance (ULWD) objective (Mitutoyo, 0.55 N.A., 17 mm working distance), a lens tube compartment (250 mm long) and a focusing lens (f = 75 mm), and finally reflected to a spectrograph by a mirror at the entrance of the spectrograph (entrance slit width = 100 μm). The spectrograph (HoloSpec f/1.8i, Kaiser Optical Systems, Inc.) has a rejection filter (notch filter) to remove the photons from the incident beam and the Rayleigh scattering, and is combined with a CCD camera (Andor iDus, Andor Technology) to detect the Stokes Raman light resolved by a high frequency transmission grating (2600 grooves/mm).

Polarized Raman measurements were performed by rotating the half-wave plate and polarizer to obtain S_x, S_y, P_x, and P_y polarization combinations. S

and P are the polarization states of the incident light, and the subscripts, x and y, are the polarization states of the Raman photons with respect to the Cartesian coordinates in the detection system. The letters S or P indicates that the incident electric field is normal to the plane of incidence or along the plane of incidence, respectively. Raman tensor elements are sensitive to the orientation and conformation of the interface molecules so that variations in structure and conformational order can be revealed through polarized Raman spectra.

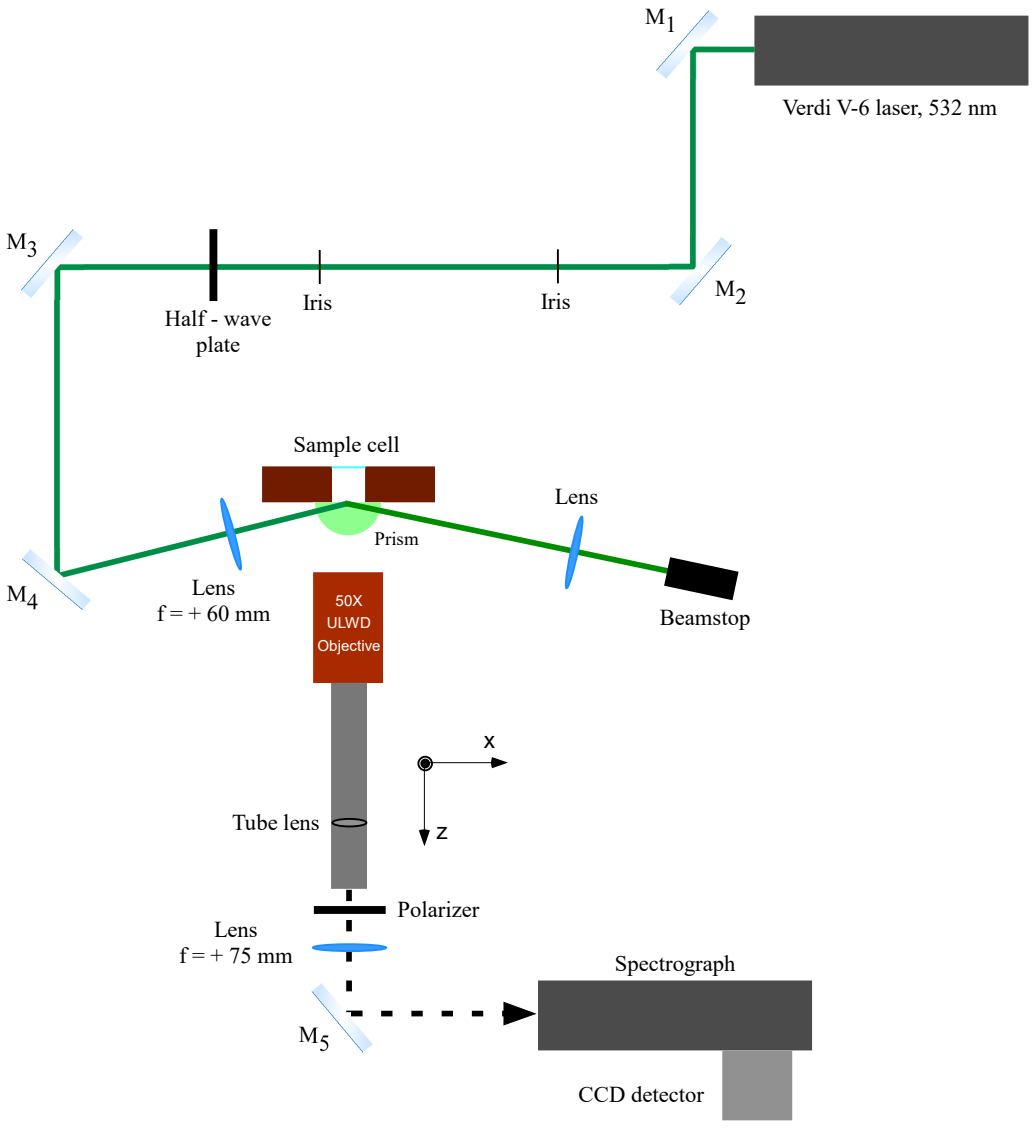

Figure 3.1. TIR Raman setup. M_{1-5} are mirrors.

A one-inch diameter fused-silica IR grade hemispherical prism (ISP Optics) was used as the solid substrate in the current study. It does not have a strong Raman signal in the spectral region of interest (2700-3100 cm^{-1}), and is optically transparent and non-fluorescent. The use of a hemispherical prism minimizes optical aberrations in the incident beam and helps to collect photons within the numerical aperture of the objective.

Figure 3.2 shows part of the Raman setup. The spectrograph and CCD camera are shown in Figure 3.3.

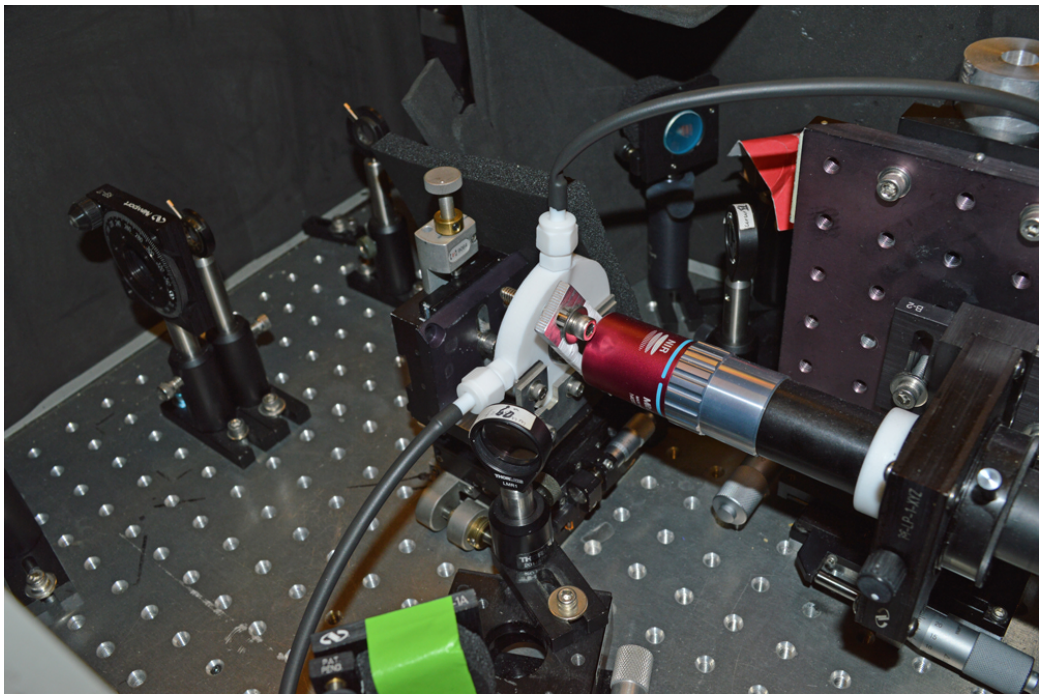

Figure 3.2. Part of the TIR Raman setup.

In all TIR Raman measurements an incident angle of 73.0° was used. The refractive indices of the silica substrate and water are 1.46 and 1.33, respectively, when a 532 nm laser is used. The incident angle is about 7.0° above the critical angle (65.8°), giving an effective penetration depth $(d_p)_{eff}$ of about 100 nm. The angle used here satisfies the requirements for the total internal reflection, the transmission coefficient, and the penetration depth of the focused laser beam.

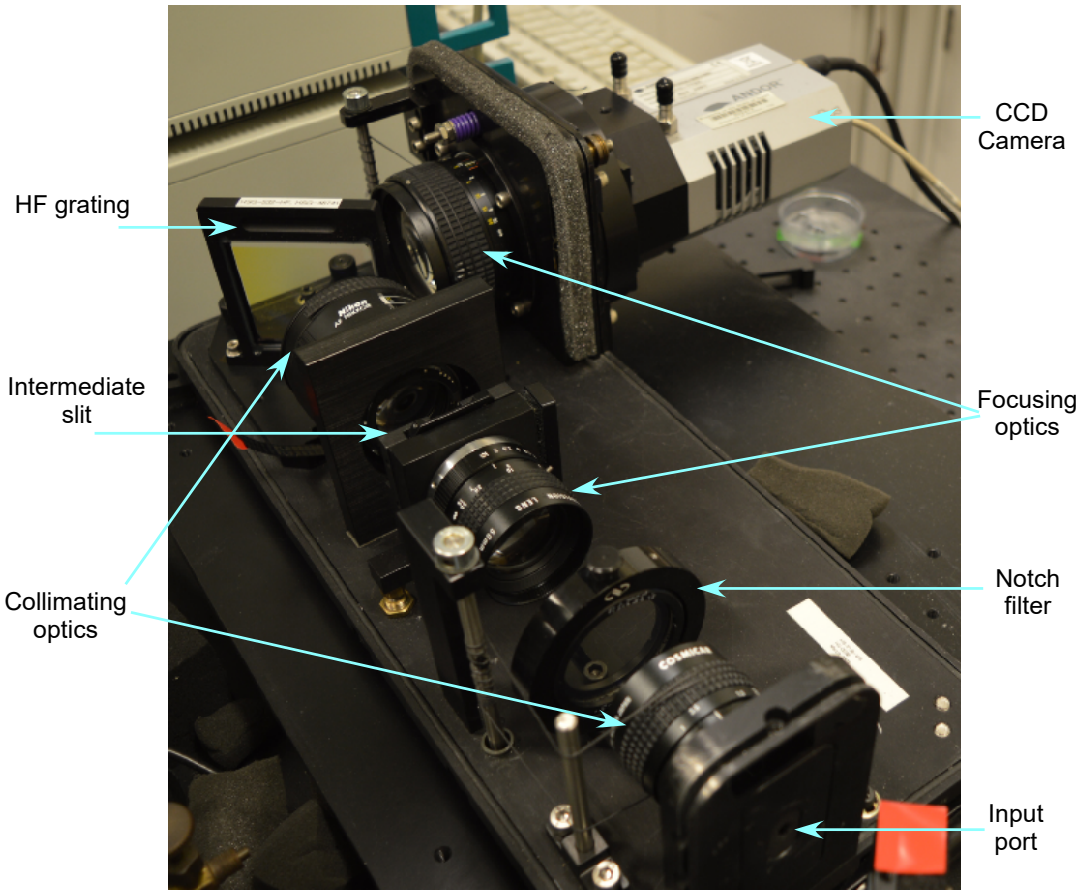

Figure 3.3. Spectrograph and CCD camera of the TIR Raman setup.

The first order (second-rank) Raman tensor has nine elements and polarized Raman experiments with different polarization selections on the incident and detection sites help detect these effective tensor elements. While the S_y-polarized measurements probe the α'_{yy} (also α'_{xx} in the case of an adsorbed layer isotropic to the interface (xy)) element of the Raman tensor, measurements with the S_x polarization combination detect the α'_{xy} tensor element. The α'_{yx} and α'_{yz} tensor elements are determined from spectra collected using the P_y polarization combination. The final polarization combination, P_x, is used to probe the α'_{xx} and α'_{xz} elements. For a uniaxial adsorbed layer some of the Raman tensor elements are equivalent and are detected in the above polarized measurements.

3.2 Raman cell

Figure 3.4 shows an illustration of the Raman cell and sample pumping system. The Raman cell is made from a cylindrical Teflon piece that has a 0.5-inch hole at the center to contain the samples. The left side of the hole is sealed by a quartz window and o-rings to check the level of liquid samples in the cell. The right side of the hole is attached to the fused silica prism that is the solid substrate in the current study. To avoid contamination, the liquid samples are pumped from their container into the Raman cell by a peristaltic pump (Lab-Line Instruments, Inc.) at a rotation speed of 80 r.p.m.

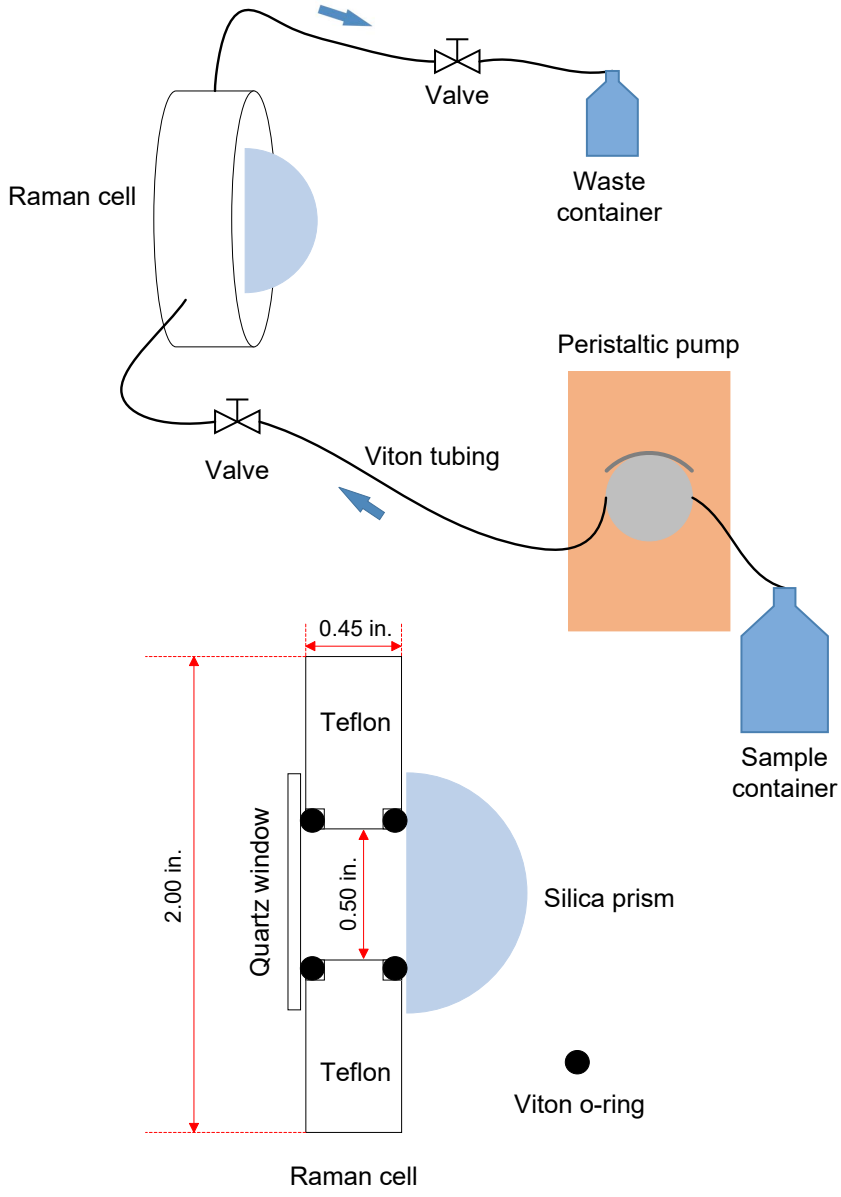

Figure 3.4. Illustration of the Raman cell and sample pumping system.

3.3 Calibration of the TIR Raman setup

The TIR Raman spectrometer was calibrated following the ASTM standard E1840-96.[88] Two samples used in the calibration were cyclohexane and a mixture of 50/50 toluene - acetonitrile. The samples were contained in vials placed at the location of the Raman cell. Raman measurements of these chem-

icals were taken with a laser power of 30 mW. The spectra of the two samples after calibration are given in Figures 3.5 and 3.6. Reference spectra are shown in Figures 3.7 and 3.8.

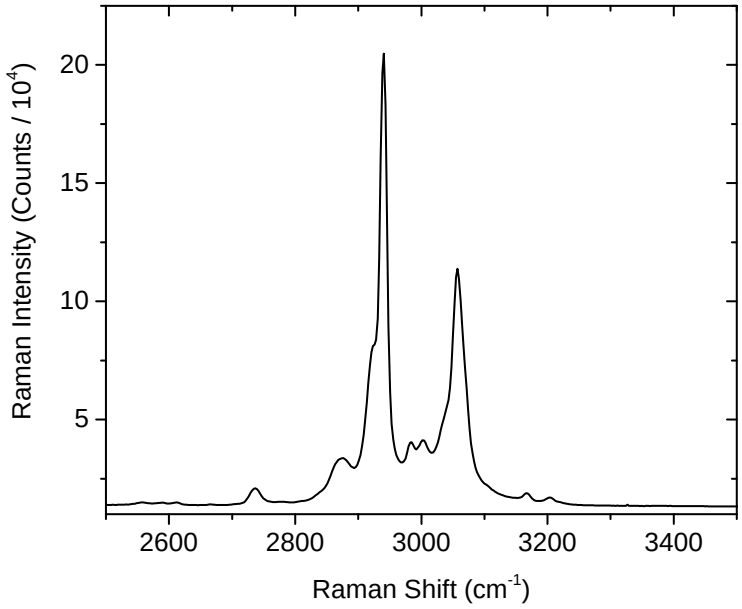

Figure 3.5. Raman spectrum of mixture of 50/50 toluene - acetonitrile.

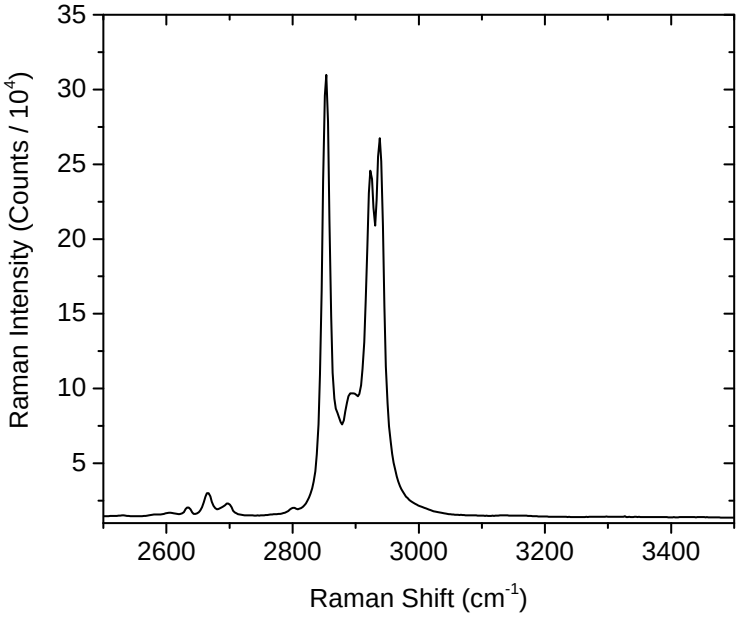

Figure 3.6. Raman spectrum of Cyclohexane.

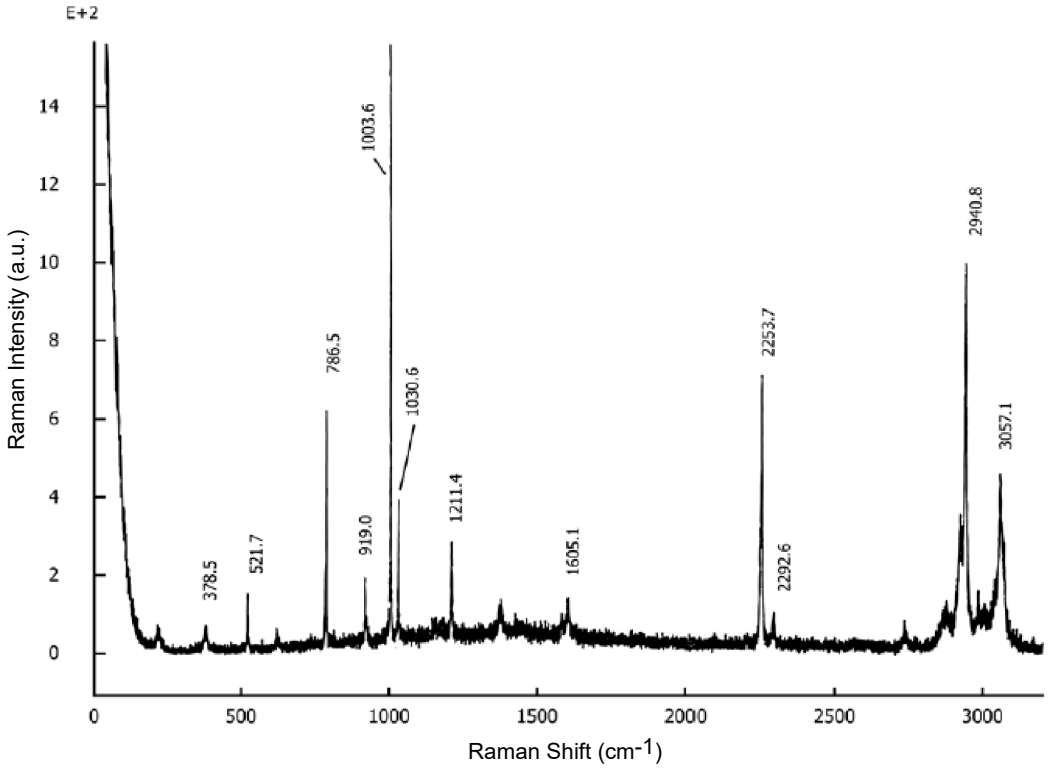

Figure 3.7. Raman spectrum of mixture of 50/50 toluene-acetonitrile.[88]

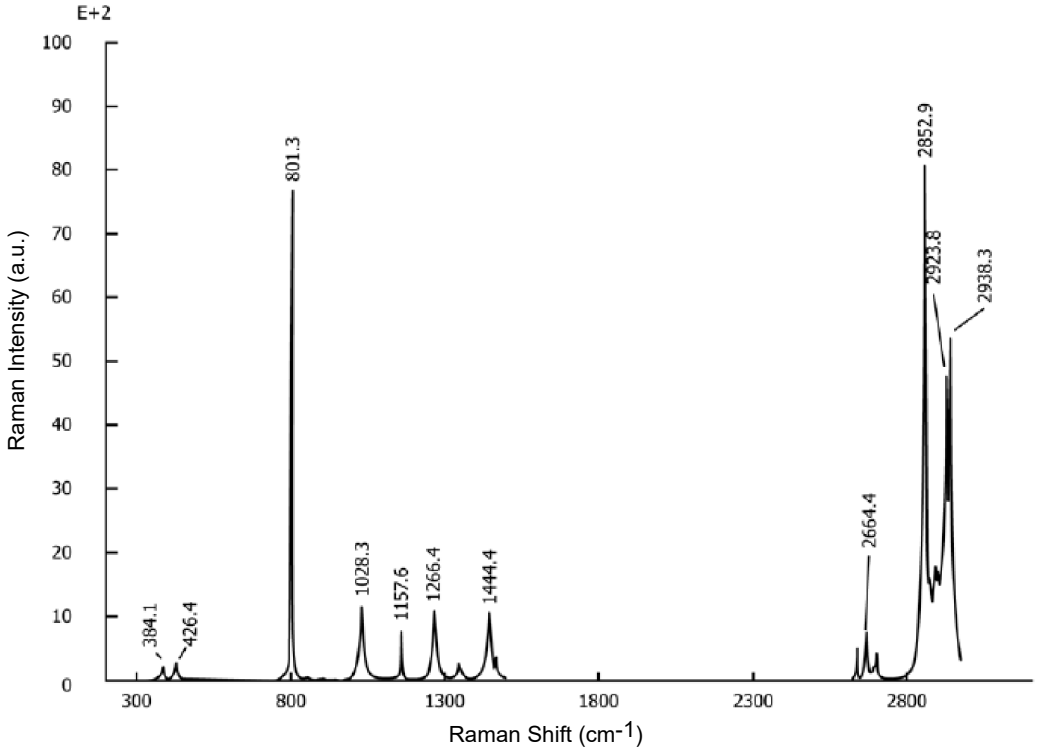

Figure 3.8. Raman spectrum of cyclohexane.[88]

3.4 Sample preparation of TIR Raman experiments

Dimethyldodecylamine oxide (99.93%) was obtained from Anatrace and was used as received. Triton X-100 (BioXtra) was supplied by Sigma-Aldrich and was not purified further. Sodium chloride (Mallinckrodt) contained in a petri dish was baked in an annealing cycle oven at 570 °C for one hour to eliminate organic contaminants in the salt. The surfactant solutions used in Raman experiments were diluted from stock solutions to different concentrations using ultra-pure water obtained from Millipore filtration units (18.2 MΩ · cm resistivity). All experiments were done at native pH. For mixtures of DDAO and TX-100, the DDAO bulk concentration was kept constant (0.30 mM and 1.00 mM in the first and second sets of mixed surfactant experiments, respectively) while the TX-100 concentration was varied. The low DDAO concentration (0.30 mM) was used to study the effect of a small amount of DDAO on the adsorption of TX-100 and it also gave high enough DDAO Raman signal for the data analysis. TIR Raman spectra of mixed surfactant solutions with a higher concentration of DDAO (1.00 mM) were measured for comparison.

The prism and Teflon cell were cleaned with a mixture of sulfuric and nitric acids (50/50 v/v) for several hours and then rinsed and leached with copious water before performing Raman measurements. All glassware used were cleaned with Liquinox (Alconox) and rinsed thoroughly with ultra-pure water. They were then baked in the annealing cycle oven up to 570 °C for several hours.

3.5 Raman measurement

The TIR Raman spectrum of ultra-pure water was taken before introducing surfactant solution into the Raman cell on the day of the experiments. Each

Raman spectrum was collected for 5 minutes and it was repeated until the Raman intensity was almost constant (the adsorption process was at equilibrium) for surfactant solution measurements. Four polarization combinations were used in the experiments of pure DDAO solution; however, in the case of mixed surfactants, the polarizer was removed and only S-polarized light was used in the experiment to increase the signal-to-noise ratio. The laser power used was 0.7 W and all Raman spectra were collected at room temperature. Table 3.1 and Figure 3.9 show values used in the experimental setup of the CCD camera.

Table 3.1. Acquisition setup

Parameter	Value
Acquisition mode	Accumulate
Triggering	Internal
Readout mode	Multi-track
Exposure time (secs)	30.0000
Number of accumulations	10
Accum cycle time (secs)	30.0761
Shift speed (μsecs)	64.25
Readout rate	100 kHz at 16-bit
Pre-amplifier gain	1.6x

3.6 Data processing of Raman spectra

3.6.1 Data preprocessing

Raman spectra were preprocessed before being treated by TFA. The data preprocessing step is very important in factor analysis and clearly affects the outcome. Figure 3.10 shows an example of background subtracted and base-

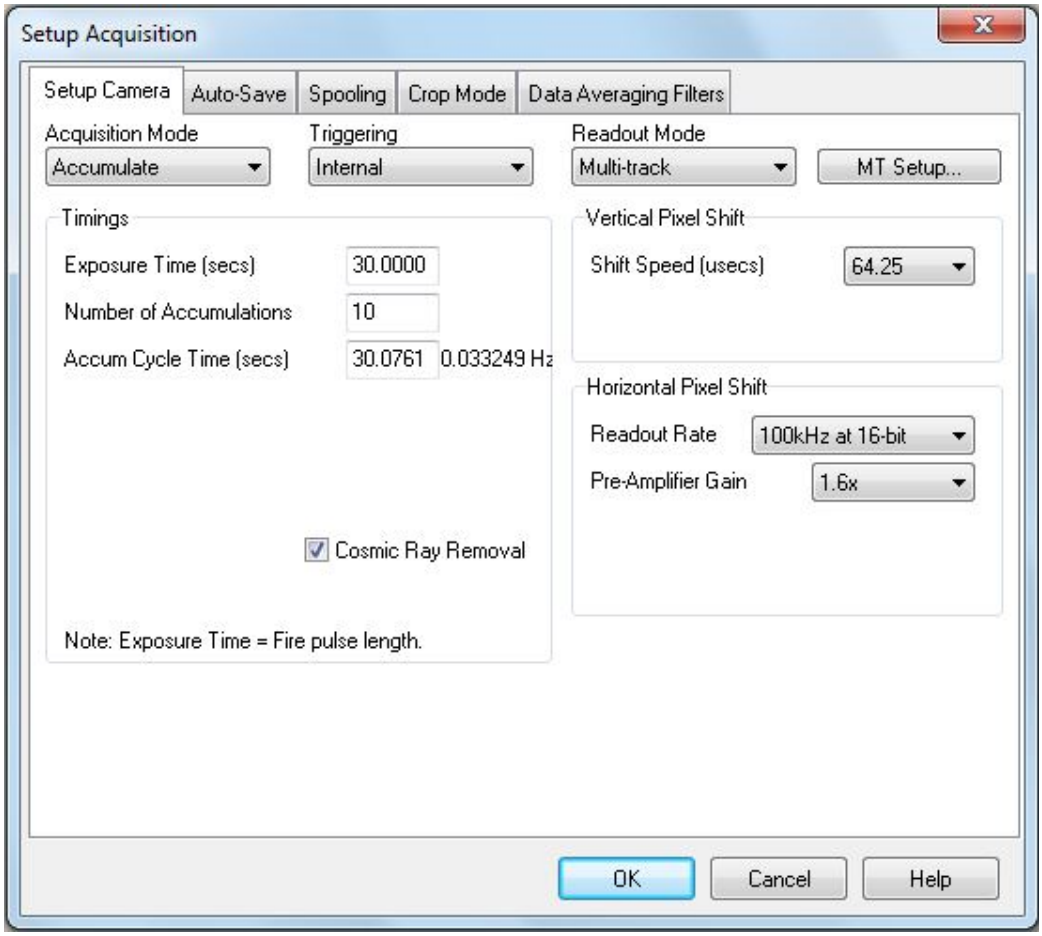

Figure 3.9. Acquisition setup

line corrected Raman spectra of TX-100 and DDAO mixture. The background-subtracted spectrum (the surfactant spectrum) was obtained by subtracting the water signal from the sample spectrum (the spectrum of water and surfactant molecules). Due to temperature fluctuations, vibrations, refractive index changes between measurements of pure water and sample spectra, and so on, obtaining a flat baseline for the background-subtracted spectrum was not expected, so a baseline correction was needed. An asymmetric least squares (ALS) smoothing method incorporated in OriginPro software was then used for baseline correction of the surfactant spectrum.[89;90] Figure 3.11 shows an example of asymmetric least squares baseline correction of a background corrected Raman spectrum of DDAO obtained from an S_y-polarized measurement.

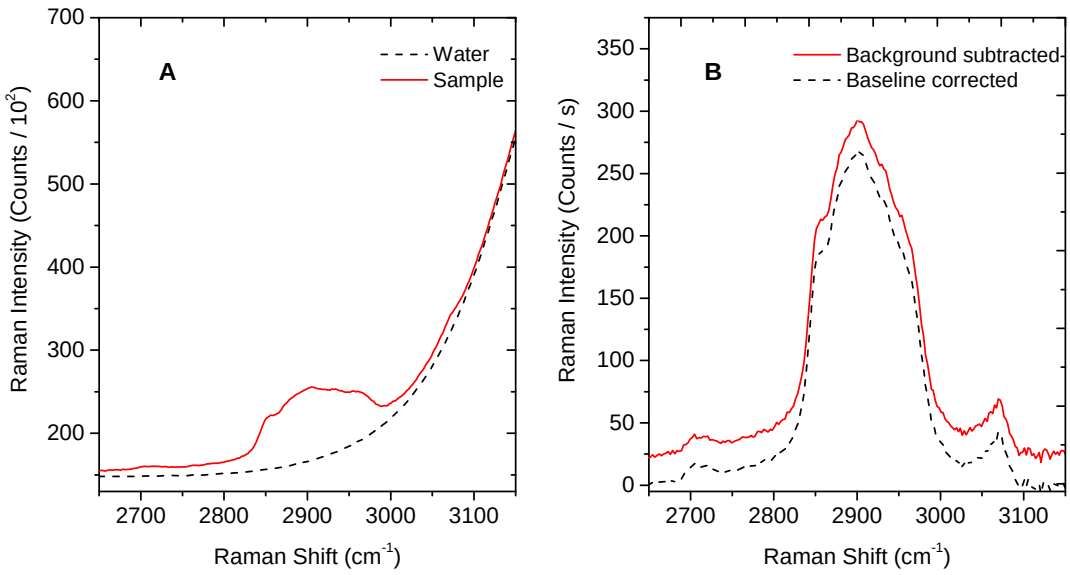

Figure 3.10. TIR Raman spectra: (A) water and mixed sample spectra; (B) background subtracted and baseline corrected spectra of a mixed sample of TX-100 and DDAO. The bulk solution contained 0.30 mM DDAO and 0.20 mM TX-100. The ALS technique was used for the baseline correction.[89]

3.6.2 Target factor analysis

Target factor analysis was applied to both single and mixed surfactant spectra. For the adsorption study of pure surfactant, the number of components (n) is equal to one and the target (test) vector is the interfacial surfactant spectrum at the highest bulk surfactant concentration. The target vectors in the mixed surfactants are the highest concentration pure spectra of TX-100 and DDAO and the number of components (n) is equal to two. The MATLAB codes for target factor analysis are provided in the book by Malinowski.[22]

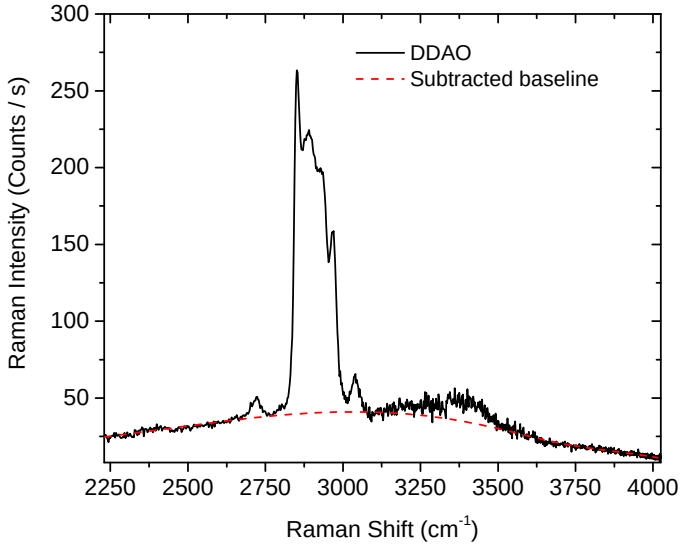

Figure 3.11. Asymmetric least-squares baseline correction of the background corrected Raman spectrum of DDAO obtained from the S_y-polarized measurement.

The first step in TFA is principal factor analysis (PFA), which is used to determine the number of factors responsible for the data and to decompose the data matrix. In this step, singular value decomposition decomposes the data matrix into the $\bar{U}$, $\bar{S}$, and $\bar{V}$ matrices. The abstract row ($\bar{R} = \bar{U}\bar{S}$) and column ($\bar{C} = \bar{V}'$) matrices obtained after the singular value decomposition have no physical meaning and are illustrated in Figures 3.12 and 3.13 using mixtures of DDAO and TX-100. These figures show that the columns of the abstract row matrix are not spectra of DDAO and TX-100. The component weights are also lack of physical meaning when they have negative values.

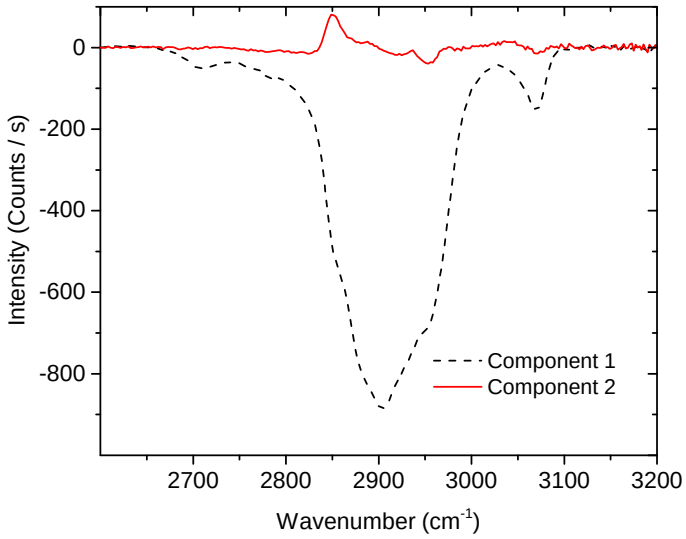

Figure 3.12. The columns of the abstract row matrix plotted versus wavenumber. These abstract columns were obtained from the principal factor analysis of Raman spectra of DDAO and TX-100 mixtures. The DDAO concentration was 0.30 mM and the TX-100 concentration was varied.

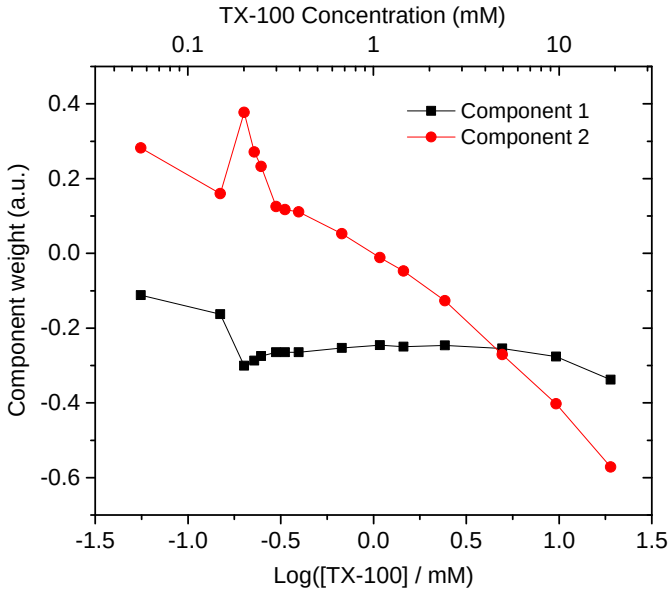

Figure 3.13. Component weights of components 1 and 2 plotted versus log([TX-100]/mM). These abstract rows were obtained from the principal factor analysis of Raman spectra of DDAO and TX-100 mixtures. The DDAO concentration was 0.30 mM and the TX-100 concentration was varied.

The test (target) vectors were then used to build the transformation matrix to convert abstract matrices into physically significant data. In order to confirm the existence of a component (represented by a test vector) in the chemical systems, an empirical function called SPOIL was used to evaluate all target spectra used,[22] and is defined in the following equation.

$$SPOIL = \frac{RET}{EDM} \simeq \frac{RET}{REP} \tag{3.1}$$

In this equation, EDM is the error contributed by the data matrix, RET is the real error in the target (test) vector and REP is the root mean square of the predicted vector. There is always certain error in the experimental data that makes the pure test vector (the test vector that has no error) different from the predicted test vector ($\hat{x}_l$). In this case, the error in the predicted vector comes from the error in the data matrix, and thus EDM is close to REP. A SPOIL value between 0.0 and 3.0 indicates that the tested target is acceptable. It is moderately acceptable if its SPOIL value is between 3.0 and 6.0. An excessive error in the reproduced data will occur if the SPOIL value is larger than 6.0. The tested vector in this case is unacceptable. The tfa.m Matlab program was used to calculate all values in Equation 3.1.[22] Figure 3.14 shows the predicted (refined) and target S_y-polarized Raman spectra of DDAO used in the target factor analysis. The two spectra match very well, indicating a successful target transformation.

The row matrix $\hat{X}$ obtained from the target transformation contains the predicted (refined) vector, and the column matrix $\hat{Y}$ consists of component weights (loadings) of refined spectra in the data matrix. The component weights (loadings) are absolute values of no physical meaning. They can, in some cases, be converted into surface excess using component weight values above the critical micelle concentration (cmc). In this paper, the conversion was realized for TX-

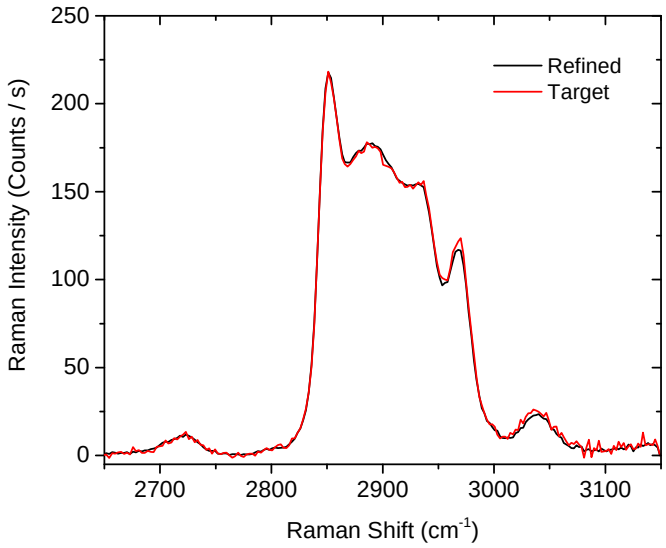

Figure 3.14. Predicted (refined) and target S_y-polarized Raman spectra of DDAO used in the target factor analysis of pure DDAO spectra.

100; however, TX-100 does not satisfy one of the four assumptions required for a successful conversion, that surface excesses should not be considered as exact values.

3.7 Raman experiments with ITO coating

Studies of surfactant adsorption at a solid-liquid interface have been done using various techniques,[62;91] and adsorption under the influence of different factors, such as type of substrate,[80;92] surfactant head group,[69;93] alkyl chain length,[61;94] solution pH,[91] and electrolytes and counterions,[70] have been studied in great detail. However, in these studies the charges of the surfaces were only controlled before surfactant solutions were introduced into the systems. The adsorption would affect the charge of the surface and the change in the surface charge would again affect the adsorption. It is not known how the adsorption process will be affected by different constant charges of the solid surface and how these charges change the optical properties of the interface. It is also interesting

to know how the adsorption process proceeds when the surface charge is kept constant and other factors, such as solution concentration, solution pH, electrolyte, and counterion, are changed. The answers to these questions are merit investigation due to their potential applications.

In the current study, an indium tin oxide (ITO) coating has been used for experiments in which the surface charge is controlled by an applied external voltage. The ITO material is electrically conductive and polarizable.[95] It is also optically transparent, allowing the combination of both electrochemistry and spectroscopy in the current study. Raman experiments at the ITO/water interface have been performed with two different configurations of the Raman cell. In the first, an index-matching fluid was inserted between a glass slide with a 1000 nm ITO coating and a fused silica IR grade hemispherical prism (Figure 3.15). The index matching fluid used here is a liquid that has a refractive index very close to that of the prism and the glass slide. The laser beam propagated through the prism, the index matching fluid, and the glass slide, and was refracted at the glass/ITO interface before being totally reflected at the ITO/water interface.

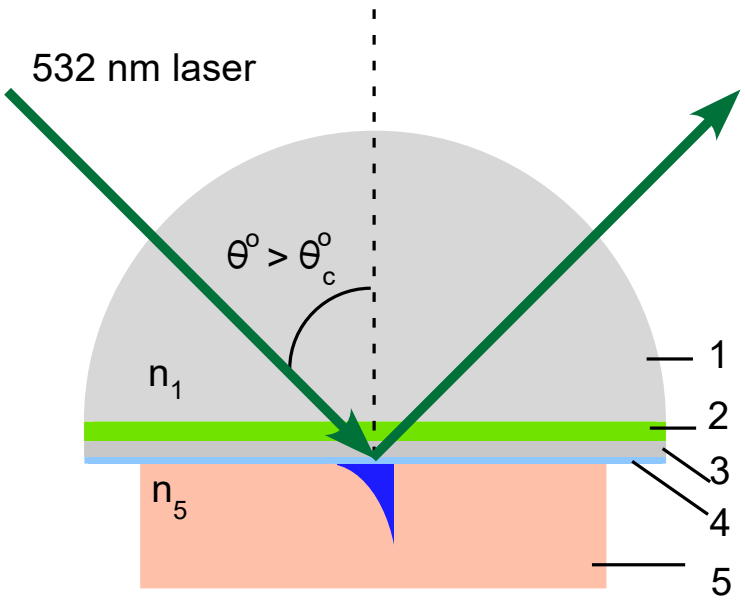

Figure 3.15. Schematic illustration of the TIR Raman experiment with ITO coating: (1) fused silica IR grade hemispherical prism, (2) index matching fluid, (3) glass substrate, (4) ITO coating, (5) aqueous solution.

In the second configuration, an ITO coating of about 180 nm was directly deposited on the flat side of a fused silica IR grade hemispherical prism (Figure 3.16). The deposition was performed by sputtering an ITO target in a vacuum chamber. The laser beam in the experiment refracted at the silica/ITO interface and then totally reflected at the interface between ITO and the aqueous solution.

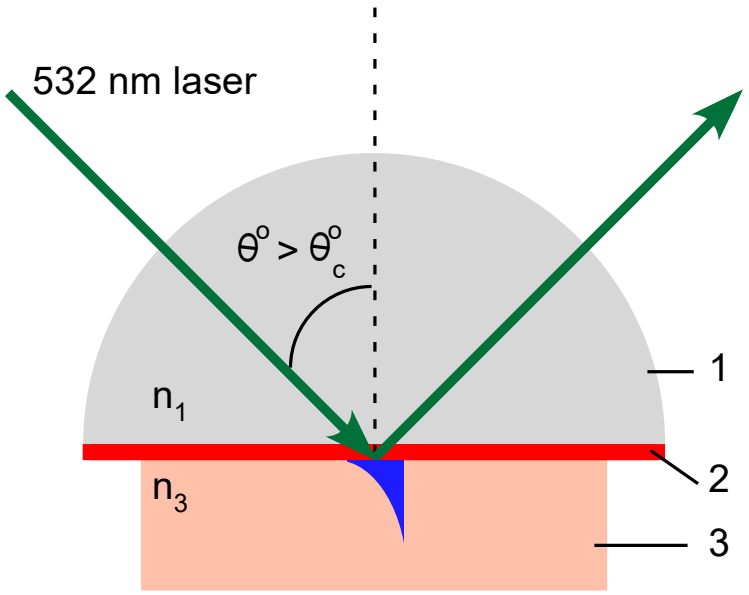

Figure 3.16. Schematic illustration of the TIR Raman experiment with the ITO coating: (1) fused silica IR grade hemispherical prism, (2) ITO coating, (3) aqueous solution.

The Raman cell used in the measurements with the ITO coating is illustrated in Figure 3.17. The counter electrode (CE) was a platinum wire and the reference electrode (RE) was a small silver/silver chloride electrode (PINE Research). The working electrode – the ITO coating on the flat side of the silica prism – was connected to the outside by inserting a small platinum foil between the ITO coating and a Viton o-ring. The potential of the working electrode was controlled by a potentiostat (Princeton Applied Research).

Raman experiments were performed while the potentiostat held the working electrode potential at certain values. The aqueous solution contained 0.1 M KCl to maintain the ionic strength of the solution.

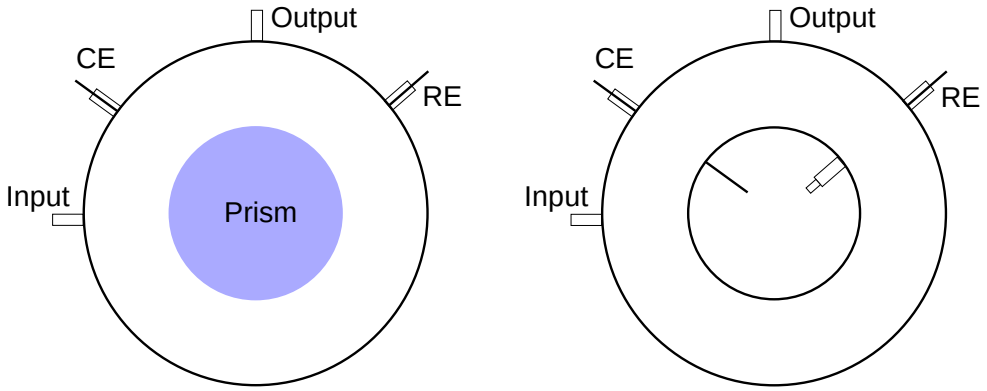

Figure 3.17. The Raman cell used in the measurements with the ITO coating: (CE) counter electrode, (RE) reference electrode. The working electrode was the ITO coating on the flat side of prism.

3.8 Sum frequency generation spectroscopy measurements

Sum frequency spectroscopy has been performed to detect the asymmetry of surfactant aggregates in the adsorbed layer. Figure 3.18 shows the geometry for the SFG experiment with a silica substrate. The 532 nm visible beam and tunable IR beam propagate through the silica window and overlap spatially and temporally at the silica/water interface to generate the SF beam. After being filtered by a short pass filter to remove the visible laser light, the SFG signal is collected by a photomultiplier tube and a gated integrator. The visible beam polarization is chosen by a half-wave plate. The IR beam polarization is chosen by an IR half-wave plate. Only the SFG beam (the output) is tuned using a linear polarizer.

SFG measurements for both DDAO and mixtures of DDAO and TX-100 solutions were performed. The IR wavenumber was scanned from 2750-3100 cm^{-1}. However, the spectra obtained do not show any peaks in the CH stretching region of the hydrocarbon chains of the surfactant molecules. It is unclear if the absence of vibrational peaks is due to the inversion symmetry of the adsorbed layer or due to the alignment of the SFG setup. The SFG spectrometer has since

been improved and future measurements would give us better insights into the adsorption of surfactants at the silica/water interface.

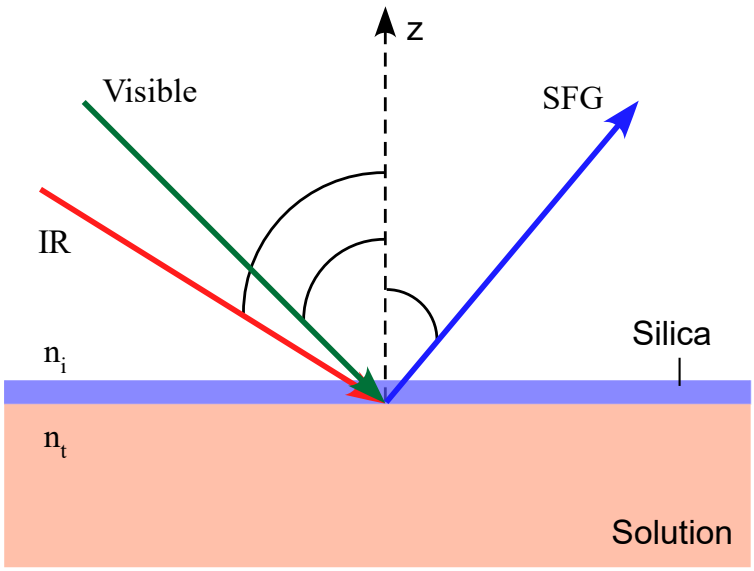

Figure 3.18. Geometry for SFG experiments.

3.9 Conductivity measurements

The formation of aggregates in the surfactant solution alters the solution properties and the adsorption of surfactant at the interface. If the changes in the surfactant solution are known, a better understanding of the solution dependence of the adsorption process at interface can be achieved. Conductivity results provide important parameters such as critical micelle concentration, degree of ion binding, and aggregation number.[96] While the critical micelle concentration reveals at which concentration micelles are formed, the degree of ion binding and aggregation number provide the size and charge of the micelles.

In the current research, conductivity measurements have been conducted by using a two-electrode cell (Figure 3.19). Two platinum (Pt) electrodes were immersed in the surfactant solutions and then connected to a potentiostat and a lock-in amplifier. The temperature of the cell was maintained by immersing it

in a water bath at 25 ± 0.1 °C. Figure 3.20 shows a photograph of the cell used in the conductivity experiments. Conductivity values of different solution concentrations were determined by measuring the impedance of the solutions. The impedance values were then fitted to determine the resistance of the surfactant solution.

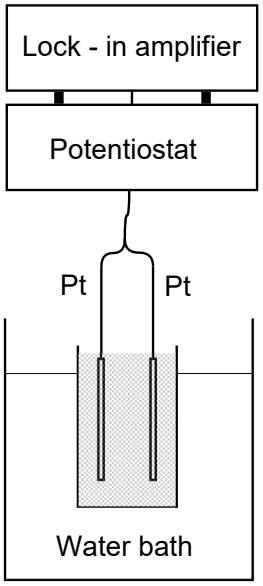

Figure 3.19. Schematic illustration of the electrochemical setup used in conductivity measurements of surfactant solutions. The two electrodes were flat platinum foil.

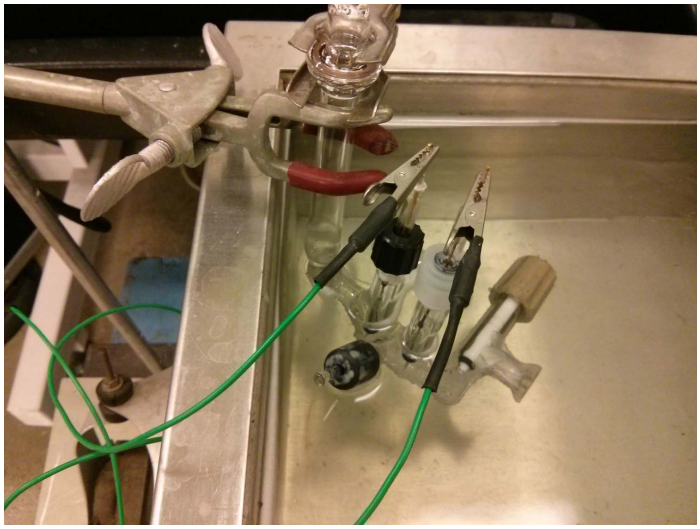

Figure 3.20. Photograph of the conductivity measurement cell.

The solution resistance is related to the conductivity via the following equation:

$$R_s = \frac{G}{\kappa} \tag{3.2}$$

where κ is the conductivity of the solution. A 0.1 M KCl solution of known conductivity value was used to determine the cell constant, G, in Equation 3.2. From R_s and G, conductivity is determined. The current cell works well for a solution of low impedance. However, for solutions of very low concentrations, the distance between the two electrodes in the cell is too large for the accurate impedance to be obtained. For high-impedance solutions, the two electrodes need to be closer to increase the conductance. A new cell has been designed for future research (Figure 3.21).

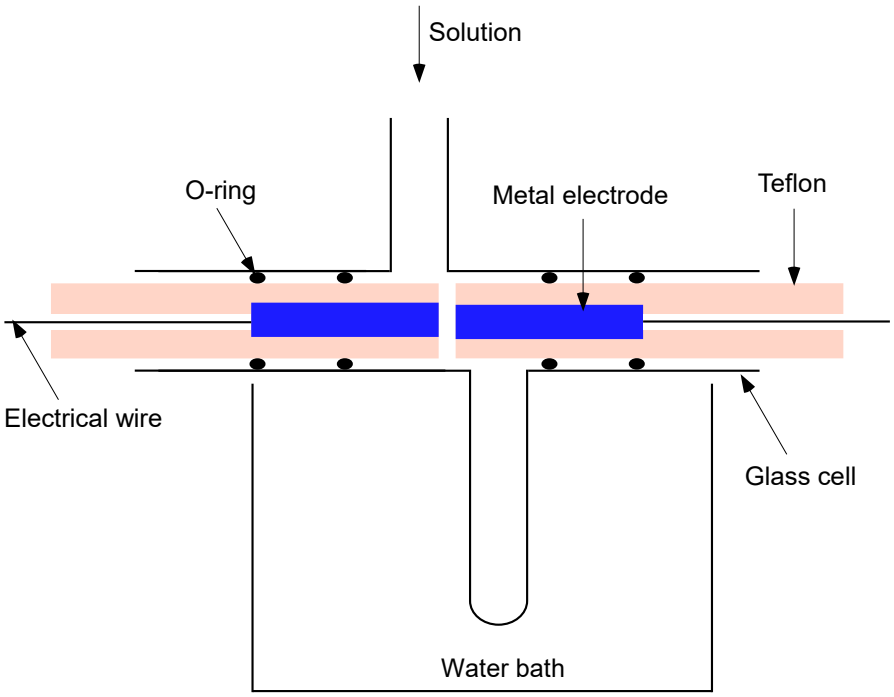

Figure 3.21. New conductivity measurement cell.

Chapter 4

Adsorption of Pure Surfactants

4.1 Adsorption of DDAO without added salt

4.1.1 DDAO spectra

Surfactant adsorption at the solid/liquid interface has been successfully studied by TIR Raman spectroscopy with much useful information acquired.[26;40;62;97;98] Although it is not an intrinsically surface sensitive technique, the control of the incident angle and the ability to correct for the bulk contribution make it a powerful method for studies of surface molecules.[99] Figures 4.1 and 4.2 show sets of Raman spectra of DDAO at the silica/water interface obtained from measurements with different polarization combinations. The bulk concentrations were from 0.05 mM to 2.55 mM. The detection limit is about 6 counts/s.

The C-H stretching region of alkyl chains is well characterized.[100;101] The peak positions and relative intensities of different vibrational modes on the Raman spectra reveals that the hydrocarbon chains of DDAO are in liquid-like environment.[102] The peak assignments of vibrational modes of the alkyl chain in DDAO molecules are given in Table 4.1. In the C-H stretching region of DDAO vibrational bands from the methylene stretches are strongest due to the higher number of methylene groups in comparison to the number of methyl groups. The symmetric (d^+) and asymmetric (d^-) methylene stretching modes are at 2852

cm^{-1} and 2890 cm^{-1}, respectively. The peak caused by Fermi resonance (d^{+}_{FR}) between the (d^{+}) band and an overtone of the methylene bending mode occurs at around 2928 cm^{-1}. The terminal methyl group shows a peak of its asymmetric stretching mode (r^{-}) at about 2960 cm^{-1}. The symmetric stretching mode of the terminal methyl group (r^{+}) is obscured by the d^{-} band. A peak caused by the asymmetric stretch of the methyl headgroup (r^{-}_{HG}) is centered at 3038 cm^{-1} and is clear with all polarization combinations. Another contribution by the terminal methyl group to the Raman spectra is also recognized from its deformational overtone mode around 2725 cm^{-1}.[62]

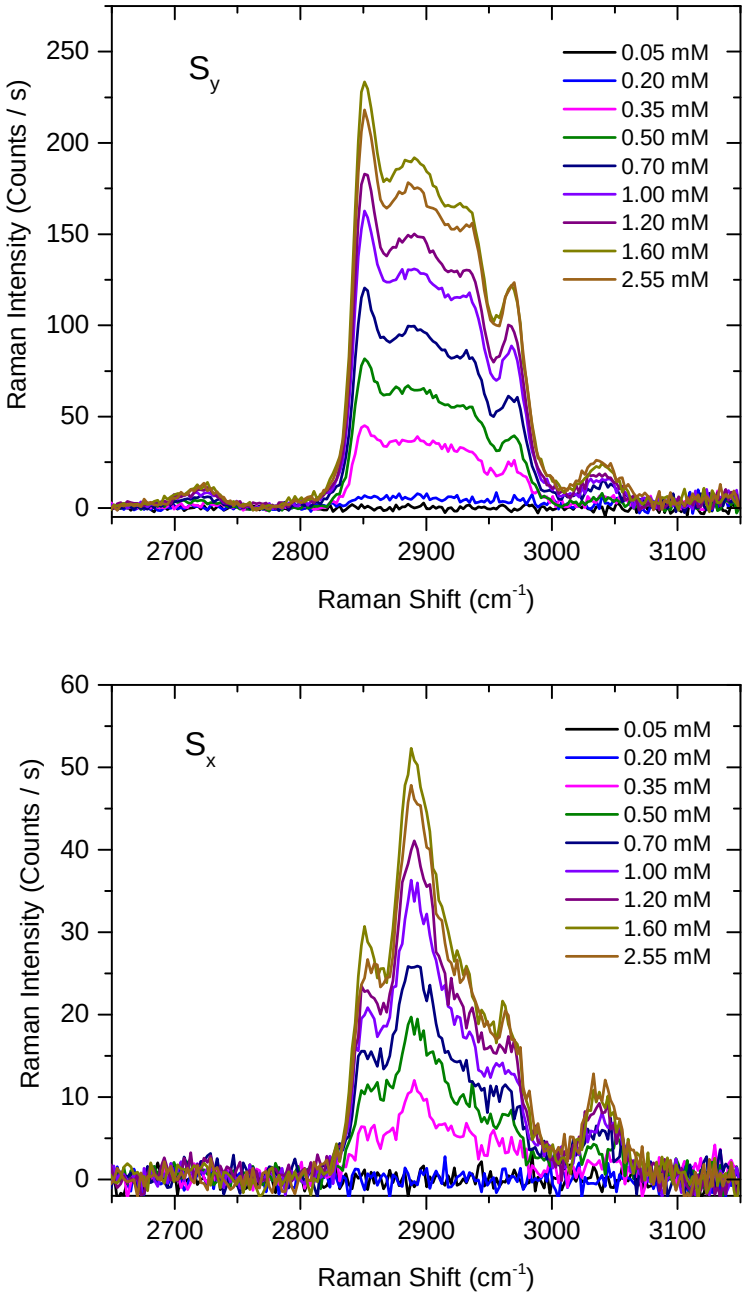

Figure 4.1. Background subtracted and baseline corrected TIR Raman spectra of DDAO at the silica/water interface with various DDAO bulk concentrations. Spectra were collected under S_x and S_y polarization combinations.

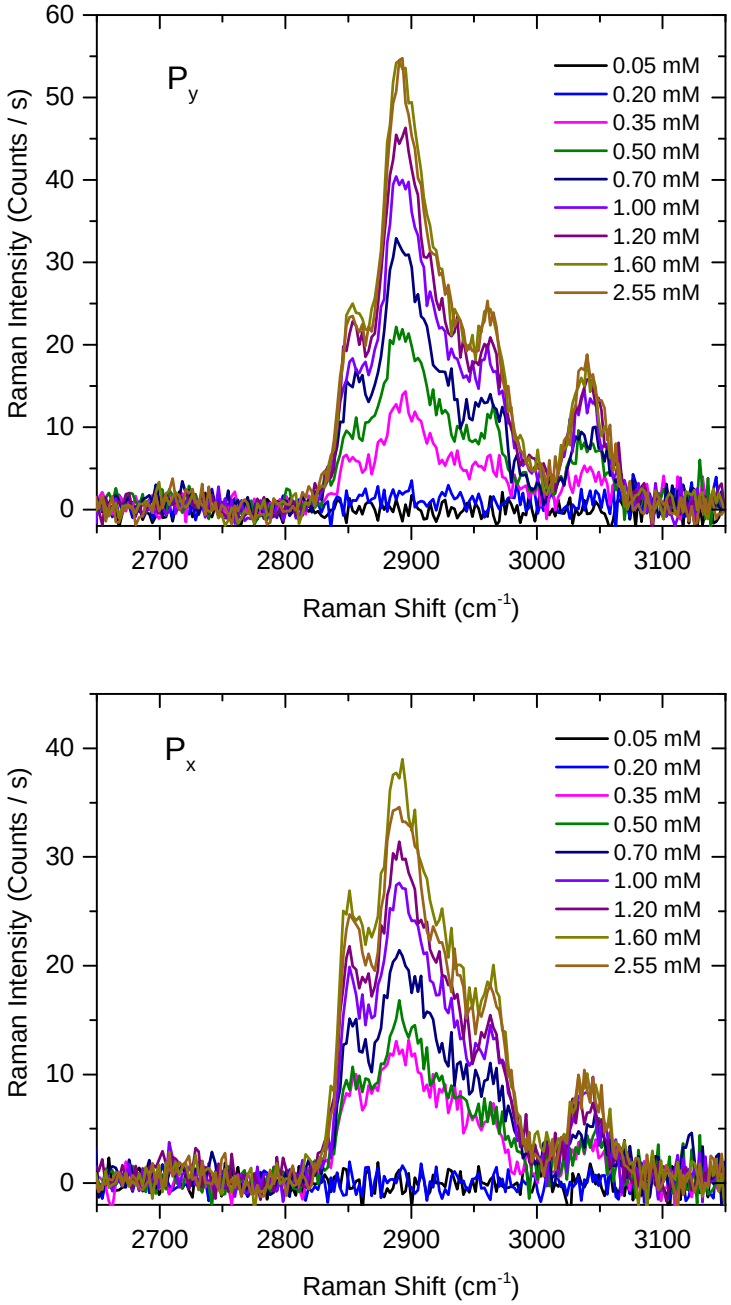

Figure 4.2. Background subtracted and baseline corrected TIR Raman spectra of DDAO at the silica/water interface with various DDAO bulk concentrations. Spectra were collected under P_x and P_y polarization combinations.

Due to the strong coupling between the (d^+) band and overtones of the CH_2 bending modes and the overlap of assigned and unassigned bands on the spectrum it is difficult to have a good peak-fitting analysis of S_y spectrum as

Table 4.1. Peak assignments of DDAO Raman spectra[62;100;101]

Frequency, cm^{-1}	Vibrational mode
2725	HCH overtone of terminal methyl group
2852	Symmetric methylene stretch (d^+)
2890	Asymmetric methylene stretch (d^-)
2928	Fermi resonance (d^+_{FR})
2960	Asymmetric methyl stretch (r^-)
3038	Asymmetric methyl headgroup (r^-_{HG})

required. The spectra obtained under S_x and P_x polarization combinations were used for the fitting and gave better results than those from the fitting of S_y-polarized spectra. Only the spectra obtained at low bulk concentrations were treated with TFA. These spectra have better signal-to-noise ratio after being treated with TFA, however, their spectral features might not represent the exact spectra of DDAO molecules at low bulk concentrations. The fitting results are given in Tables 4.2 and 4.3. Figure 4.3 shows a S_x-polarized DDAO Raman spectrum at 1.81 mM bulk concentration fitted to Gaussian functions.

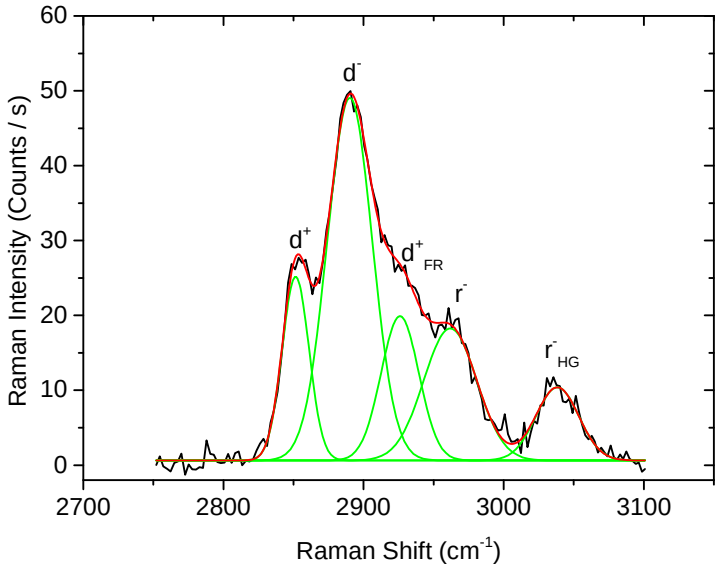

Figure 4.3. S_x-polarized Raman spectrum of DDAO at 1.81 mM bulk concentration fitted to Gaussian functions.

The fitting results in Tables 4.2 show that the peak centers of vibra-

tional modes are several wavenumbers different when bulk concentrations change. These small differences do not necessarily indicate a change of conformational order. They might result from the difference in signal-to-noise ratio between different spectra. Another indication of a possible conformational change is the relative peak height between two vibrational modes on the same spectra collected under the same polarization combination,[100] and these values were also obtained from the fitting of S_x-polarized Raman spectra and are shown in Figure 4.4. The relative intensity is quite constant with an average and standard deviation values of 1.89 and ± 0.11, respectively. The variation of these values can be considered to be within experimental errors. Effective Raman tensor elements are sensitive to the orientation of surfactant molecules at the interface and any change in the tilt angle of surface molecules will lead to a change of relative intensity of a vibrational mode in S- and P-polarized spectra. In the current study the intensity of the asymmetric methylene stretching mode (d^-) has the highest signal in the S_x and P_x spectra and is used to calculate the relative intensity of (d^-) mode (Figure 4.5). The results show that the relative intensity values are similar except for the one obtained from the experiment with 0.35 mM DDAO concentration. It was reported for the case of CTAB at a silica/water interface that a change of 2-4 degrees could be detected when the relative intensity changed by a factor of more than 2.[62] The maximum change in the current study was less than 1.7.

Table 4.2. Vibrational modes from fitting S_x-polarized Raman spectra of DDAO at the silica/water interface

Conc. (mM)	d^+ (cm^{-1})	d^- (cm^{-1})	d^+_{FR} (cm^{-1})	r^- (cm^{-1})	r^+_{HG} (cm^{-1})
0.35	2851.8 ± 0.3	2889.8 ± 0.8	2926.0 ± 1.2	2963.4 ± 1.8	3038.3 ± 0.5
0.50	2851.8 ± 0.3	2889.8 ± 0.8	2926.0 ± 1.2	2963.4 ± 1.8	3038.3 ± 0.5
0.70	2850.7 ± 0.9	2890.8 ± 1.0	$2927. \pm 2.4$	2960.5 ± 3.7	3035.8 ± 1.5
1.00	2851.0 ± 0.6	2891.1 ± 1.0	2926.8 ± 1.9	2960.7 ± 2.8	3039.4 ± 1.0
1.20	2851.6 ± 0.6	2890.3 ± 1.2	2929.3 ± 2.0	2965.0 ± 3.1	3037.2 ± 0.9
1.39	2852.0 ± 0.6	2890.2 ± 1.4	2925.8 ± 2.4	2964.2 ± 3.0	3038.6 ± 0.7
1.60	2851.5 ± 0.4	2888.5 ± 1.7	2924.0 ± 2.8	2963.8 ± 3.0	3039.1 ± 0.8
1.81	2851.5 ± 0.5	2890.2 ± 0.9	2925.9 ± 1.7	2961.9 ± 2.7	3038.3 ± 0.8
2.05	2852.4 ± 0.6	2887.4 ± 1.7	2920.9 ± 4.0	2965.7 ± 4.7	3038.3 ± 0.8
2.55	2852.5 ± 0.6	2890.2 ± 1.2	2927.7 ± 1.9	2965.0 ± 3.3	3038.5 ± 0.8

Table 4.3. Full width at half maximum (FWHM) of vibrational modes from fitting S_x-polarized Raman spectra of DDAO at the silica/water interface

Conc. (mM)	d^+ (cm^{-1})	d^- (cm^{-1})	d^+_{FR} (cm^{-1})	r^- (cm^{-1})	r^+_{HG} (cm^{-1})
0.35	23.01	36.90	34.82	39.99	36.60
0.50	23.01	36.89	34.84	39.98	36.60
0.70	23.38	41.50	27.93	42.11	39.94
1.00	22.24	41.96	28.71	44.24	38.07
1.20	22.78	38.28	35.85	34.37	33.66
1.39	24.16	36.22	35.64	39.52	33.45
1.60	22.08	34.97	39.15	36.49	33.67
1.81	22.74	37.75	31.77	44.74	36.65
2.05	23.91	32.32	45.11	40.86	39.53
2.55	23.76	36.71	35.75	38.43	39.27

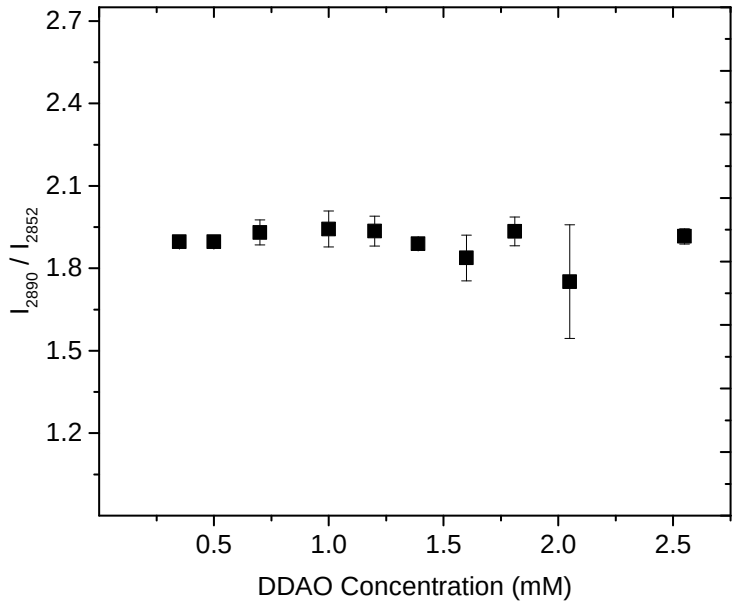

Figure 4.4. Relative peak heights of asymmetric (d^-) and symmetric (d^+) methylene stretches obtained from S_x-polarized Raman spectra and plotted as a function of DDAO concentration.

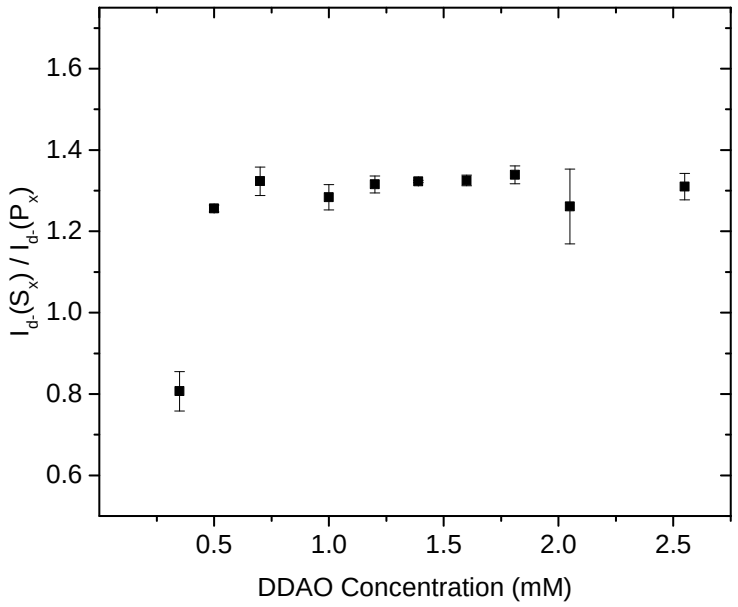

Figure 4.5. Relative intensities of the d^- band in the S_x- and P_x-polarized spectra.

4.1.2 Adsorption isotherm

The relative intensities between the d^- bands in the S_x and P_x spectra indicate almost constant average tilt angle of the alkyl chains in DDAO molecules. Under this condition the integrated areas of Raman spectra are considered to be proportional to the surface coverage. The C-H stretching region from 2800-3000 cm^{-1} on the S_y spectra was integrated and results with error bars are shown in Figure 4.6. The error bars on some points in Figure 4.6 are too close to the centers of the symbols. In region I with DDAO concentration below 0.20 mM, the adsorbed amount was insignificant or inefficiently detected by TIR Raman spectroscopy. The adsorption isotherm increases linearly with bulk concentration up to 1.60 mM in region II. After reaching a maximum value at a bulk concentration of about 1.60 mM, however, the isotherm decreases with bulk concentration in the region III. The critical micelle concentration (cmc) of DDAO solutions in the study is about 1.80 mM and is in the range reported in the literature (1.80-2.50 mM).[2;12;13;103] Claesson et al. studied the adsorption of DDAO at the silica/water interface and found that the DDAO adsorption isotherm was at a maximum value before the cmc and decreased when the bulk concentration was further increased.[2] The same trend is also observed in this study (Figure 4.6) but a decrease of adsorbed amount of DDAO is not obvious as in the study by Clasesson due to the increased bulk contribution to the total Raman signal when DDAO bulk concentration increases. The decrease of the adsorption isotherm would result from a change in the structure of the adsorbed layer. Bilayer-like structures were proposed to form on the silica surface in contact with DDAO solutions with concentrations close to the cmc.[2] A phase transition from a bilayer to admicelles, for example, will change the density of the adsorbed layer.

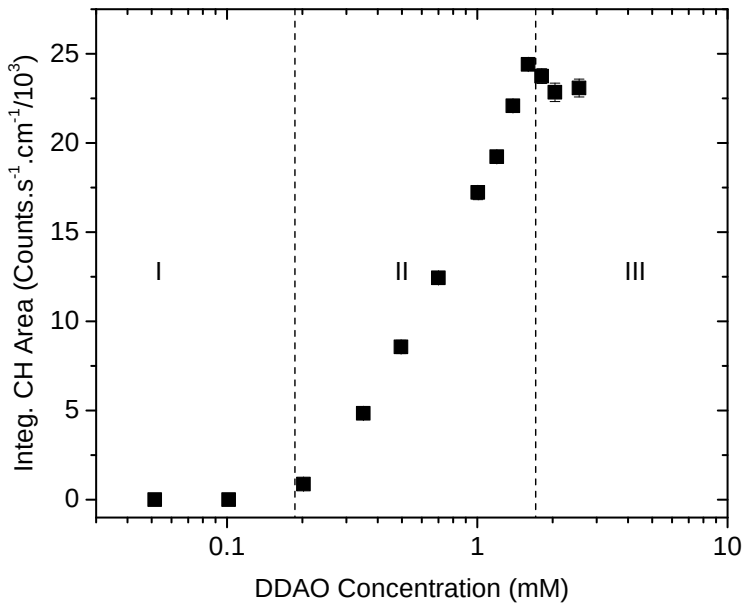

Figure 4.6. Adsorption isotherm of DDAO at the silica/water interface obtained from integrated areas of the C-H stretching region (2800-3000 cm^{-1}) of DDAO spectra collected under S_y polarization combination.

4.1.3 Adsorption mechanism

Dimethyldodecylamine oxide (DDAO) exists as both cationic and nonionic forms in aqueous solutions. For pure DDAO solutions, the degree of ionization is decreased from 11% to 0.8% when the DDAO concentration changes from low to high (cmc) and corresponds to an increase of solution from 5.8 to 7.0.[2] The dissociation (Equation 4.1) of the protonated form $DDAOH^+$ has a pK_a value of 4.7.[2] Silica surface in contact with water has been reported to have two different sites of silanol groups with corresponding pK_a values of 4.5 and 8.5.[48] The surface silanol groups are in equilibria with siloxides according to Equation 4.2. From the study by Eisenthal, the silanol sites with pK_a values of 4.5 and 8.5 occupy 19% and 81% of the total number of surface silanol groups, respectively. A point of zero charge for the silica surface is obtained when pH < 3.[48] For the range of native pH caused by DDAO solutions the silica surface is negatively

charged with the existence of both silanol and siloxide groups. The silanol groups have been reported to deprotonate only 19% at pH = 12 leading to a high density of silanols present at high pH values.[49] The deprotonation value was calculated with a density value of 4.5 silanols/nm^2. It has been proposed that, at low bulk surfactant concentrations, the adsorption of DDAO at the hydrophilic solid/liquid interface is caused by only electrostatic interactions between the cationic form and the negatively charged surface or by both the electrostatic interactions and hydrogen bonding between protonated DDAOH$^+$ and nonionic DDAO with the silica surface, respectively.[2;12] The N-O bond in the nonionic molecules is highly polar and was reported to form stronger hydrogen bonds with water than that between water molecules. Due to the strong hydrogen bonds of N-O groups it may be possible that, at low solution concentrations, the nonionic DDAO molecule forms hydrogen bonds with the silanol group and replaces water at the interface. The protonation of non-ionic DDAO molecules may be enhanced at the interface when they are close to the silanol groups of pK_a 4.5 and this finally leads to adsorption caused by electrostatic interactions. At higher bulk concentrations, all negatively charged sites on the silica surface are neutralized by protonated DDAOH$^+$ and further adsorption is driven by hydrogen bonding, hydrophobic effects, and lateral interactions (van der Waals interactions) between the hydrocarbon tails of pre-adsorbed molecules and that of surfactant molecules in the bulk solution.

$$\mathrm{DDAOH^+ + H_2O \rightleftharpoons DDAO + H_3O^+} \tag{4.1}$$

$$\mathrm{- SiOH + H_2O \rightleftharpoons -SiO^- \ + H_3O^+} \tag{4.2}$$

4.2 Adsorption of DDAO with added NaCl

4.2.1 DDAO Spectra

Spectra of DDAO at the silica/liquid interface at various DDAO concentrations and 0.20 M NaCl are shown in Figures 4.7 and 4.8. These spectra were measured with different polarization combinations and DDAO bulk surfactant concentration ranged from 0.05 mM to 2.51 mM. The detection limit is about 6 counts/s. The peak assignments are in the previous section and they are shown here in Table 4.4. The hydrocarbon chains of DDAO molecules are in liquid-like environment as revealed by the peak positions and relative intensities of different vibrational modes on the Raman spectra.[102] Sodium chloride at 0.20 M shows no recognized effects on the conformation of alkyl chains of DDAO.

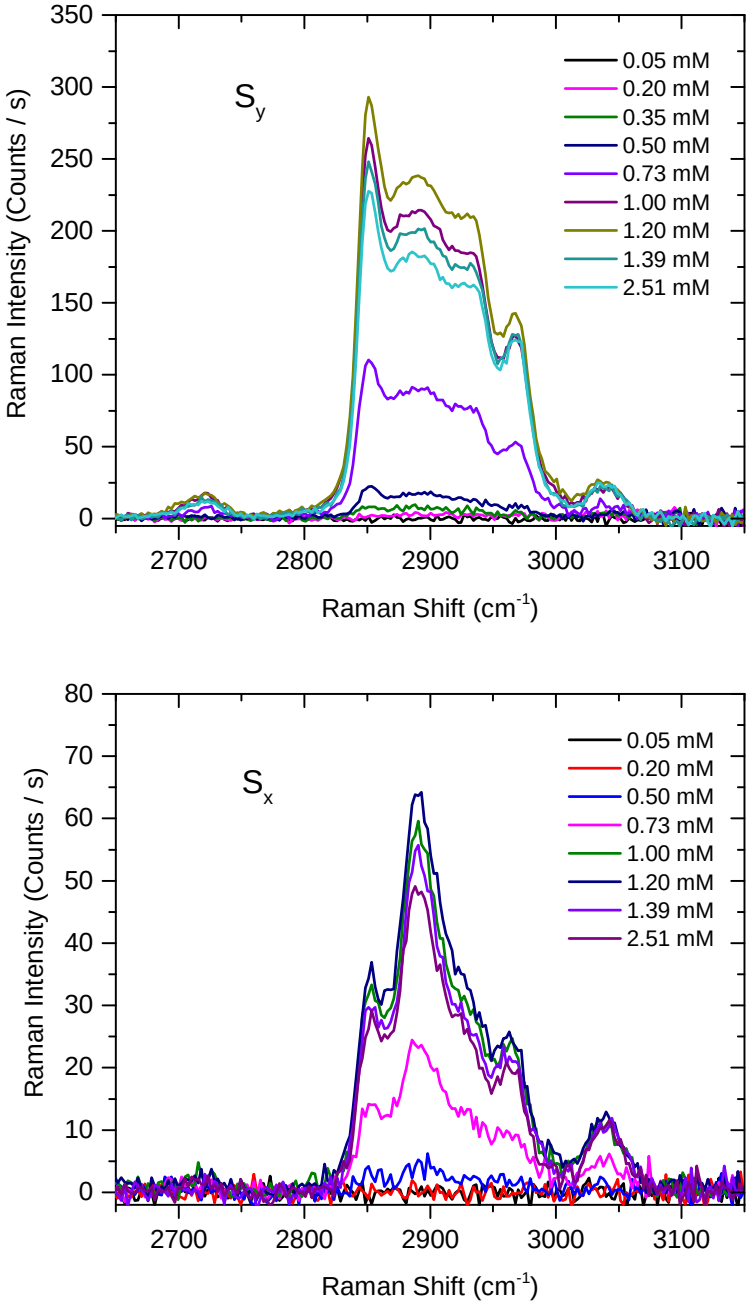

Figure 4.7. Background subtracted and baseline corrected TIR Raman spectra of DDAO at the silica/water interface with various DDAO bulk concentrations. Spectra were collected under S_x and S_y polarization combinations. The solution concentration of NaCl was 0.20 M.

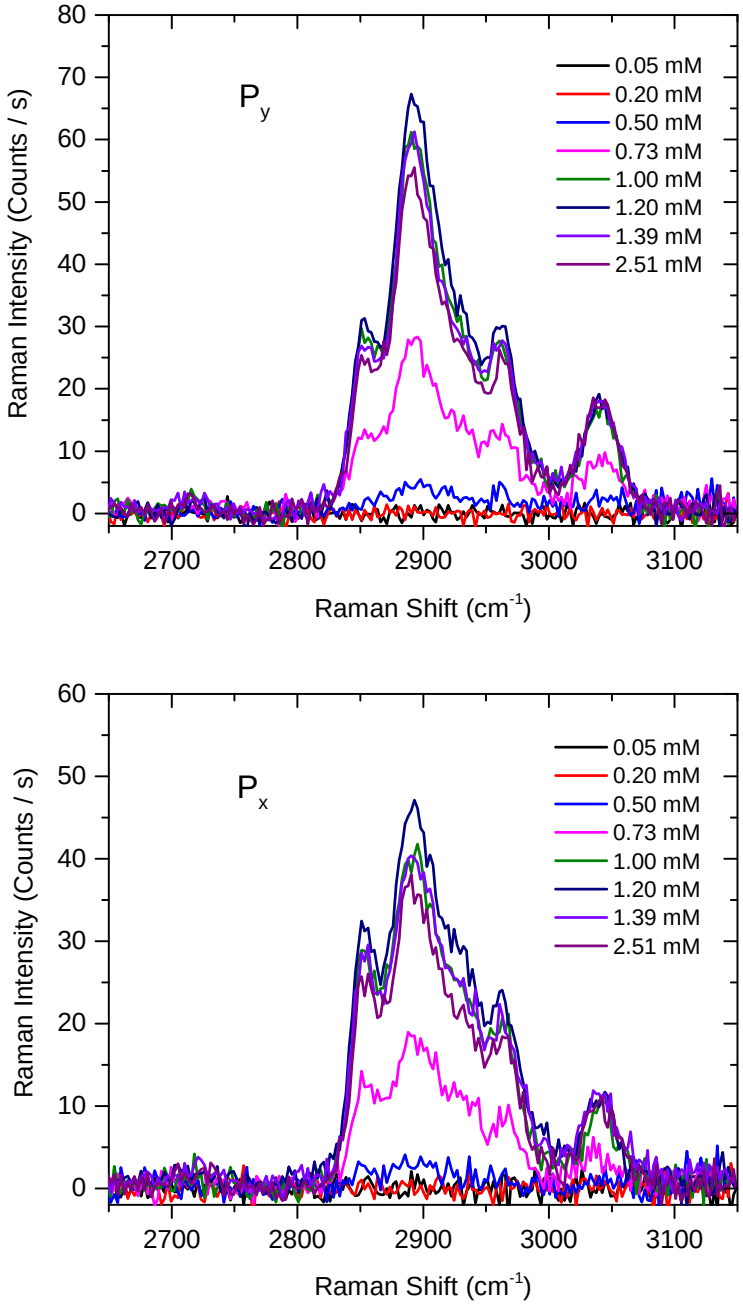

Figure 4.8. Background subtracted and baseline corrected TIR Raman spectra of DDAO at the silica/water interface with various DDAO bulk concentrations. Spectra were collected under P_x and P_y polarization combinations. The solution concentration of NaCl was 0.20 M.

The spectra obtained from S_x- and P_x-polarized measurements were fitted to analyze the conformational and orientational changes of DDAO molecules.

The fitting results are given in Tables 4.5 and 4.6. Figure 4.9 shows an S_x-polarized Raman spectrum of DDAO fitted to Gaussian functions. The relative intensity of the d^- and d^+ modes were calculated and the results indicate an insignificant change in the conformation of the hydrocarbon chains in DDAO molecules (Figure 4.10). The relative intensity between the d^- mode in S_x-polarized spectrum and that in P_x-polarized spectrum showed a quite constant of the averaged tilt angle of the alkyl chains with respect to the surface normal.

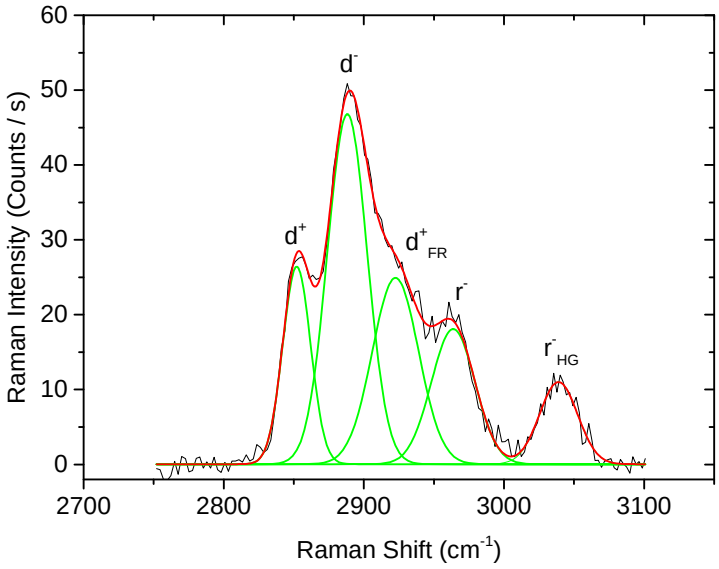

Figure 4.9. S_x-polarized Raman spectra of DDAO at the silica/water interface fitted to Gaussion functions. DDAO solution concentration was 1.80 mM.

Table 4.4. Peak assignments of DDAO Raman spectra[62;100;101]

Frequency, cm^{-1}	Vibrational mode
2725	HCH overtone of terminal methyl group
2852	Symmetric methylene stretch (d^+)
2890	Asymmetric methylene stretch (d^-)
2928	Fermi resonance (d^+_{FR})
2960	Asymmetric methyl stretch (r^-)
3038	Asymmetric methyl headgroup (r^-_{HG})

Table 4.5. Vibrational modes from fitting S_x-polarized Raman spectra of DDAO at the silica/water interface

Conc. (mM)	d^+ (cm^{-1})	d^- (cm^{-1})	d^+_{FR} (cm^{-1})	r^- (cm^{-1})	r^+_{HG} (cm^{-1})
0.50	2851.9 ± 0.3	2889.4 ± 0.7	2924.5 ± 1.2	2963.3 ± 1.4	3038.6 ± 0.4
0.73	2851.4 ± 0.8	2891.1 ± 1.1	2927.2 ± 2.6	2960.5 ± 4.7	3038.2 ± 1.7
1.00	2851.6 ± 0.4	2890.2 ± 0.8	2928.0 ± 1.3	2964.8 ± 1.7	3036.6 ± 0.8
1.10	2851.7 ± 0.4	2889.6 ± 1.3	2923.2 ± 2.2	2960.9 ± 3.0	3039.2 ± 0.8
1.20	2851.9 ± 0.5	2889.7 ± 1.1	2924.0 ± 1.9	2962.6 ± 2.4	3037.5 ± 0.8
1.30	2851.8 ± 0.4	2888.0 ± 1.7	2921.3 ± 3.1	2963.1 ± 3.6	3039.0 ± 0.8
1.39	2852.2 ± 0.4	2890.4 ± 0.7	2925.4 ± 1.3	2962.4 ± 1.7	3040.1 ± 0.7
1.60	2852.2 ± 0.4	2888.5 ± 1.5	2923.7 ± 3.8	2966.4 ± 2.3	3038.4 ± 0.6
1.80	2852.1 ± 0.5	2888.2 ± 1.5	2922.6 ± 2.7	2963.7 ± 2.4	3039.0 ± 0.6
2.00	2851.2 ± 0.4	2890.2 ± 1.1	2928.7 ± 0.0	2965.5 ± 2.9	3038.7 ± 0.7
2.51	2852.2 ± 0.5	2889.7 ± 0.9	2926.0 ± 1.5	2964.1 ± 1.5	3039.1 ± 0.7

Table 4.6. Full width at half maximum (FWHM) of vibrational modes from fitting S_x-polarized Raman spectra of DDAO at the silica/water interface

Conc. (mM)	d^+ (cm^{-1})	d^- (cm^{-1})	d^+_{FR} (cm^{-1})	r^- (cm^{-1})	r^+_{HG} (cm^{-1})
0.50	23.03	35.51	35.49	39.47	37.24
0.73	22.24	40.23	28.20	46.68	40.84
1.00	22.20	37.48	33.69	35.37	40.16
1.10	22.81	36.19	34.20	46.19	40.60
1.20	24.26	35.42	34.46	42.29	37.76
1.30	22.30	33.69	40.17	41.93	38.79
1.39	23.50	35.83	31.37	41.00	36.70
1.60	23.21	33.91	45.17	33.55	37.61
1.80	23.44	33.45	38.70	36.92	32.16
2.00	21.76	39.58	36.70	35.36	36.00
2.51	23.54	35.76	33.70	34.28	36.37

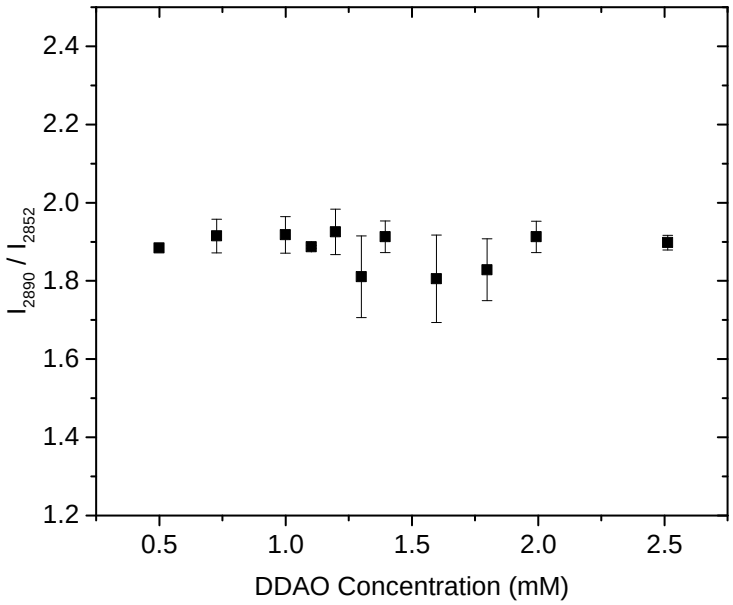

Figure 4.10. Relative peak heights of asymmetric (d^-) and symmetric (d^+) methylene stretches obtained from S_x-polarized Raman spectra and plotted as a function of DDAO concentration.

4.2.2 Adsorption isotherm

Figure 4.12 shows the adsorption isotherm of DDAO with 0.20 M NaCl in the bulk plotted as a function of solution concentrations. The isotherm here is presented in terms of the integrated area of the C-H stretching region (2800-3000 cm^{-1}). The results obtained in the previous study are also presented in Figure 4.12 for comparison. It is from these isotherms that the adsorbed amount of DDAO when 0.20 M NaCl is added is significant at higher concentration in comparison to that of DDAO without added 0.20 M NaCl. In the case of DDAO solutions without NaCl, DDAO molecules need to compete with the interfacial water to adsorb to the silica surface. The addition of an electrolyte would reduce the concentration of free water in the solution as well as at the interface, however, the Na^+ ions are present in the interfacial region and compete with the DDAO molecules for the negative charged sites on the surface. The added

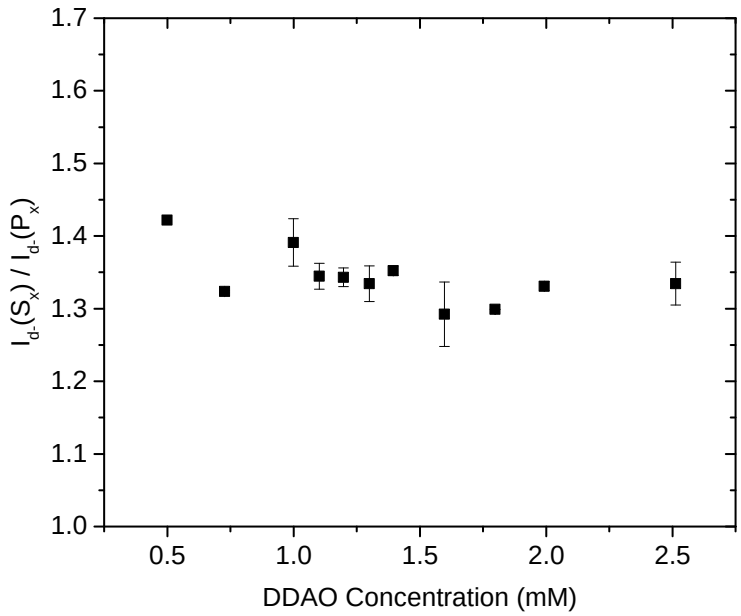

Figure 4.11. Relative intensities of the d^- band in the S_x- and P_x-polarized spectra as a function of DDAO concentration.

NaCl in the current study is also expected to cause the salting-out effect on the hydrocarbon chains of DDAO and enhance the adsorption of the surfactant.[104] At the DDAO concentrations smaller than 0.70 mM the competition of DDAO with the interfical sodium ions and the interaction of cationic DDAO and the chloride ions determine the adsorbed amount of DDAO at the interface. When the DDAO concentration is higher, the salting-out and hydrophobic effects are dominant. The DDAO molecules bind to the silica surface via electrostatic interactions and hydrogen bonds and the adsorption is enhanced by the salting-out effect. The silica surface in contact with solutions of alkali halides have been studied both experimentally and theoretically and the more acidic silanols were reported to have lower pK_a values in comparison to ones in pure water.[52;54–59] A lower pK_a might lead to a higher density of negative charged sites on the silica surface and enhance the protonation of DDAO molecules at the interface.

Sodium chloride was reported to lower the cmc of DDAO solution and

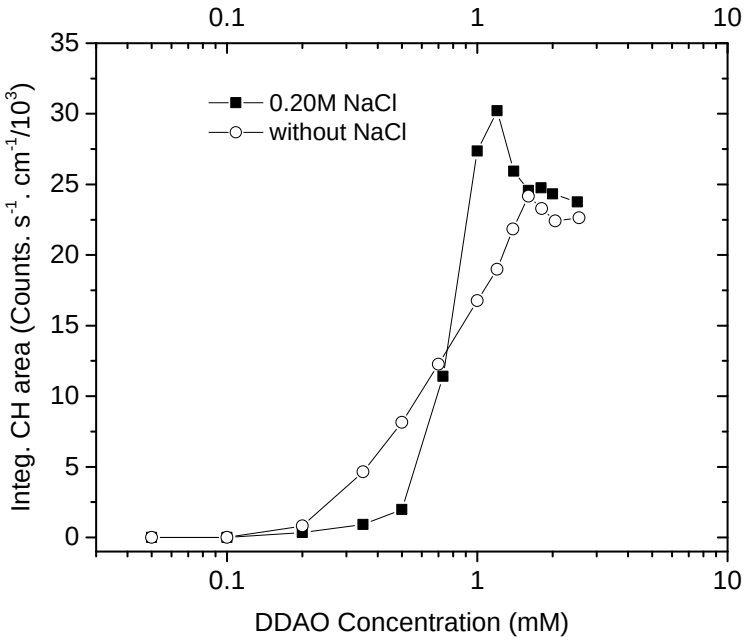

Figure 4.12. Adsorption isotherms of DDAO at the silica/water interface with and without 0.20 M NaCl in the aqueous solutions.

increase the molar micellar weight.[103;104] The form of DDAO in these studies, however, was controlled by adjusting the solution pH so that only cationic or nonionic form exist in the aqueous phase. The control of solution pH in the study of surfactant adsorption at the silica/water interface, especially in the case of a pH sensitive surfactant like DDAO, will make the interpretation of the results more complicated. It is due to the fact that the charge of the silica surface will also be modified by the change of solution pH.

The adsorption isotherms of DDAO show a common intersection point (cip) at the solution concentration of about 0.70 mM. This intersection point is the surfactant concentration at which the surface excess is not effected by an electrolyte.[61;71;105] This point has been interpreted as the isoelectric point (iep) of the substrate when there is no adsorption of background electrolyte on the solid surface. The cip has been suggested as the point at which a bilayer of surfactants starts forming on the surface with the headgroups of the second layer facing to-

wards the solution.[71] The existence of cip indicates that the first layer of DDAO on the charged surface is composed of mainly protonated $DDAOH^+$. Vibrational sum frequency generation (VSFG) measurements with surfactant concentrations below and above the cip (0.70 mM in the current study) might validate the cip. The SFG signal of the terminal methyl group would decrease or vanish when a bilayer forms on the substrate.

4.3 Adsorption of TX-100

4.3.1 TX-100 spectra

The adsorption of TX-100 on the hydrophilic silica surface has also been investigated in the current study. Figure 4.13 shows a set of background subtracted and baseline corrected TIR Raman spectra of TX-100 at different TX-100 solution concentrations. The Raman spectra of TX-100 measured when 0.20 M NaCl was in the surfactant solutions are given in Figure 4.14. All TIR Raman experiments were performed without a polarizer in the setup and only S-polarized light was used. The removal of the polarizer helps increase the signal-to-noise ratio of the spectra. Raman spectra of pure TX-100 in the 2800-3000 cm^{-1} region are due to vibrational modes of the alkyl chains and that of ethylene oxide (EO) groups. The peak of symmetric CH stretch of the aromatic ring is observed at 3080 cm^{-1}.[40]

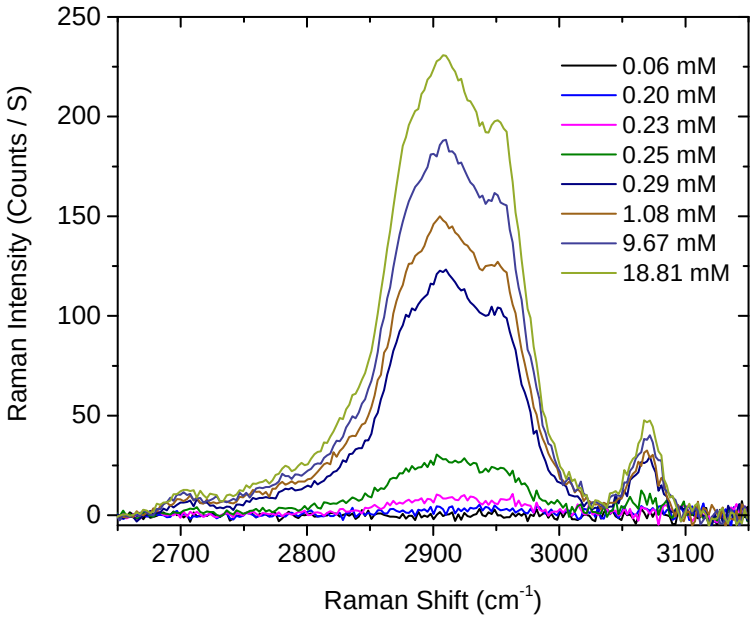

Figure 4.13. Background subtracted and baseline corrected TIR Raman spectra of TX-100 at the silica/water interface with various TX-100 bulk concentrations. Spectra were obtained from S-polarized measurements.

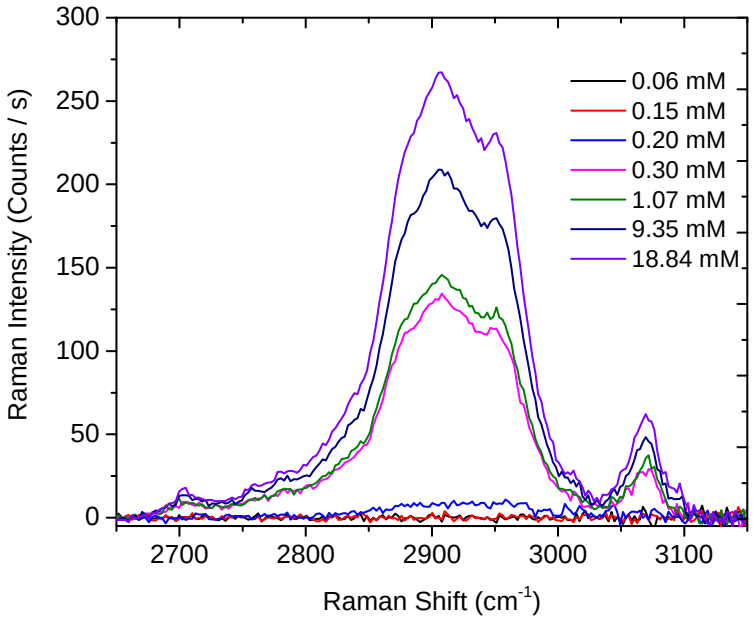

Figure 4.14. Background subtracted and baseline corrected TIR Raman spectra of TX-100 at the silica/water interface with various TX-100 bulk concentrations. Spectra were obtained from S-polarized measurements. NaCl concentration was 0.20 M.

4.3.2 Adsorption isotherm

TIR Raman spectra of TX-100 were analyzed by target factor analysis and the component weights are given in Figure 4.15. The bulk contributions to the Raman signal are obvious at high concentrations of TX-100. The component weights are calibrated to eliminate the bulk contribution and converted to surface excesses. The adsorption isotherms of TX-100 in terms of surface excesses at the silica/water interface are shown in Figure 4.16. They are presented as a function of log([TX-100]/mM). At TX-concentrations smaller than 0.20 mM, both adsorption isotherms are insignificant. In the concentration region of 0.20 - 0.30 mM, the adsorbed amount of TX-100 at the interface is much higher with 0.20 M NaCl in the aqueous solution. This might be caused by the presence of NaCl that makes the interaction between TX-100 molecules stronger. The stronger interactions would be reflected by a higher value of the interaction parameter ω. The salting-out effect of NaCl on the hydrocarbon chains of TX-100 might also contribute to this observation.

The adsorption isotherms in both cases show a step function due to the possible presence of both monomers and aggregates at the interface.[40] At TX-100 concentration higher than the cmc ($\approx$ 0.30 mM) , the addition of NaCl to the surfactant solution leads to a decrease in the adsorbed amount. The TX-100 micelles are dehydrated in the solution with NaCl leading to a smaller effective headgroup area of the monomer and an increase in micellar sizes.[106] The surfactant is then more in the bulk solution. The change of surface charge and the presence of NaCl might also alter the structure of the adsorbed layer.

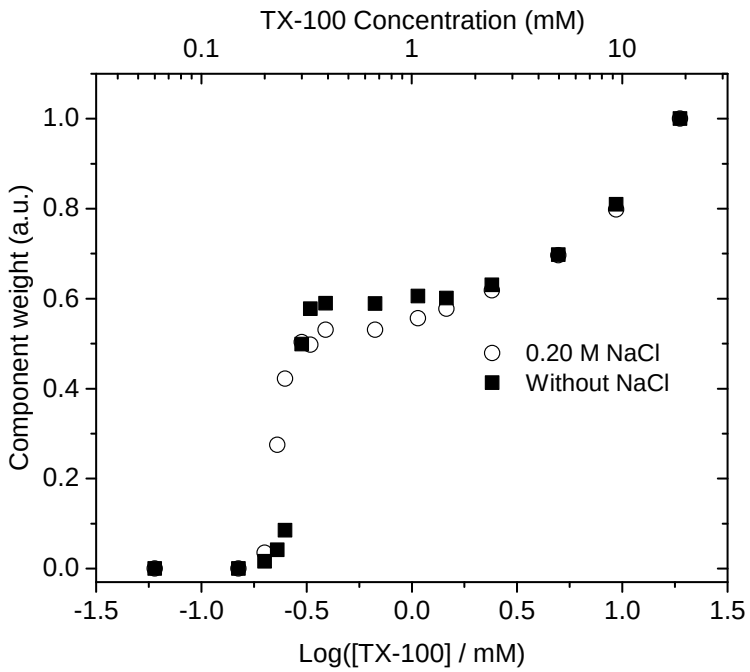

Figure 4.15. Component weights of TX-100 with and without 0.20 M NaCl in the aqueous solutions. These values are from target factor analysis of sets of TX-100 spectra.

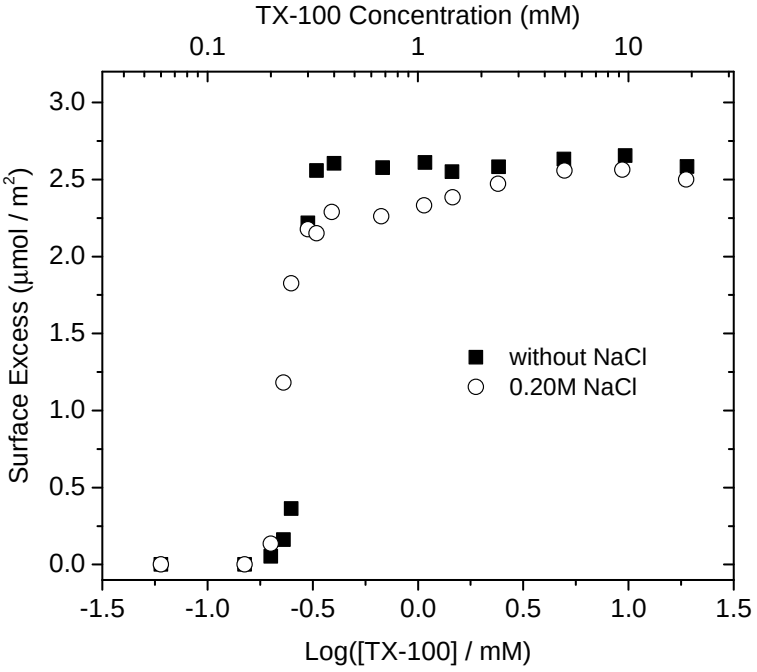

Figure 4.16. Adsorption isotherms of TX-100 at the silica/water interface with and without 0.20 M NaCl in the aqueous solutions.

The adsorption isotherms of TX-100 are fitted to the Frumkin model (Figure 4.17) and the fitting results are given in Table 4.7. The open circles were removed from the fitting as they do not follow the Frumkin model. ω values in Table 2.71 reveal strong interactions between TX-100 molecules on the silica surface.[40]

Table 4.7. Parameters obtained from fitting adsorption isotherms of TX-100 to the Frumkin model.

NaCl (M)	Γ_∞ (mol m^2)	K_L (mol^{-1} m^3)	ω
0	2.57	0.21	5.21
0.20	2.68	0.21	4.20

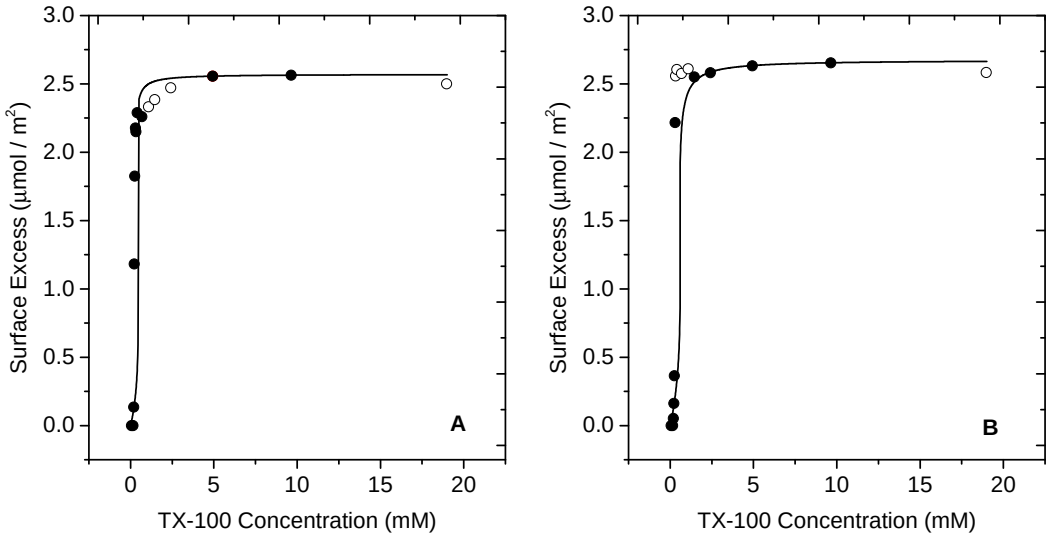

Figure 4.17. Adsorption isotherms of TX-100 at the silica/water interface: (A) with 0.20 M NaCl and (B) without 0.20 M NaCl in the bulk solution. The solid lines represent the isotherms fitted to the Frumkin model. The isotherm here is expressed in term of surface excess. The open circles were not used in the fittings.

Chapter 5

Adsorption of mixtures of DDAO and TX-100

5.1 Adsorption of mixtures without added salt

5.1.1 Adsorption of mixtures at low concentration of DDAO

Spectra of DDAO and TX-100 mixtures at the silica/water interface are shown in Figure 5.1. In all these mixtures, the bulk concentration of DDAO was constant at 0.30 mM ($\approx \frac{1}{6}$cmc) and TX-100 solution concentration was varied from 0.06 mM to 18.98 mM. Spectral assignments of pure DDAO and TX-100 are discussed the previous chapter. The spectral shape in Figure 5.1 is a mixed shape of DDAO and TX-100 spectra at TX-100 concentrations approximately below 2.50 mM and is close to that of pure TX-100 at higher concentrations. This might be an indication of cooperative adsorption at low TX-100 concentrations and competitive adsorption at higher ones.

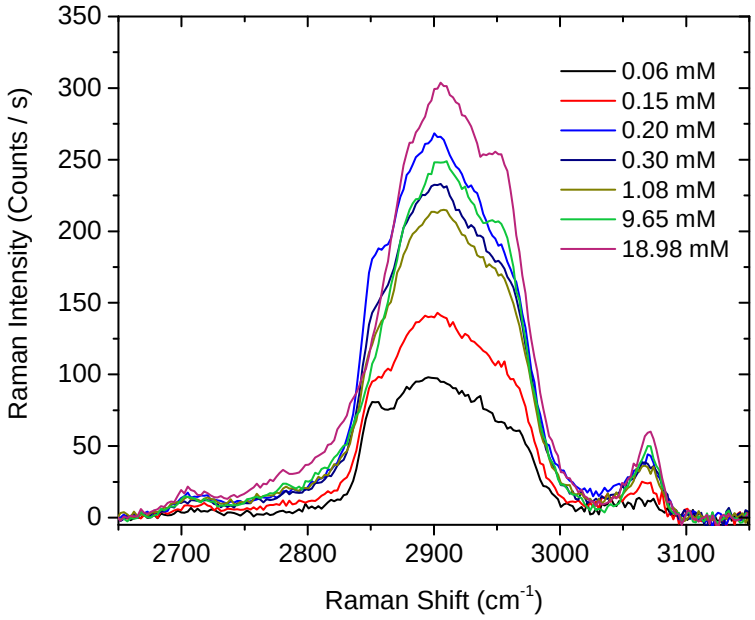

Figure 5.1. Background subtracted and baseline corrected TIR Raman spectra of DDAO and TX-100 mixtures at DDAO bulk concentration of 0.30 mM and varied concentrations of TX-100.

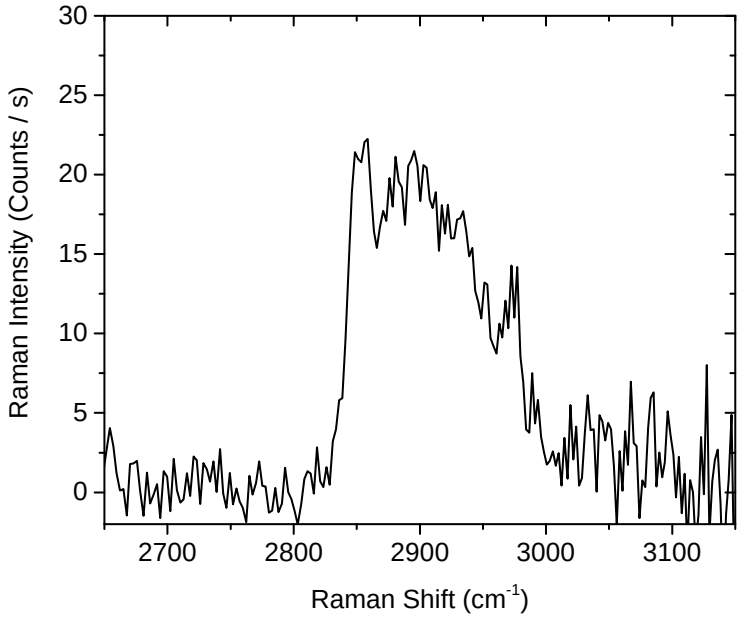

Figure 5.2. S-polarized Raman spectrum of DDAO at the silica/water interface with a bulk concentration of 0.30 mM.

Adsorption Isotherm. Target testing confirmed that two factors were responsible for the data with their corresponding SPOIL values smaller than 3 (Table 5.1). Targets 1 and 2 in Table 5.1 are DDAO and TX-100, respectively. Target spectra were obtained from S-polarized Raman measurements with single component solutions of 2.00 mM DDAO and 18.81 mM TX-100, respectively. The target and refined spectra of DDAO and TX-100 are given in Figure 5.3. These spectra show that, while target and refined spectra of TX-100 match very well, the ones of DDAO show noticeable differences. The orientation and conformation of molecules in the mixed surfactant layer might be different from that of a single surfactant layer. It is also the imperfection of chemometric methods in decomposing overlapped spectra. TFA was performed to decompose the mixed spectra into single components and then rotate abstract row and column matrices to obtain refined spectra and component weights of two surfactants in the mixtures. The component weights of two surfactants in the mixed spectra are given in Figure 5.4. The error bars are very close to the centers of the symbols and are hard to see. The CH stretching region (2800-3000 cm^{-1}) of extracted TX-100 and DDAO spectra as well as that of reproduced mixed spectra were integrated and plotted versus log([TX-100]/mM) in Figure 5.5.

Table 5.1. Results obtained from target testing of DDAO and TX-100 mixtures. DDAO concentration was of 0.30 mM and TX-100 concentration was varied.

Target	REP	RET	SPOIL
1	3.42	6.40	1.87
2	1.30	2.88	2.22

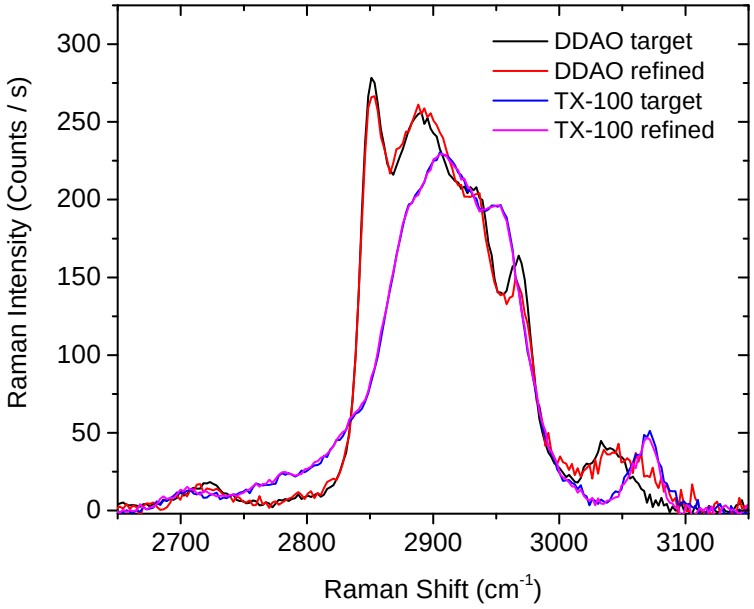

Figure 5.3. Target and refined spectra of DDAO and TX-100. The target spectra were obtained from S-polarized Raman experiments without a polarizer in the setup.

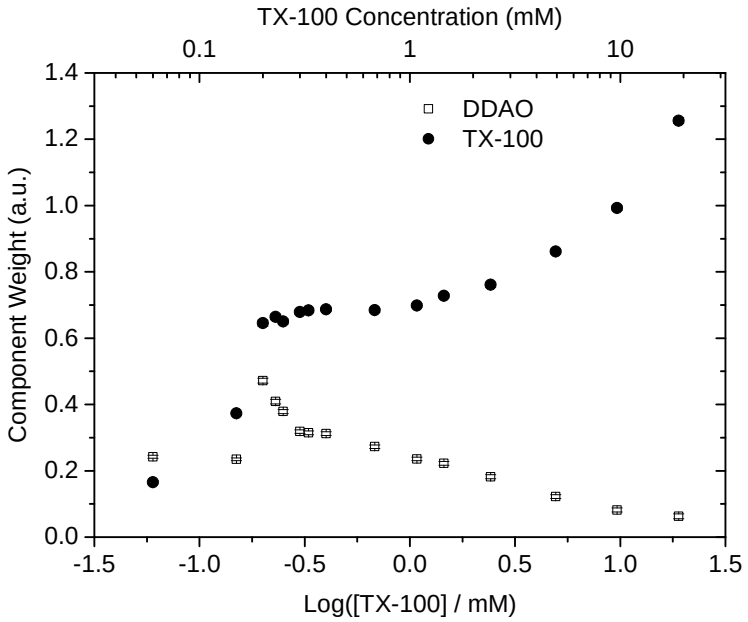

Figure 5.4. Component weights of TX-100 and DDAO in the mixtures as a function of log([TX-100]/mM). The bulk concentration of DDAO was 0.30 mM.

DDAO concentration was constant well below its cmc value so that bulk

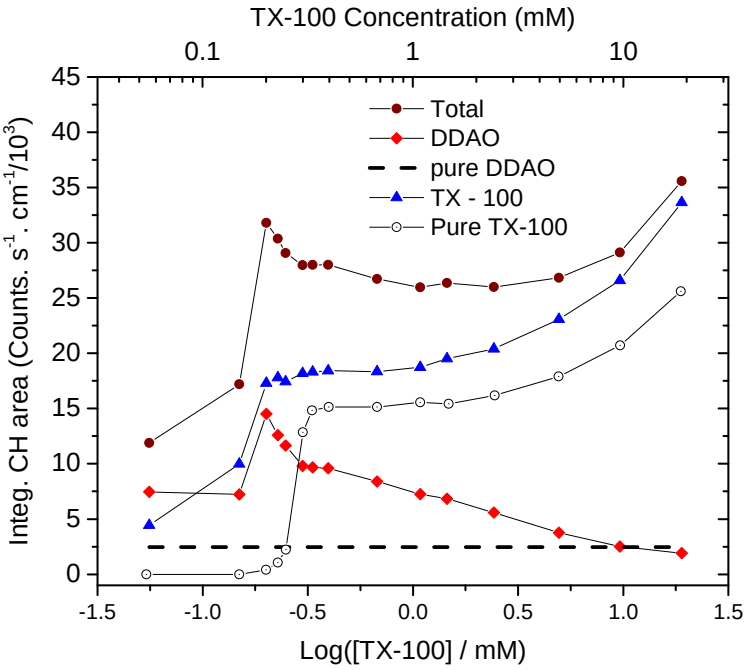

Figure 5.5. Integrated CH areas of TX-100, DDAO and mixed spectra plotted as a function of log([TX-100]/mM). The integrated CH region is from 2800 to 3000 cm^{-1}. The dashed line shows integrated values of pure DDAO at the silica/water interface with a bulk concentration of 0.30 mM.

contribution to its Raman spectra is negligible. For the purpose of comparison, integrated CH stretch area of DDAO at the silica/water interface with a bulk concentration of 0.30 mM is plotted in Figure 5.5. In this figure results from adsorption measurements with pure TX-100 at the same concentration as that in the mixture are also shown. The Raman signals of DDAO in Figure 5.5 indicate a strong synergistic effect at low bulk concentrations of TX-100 and competitive adsorption at very high concentrations.

Adsorption of both surfactants to the hydrophilic silica surface were enhanced in the mixtures (Figure 5.5). In the case of DDAO, except at very high concentration of TX-100, its Raman intensity is always higher than that of pure DDAO. The Raman intensity of DDAO first increases up to a maximum value at a TX-100 concentration of about 0.20 mM and then decreases with higher TX-100 bulk concentrations. The total Raman signal is also highest at a concen-

tration of 0.20 mM for TX-100. This is an indication of a change in the structure of the adsorbed layer leading to a more efficient coverage of the surface. A bilayer structure may be formed at the interface as suggested in the adsorption study of mixed surfactants of DDAO and dodecyl maltoside ($C_{12}G_2$).[2] When TX-100 bulk concentration increases, surface DDAO molecules are displaced by TX-100 and are incorporated into the mixed micelles in the solution leading to a decrease of its interfacial concentration.

The absolute values of component weights obtained from TFA have no physical meaning and need to be converted into the surface excess of surfactant molecules. The surface excesses of TX-100 in the mixtures were obtained by comparing its Raman intensities to that of a pure system measured at the same conditions. The surface excess of DDAO in the single component system (Figure 4.6) is not constant with concentration above the cmc. It is only possible to calibrate the component weights of TX-100 in single and mixed surfactant systems. The surface excesses obtained from the calibration procedure are shown in Figure 5.6. Adsorption of TX-100 at the interface is greatly enhanced in the mixed surfactants (Figure 5.6). While the surface excess of TX-100 is insignificant at small concentrations of a pure system, it is much higher when DDAO is incorporated into the solution. Although the surface concentration of DDAO decreases when TX-100 concentration increases, the small amount of DDAO at the interface keeps the TX-100 surface excess in the mixtures higher than that in the pure system. The decrease of both total and DDAO Raman signals after the maximum might indicate a structural change of the adsorbed layer.

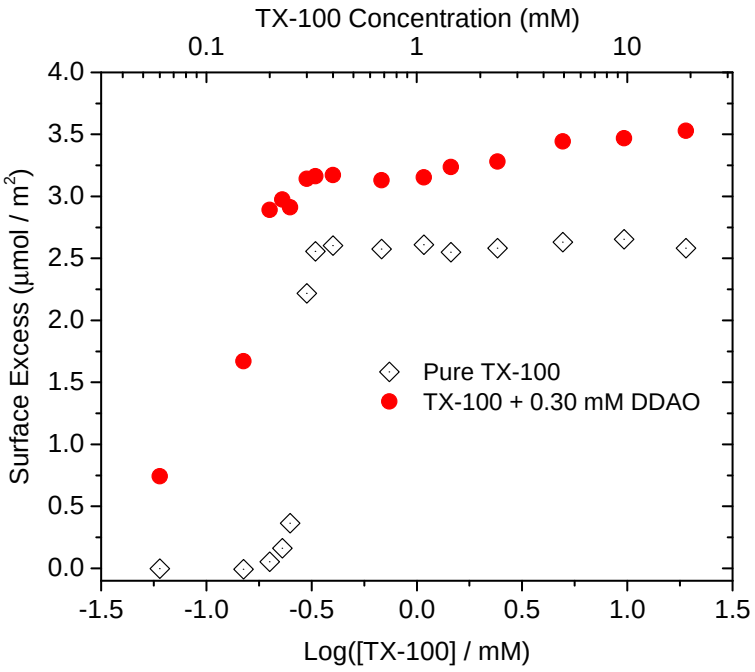

Figure 5.6. Adsorption isotherms of TX-100 in single and mixed systems as a function of log([TX-100]/mM). The isotherm here is expressed in terms of surface excess. TIR Raman experiments of the mixtures were performed with constant concentration of DDAO (0.30 mM) and varied concentration of TX-100.

Adsorption kinetics. Figures 5.7 - 5.9 show variations of the Raman signal with time for different mixtures of TX-100 and DDAO. The variations are shown for total Raman signal as well as signals of single components. The adsorption of the mixture at very low concentration of TX-100 (0.06 mM) is at equilibrium after about 55 minutes (Figure 5.7A). At higher concentrations of TX-100, it takes less than 5 minutes for the adsorption process to be at equilibrium.

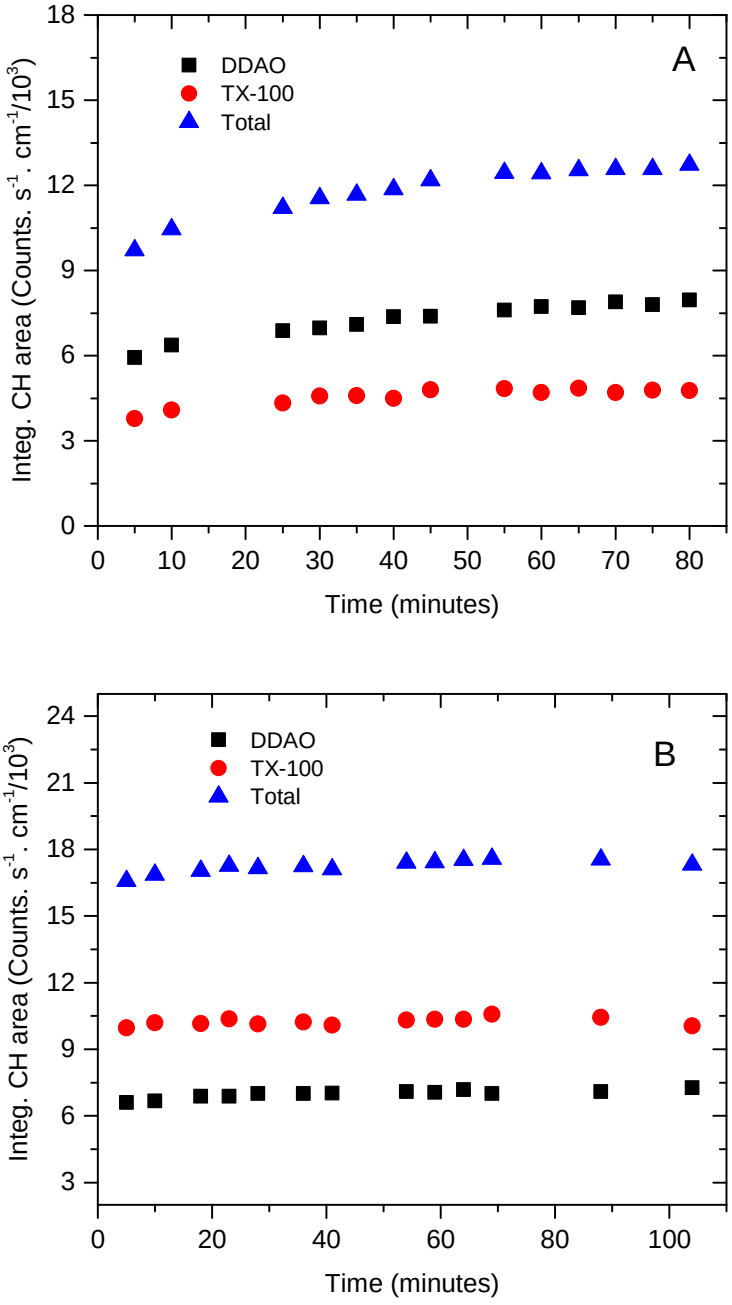

Figure 5.7. Adsorption kinetics of mixtures with two different bulk concentrations of TX-100: (A) 0.06 mM; (B) 0.15 mM. The bulk concentration of DDAO was fixed at 0.30 mM.

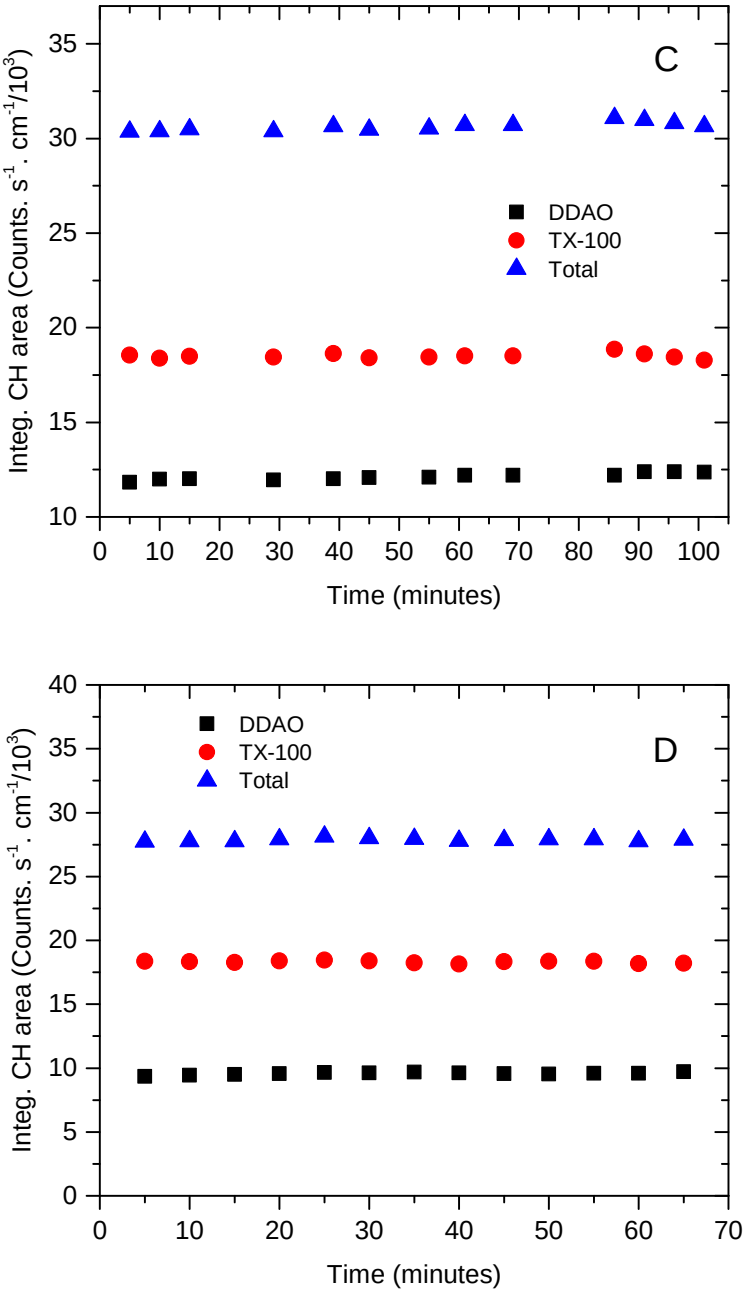

Figure 5.8. Adsorption kinetics of mixtures with two different bulk concentrations of TX-100: (C) 0.23 mM; (D) 0.30 mM. The bulk concentration of DDAO was fixed at 0.30 mM.

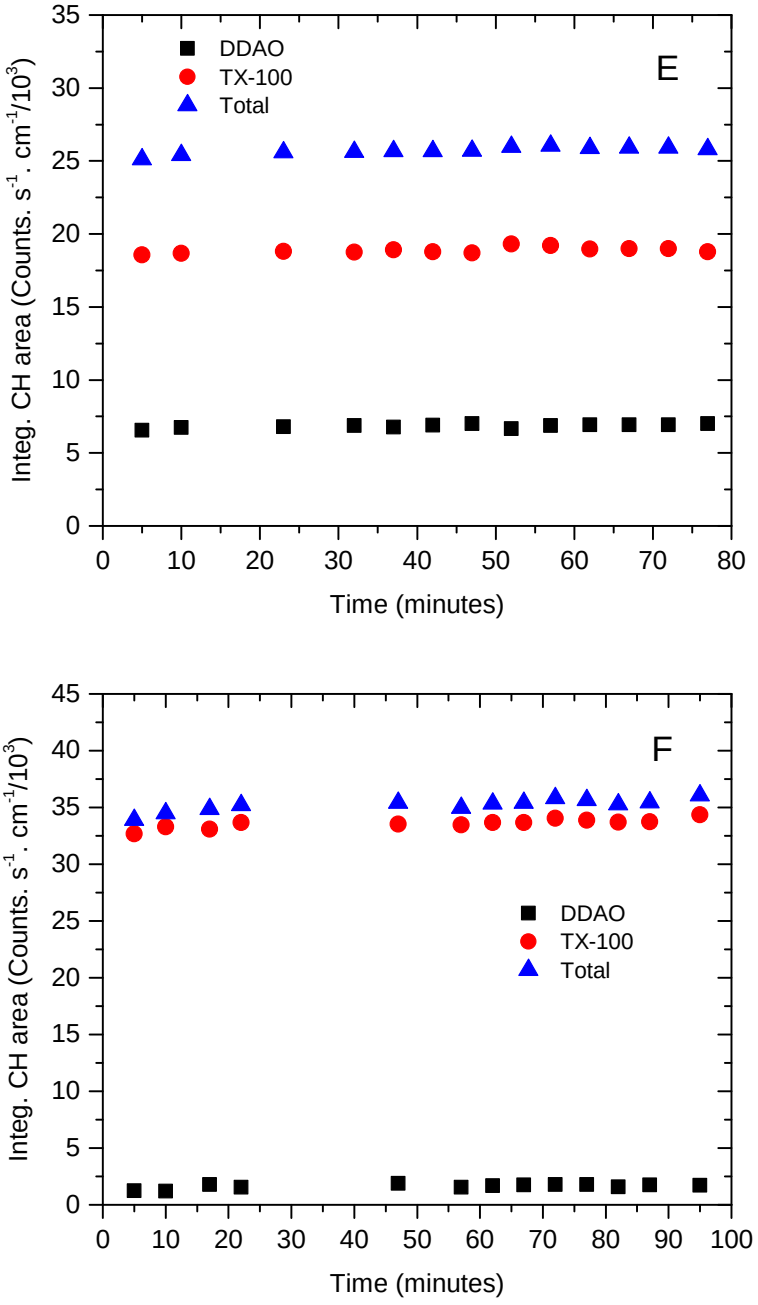

Figure 5.9. Adsorption kinetics of mixtures with two different bulk concentrations of TX-100: (E) 1.08 mM; (F) 18.98 mM. The bulk concentration of DDAO was fixed at 0.30 mM.

5.1.2 Adsorption of mixtures at higher concentration of DDAO

The above results show enhanced adsorption of TX-100 at low DDAO concentration. It would be more complete to see the effects at higher DDAO concentrations. Figure 5.10 shows some Raman spectra of DDAO and TX-100 mixtures at a DDAO bulk concentration of 1.00 mM with varied concentrations of TX-100. The mixed surfactant spectra clearly show the peak of d^+ mode of DDAO molecules at TX-100 bulk concentrations below 0.70 mM (spectrum is not shown here). The spectra in this range of TX-100 concentration also show the overlap of the r^-_{HG} peak of DDAO and the symmetric CH stretch of the aromatic ring of TX-100 in the 3020 - 3100 cm^{-1} region. Target testing revealed two main factors contributing to the mixed spectra and their component weights are given in Figure 5.11.

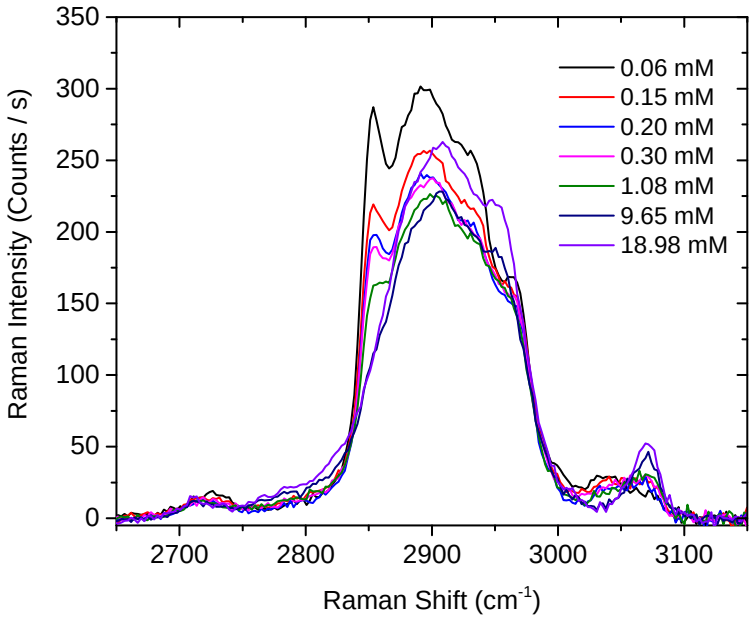

Figure 5.10. Background subtracted and baseline corrected TIR Raman spectra of DDAO and TX-100 mixtures at DDAO bulk concentration of 1.00 mM and varied concentrations of TX-100.

Figure 5.12 shows integrated CH areas of TX-100, DDAO and mixed

spectra after TFA was applied. Adsorption of DDAO is only enhanced with a TX-100 concentration smaller than 0.15 mM. When TX-100 concentrations are higher, DDAO molecules on the surface are slowly replaced by TX-100 with its adsorbed amount smaller than that of pure DDAO. The removal of DDAO from the interface results from the competitive adsorption of DDAO and TX-100 and the formation of mixed micelles in the bulk phase. Adsorption of TX-100 in the mixtures is greatly enhanced when its bulk concentration is lower than about 0.25 mM and at higher concentrations it slowly replaces DDAO molecules on the surface. The component weights of TX-100 in the mixtures were converted to surface excesses and results are shown in Figure 5.13. The surface excesses of TX-100 in its mixtures with 0.30 mM DDAO are also given in Figure 5.13 for comparison purposes. This figure reveals that adsorption of TX-100 in its mixtures with 1.00 mM DDAO is not as enhanced as that in its mixtures with 0.30 mM DDAO. This adsorption behavior is expected due to the fact that DDAO molecules have both electrostatic interactions and hydrogen bonds with the silica surface and the higher concentration of DDAO would lead to a higher number of its molecules in the adsorbed layer. A smaller concentration of DDAO would be more effective in enhancing the adsorption of TX-100.

Table 5.2. Results obtained from target testing of DDAO and TX-100 mixtures. DDAO concentration was of 1.00 mM and TX-100 concentration was varied.

Target	REP	RET	SPOIL
1	1.53	4.06	2.65
2	1.45	2.34	1.61

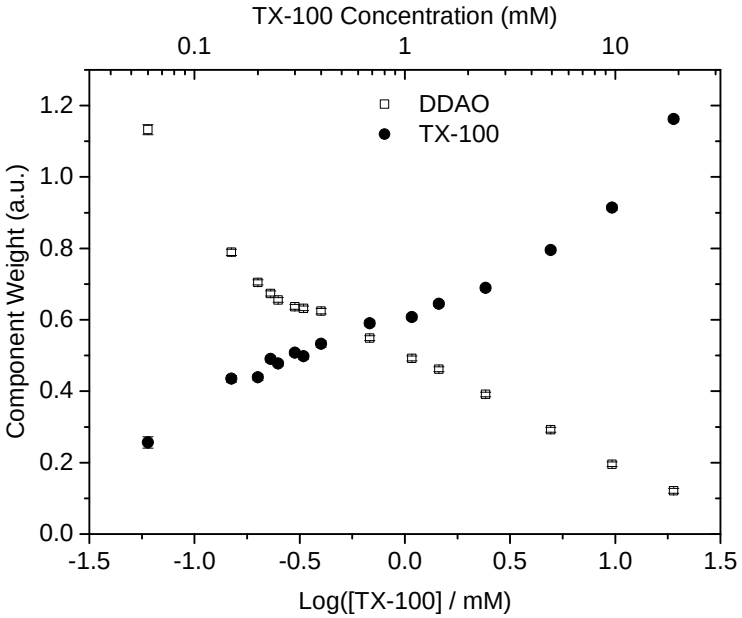

Figure 5.11. Component weights of DDAO and TX-100 in mixed surfactants. DDAO bulk concentration was 1.00 mM and TX-100 concentration was varied.

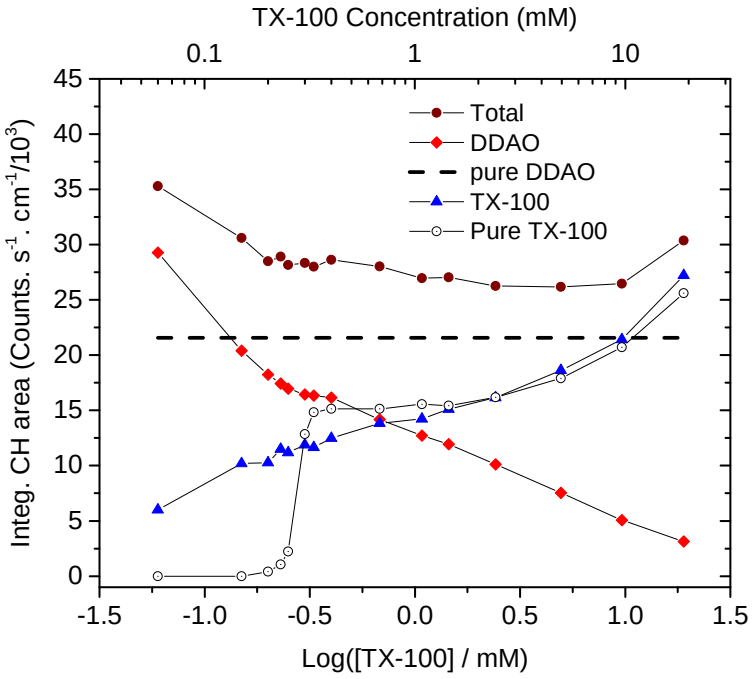

Figure 5.12. Integrated CH areas of TX-100, DDAO and mixed spectra obtained after target factor analysis and plotted as a function of log([TX-100]/mM). The integrated CH region is from 2800 to 3000 cm^{-1}. The dashed line shows integrated values of pure DDAO at the silica/water interface with a bulk concentration of 1.00 mM.

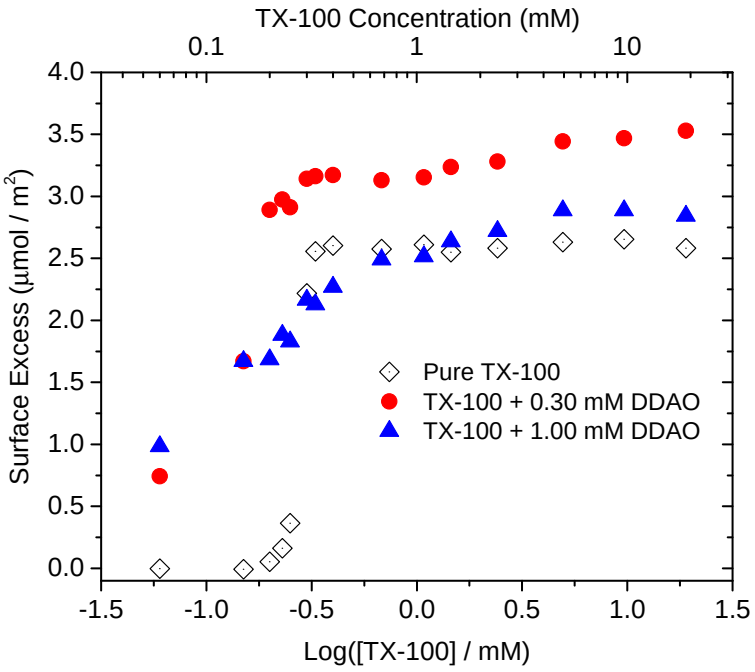

Figure 5.13. Adsorption isotherms of TX-100 in single and mixed systems as a function of log([TX-100]/mM). The isotherm here is expressed in term of surface excess. TIR Raman experiments of the mixtures were performed with two different concentrations of DDAO (0.30 mM and 1.00 mM) and varied concentrations of TX-100.

5.1.3 Adsorption mechanism

Mixed surfactants at hydrophilic solid/water interfaces have been studied using different techniques.[2;107–109] For the case of DDAO, there is only a study of its mixtures with dodecyl maltoside ($C_{12}G_2$) at the silica/water interface by an ellipsometric method.[2] This optical technique, although being sensitive to the change of adsorbed layer, only gives the total adsorbed amount at the interface without any information on contribution of single components in the adsorbed layer, which makes it difficult to propose an adsorption mechanism. It is from Figure 5.13 that for pure TX-100, at concentrations smaller than 0.15 mM adsorption of TX-100 at the interface is negligible. However, the adsorbed amount changes dramatically in the mixed surfactant at the same range of pure TX-100 concentrations. The possible mechanism for this range of TX-100 concentrations

is that DDAO molecules adsorb to the interface first and then hydrophobic interactions between alkyl chains of surfactant molecules lead to the adsorption of TX-100. The negatively charged sites on the silica surface are occupied by the protonated $DDAOH^+$ and the neutral sites are for TX-100 and nonionic DDAO. When TX-100 concentration increases, mixed surfactants can form a bilayer on the silica surface.[2] The formation of mixed micelles in the bulk solution decreases the surface concentration of DDAO and the adsorbed layer is richer in TX-100. The mixed micelles are favored by the protonated DDAO molecules due to the reduction of electrostatic repulsion between their headgroups. At very high concentrations of TX-100, the surface is almost fully occupied by TX-100 while most DDAO molecules are in the mixed micelles. The adsorption enhancement of TX-100 by the presence of DDAO in the solution can be illustrated by Figure 5.14.

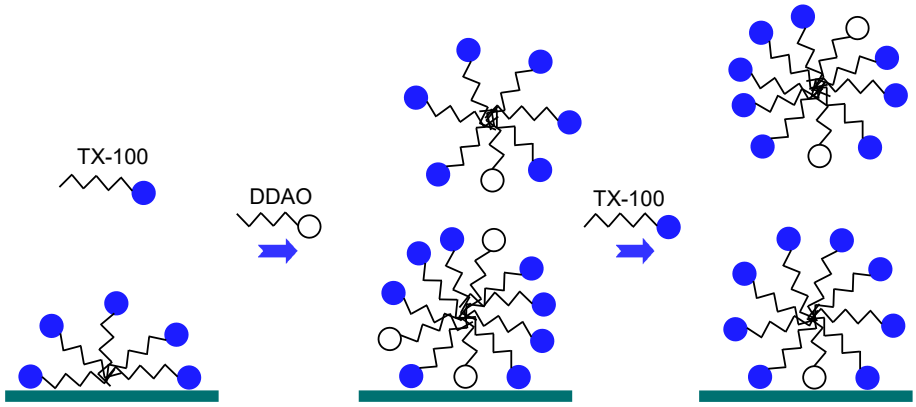

Figure 5.14. Illustration of mixed surfactants at the silica-water interface without NaCl. TX-100 and DDAO molecules are represented by surfactants with blue and red headgroups, respectively. TX-100 concentration is increased from left to right.

The addition of a very small amount of cetyltrimethylammonium bromide (CT-AB) was reported to effectively enhance the adsorption of TX-100 at the hydrophilic silica/water interface.[26] The enhancement was then attributed to the ability of CTAB at its very low concentration to alter the adsorbed layer structure of TX-100 leading to a more dense surfactant layer at the interface. The protonated form of DDAO might play a similar role as CTA^+ does in the

mixture of CTAB and TX-100.

5.2 Adsorption of mixtures with added NaCl

5.2.1 Adsorption of mixtures at low concentration of DDAO

Effects of NaCl on the adsorption of pure surfactants at the silica/water interface have been shown above. The adsorbed amount of both pure surfactants at low solution concentrations are greatly altered by the presence of 0.20 M NaCl. A small amount of DDAO is shown above to enhance the adsorption of surfactants in the mixtures. It is important to know if DDAO is still effective in enhancing the adsorption of the mixtures when NaCl is added to the solution. Figure 5.15 shows a set of background subtracted and baseline corrected TIR Raman spectra of DDAO and TX-100 mixtures at the silica/water interface with 0.20 M NaCl in the solution. The DDAO concentration was fixed at 0.30 mM while the TX-100 concentration was varied. Figure 5.16 shows a spectrum of DDAO at the silica/water interface when its bulk concentrations of DDAO and NaCl were 0.30 mM and 0.20 M, respectively. The spectra of the mixed surfactants (Figure 5.15) show a mixed shape of DDAO and TX-100 at TX-100 concentrations up to 2.50 mM. At higher concentrations of TX-100 the spectral shape is very close to that of pure TX-100 and this is an indication of the dominance of TX-100 at the interface. Target testing was performed and confirmed the contribution of two factors to the mixed spectra (Table 5.3). The mixed spectra were decomposed into single components and the component weights are given in Figure 5.17.

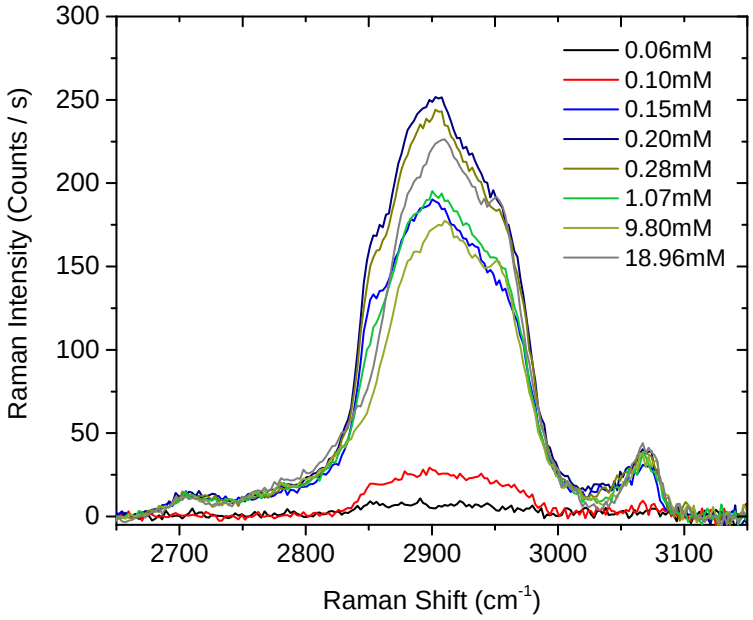

Figure 5.15. Background subtracted and baseline corrected TIR Raman spectra of DDAO and TX-100 mixtures at DDAO bulk concentration of 0.30 mM and varied concentrations of TX-100. Sodium chloride was 0.20 M in the surfactant solution.

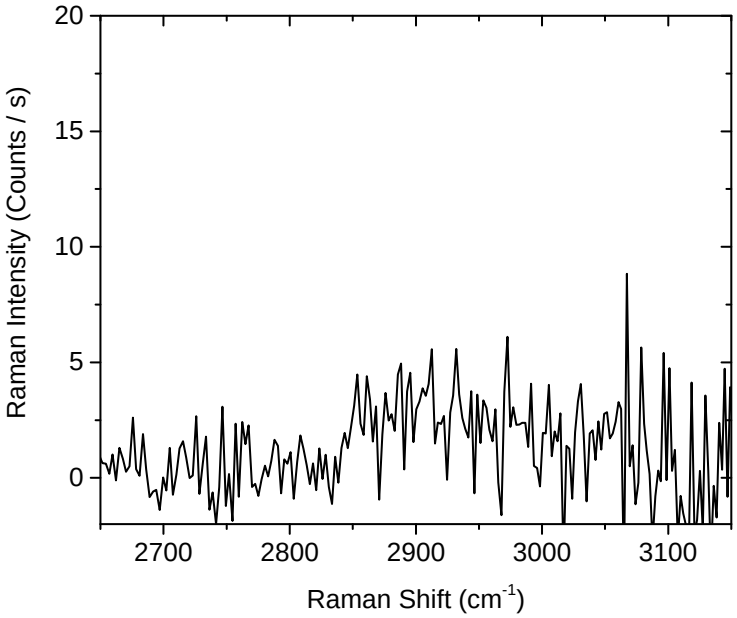

Figure 5.16. S-polarized TIR Raman spectrum of DDAO at the silica/water interface. The solution concentrations of DDAO and NaCl were 0.30 mM and 0.20 M, respectively.

Table 5.3. Results obtained from target testing of DDAO and TX-100 mixtures. DDAO concentration was 0.30 mM and TX-100 concentration was varied. The NaCl concentration in the mixtures was 0.20 M.

Target	REP	RET	SPOIL
1	3.35	5.34	1.60
2	1.70	3.08	1.82

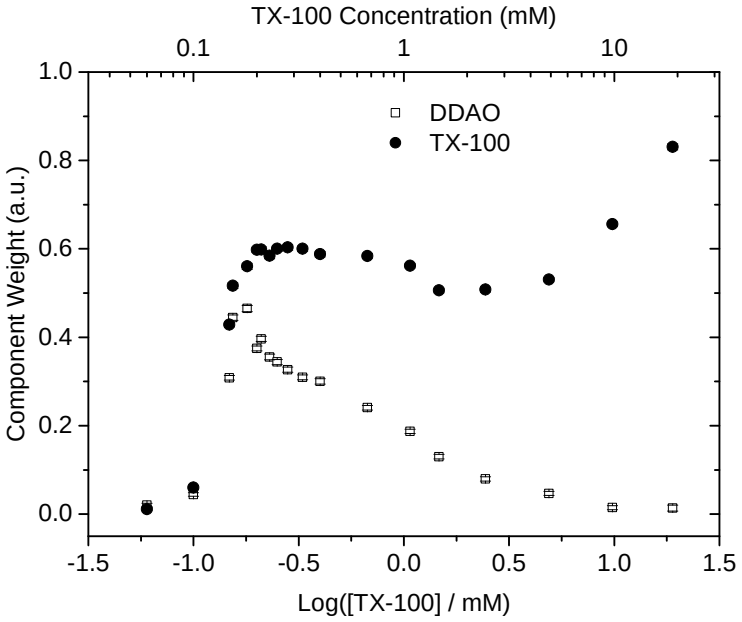

Figure 5.17. Component weights of TX-100 and DDAO in mixed surfactants plotted as functions of log([TX-100]/mM). The solution concentrations of DDAO and NaCl were 0.30 mM and 0.20 M, respectively.

5.2.2 Adsorption isotherm

From the CH stretching region (2800-3000 cm^{-1}) of the mixed spectra, DDAO and TX-100 spectra were extracted, integrated and plotted as a function of log([TX-100]/-mM) (Figure 5.18). The results of single surfactants mixed with 0.20 M NaCl are also given in the same figure. The connection lines between data points are there to indicate the trend of the Raman signals. The adsorption of DDAO from the aqueous solution with 0.20 M NaCl is so small that the adsorption of both surfactants is not greatly enhanced at TX-100 concentration smaller

than 0.10 mM. The synergistic effect when NaCl is present is reduced in comparison to that of mixtures without NaCl in the same range of TX-concentrations. This demonstrates the important role of pre-adsorbed DDAO at low TX-100 concentrations. The total adsorbed amount is maximized at TX-100 concentration of 0.18 mM, however, the maximum adsorbed value of DDAO is at 0.15 mM TX-100. When the TX-100 concentration is higher, surface DDAO molecules are replaced by TX-100 and the Raman signal of DDAO decreases until it reaches the value of pure DDAO. The formation of mixed micelles of DDAO and TX-100 keeps DDAO molecules in the bulk solution. The presence of a tiny amount of DDAO at the interface still enhances the adsorption of TX-100 until its solution concentration approaches 1.00 mM.

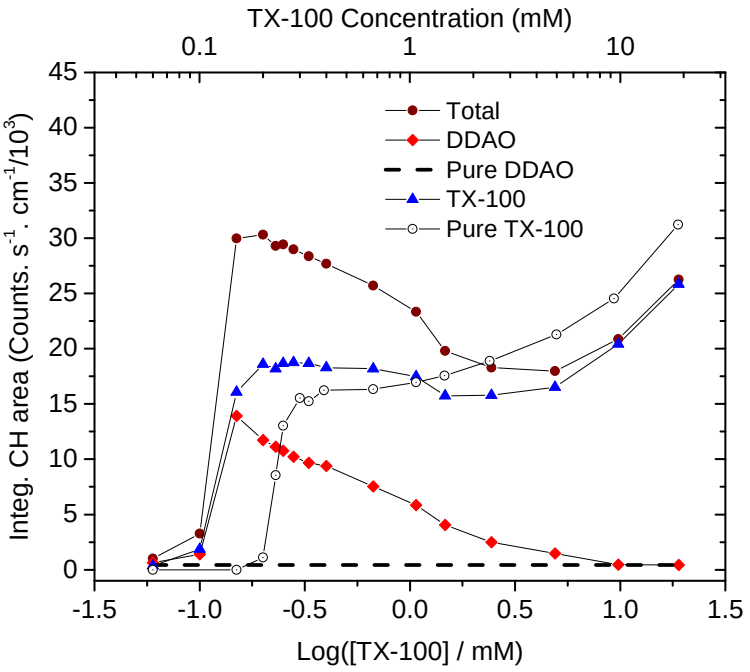

Figure 5.18. Integrated CH areas of TX-100, DDAO and mixed spectra obtained after target factor analysis and plotted as a function of log([TX-100]/mM). The integrated CH region is from 2800 to 3000 cm^{-1}. The dashed line shows integrated values of pure DDAO at the silica/water interface with a bulk concentration of 0.30 mM.

The intensities of TX-100 in the mixtures were converted into surface excesses by comparing TX-100 signals with that of pure TX-100 measured at the

same condition. The isotherms of pure TX-100 and TX-100 in the mixed surfactant system are presented in Figure 5.19. The isotherm of TX-100 is shifted to the left, which is an indication of the effects of co-surfactant and salting-out by NaCl. In the TX-100 concentration region of 0.18 - 0.7 mM the isotherm is quite constant. It is then decreased and is smaller than that of pure TX-100. The mixed micelles might alter the structure of the adsorbed layer making it less effective in covering the surface. Although the signal of DDAO at very high concentrations of TX-100 (9.80 - 19.00 mM) is small, it is due to the presence of DDAO at the interface. At a concentration of 0.30 mM, the contribution of DDAO in the bulk is negligible. The presence of 0.30 mM in the aqueous solution leads to a lower pH value in comparison to that of the solution of TX-100 and 0.20 M NaCl.

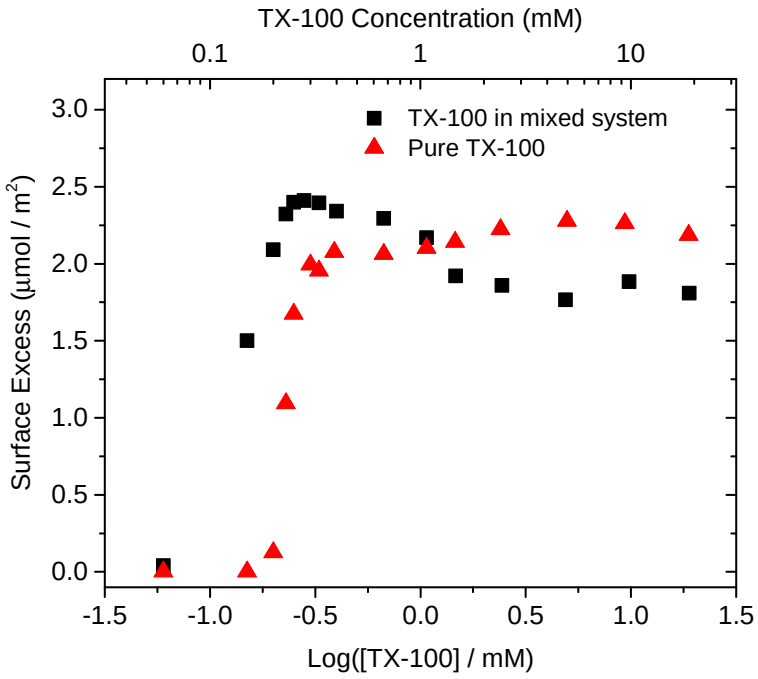

Figure 5.19. Adsorption isotherms of TX-100 in single and mixed systems as a function of log([TX-100]/mM). The isotherm here is expressed in terms of surface excess. TIR Raman experiments of the mixtures were performed with 0.30 mM DDAO and varied concentration of TX-100. The NaCl concentration was 0.20 M.

Adsorption of mixed surfactants at the solid/liquid interfaces have been

investigated using different techniques.[110;111] The use of AFM can reveal the mophorlogy of the adsorbed layer when surfactant concentration changes, however, experiments using AFM often have to perform at solution concentrations above the cmc and have to use with other methods such as depletion experiments to determine the components of the adsorption isotherm.[111]

5.2.3 Adsorption kinetics

The adsorption kinetics of mixtures at the silica/water interface is shown in Figures 5.20 - 5.21. The variations of Raman signal are presented for the mixtures as well as components. Different concentrations of TX-100 are selected to see the effects of its concentration on the kinetics. At TX-100 concentrations well below the cmc it take about 50 minutes for the adsorption process to reach an equilibrium. The changes in the signals of components might be due to the exchange of surfactants at the interface. For the mixtures with TX-100 at concentrations higher than the cmc, equilibrium is reached within 5 minutes after the injection of surfactant solution into the cell. TX-100 molecules dominate the interface and any exchange with DDAO is not noticeable.

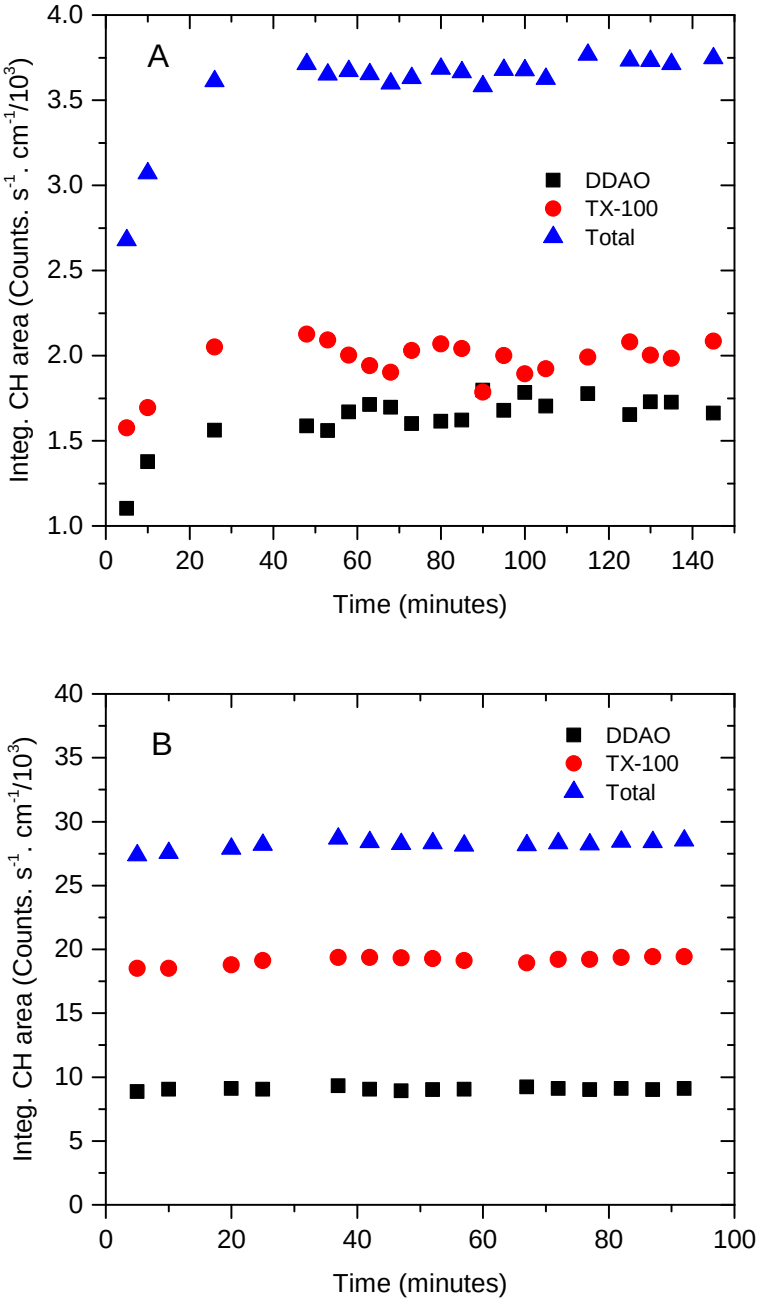

Figure 5.20. Adsorption kinetics of mixtures with two different bulk concentrations of TX-100: (A) 0.10 mM; (B) 0.40 mM. The bulk concentrations of DDAO and NaCl were fixed at 0.30 mM and 0.20 M, respectively.

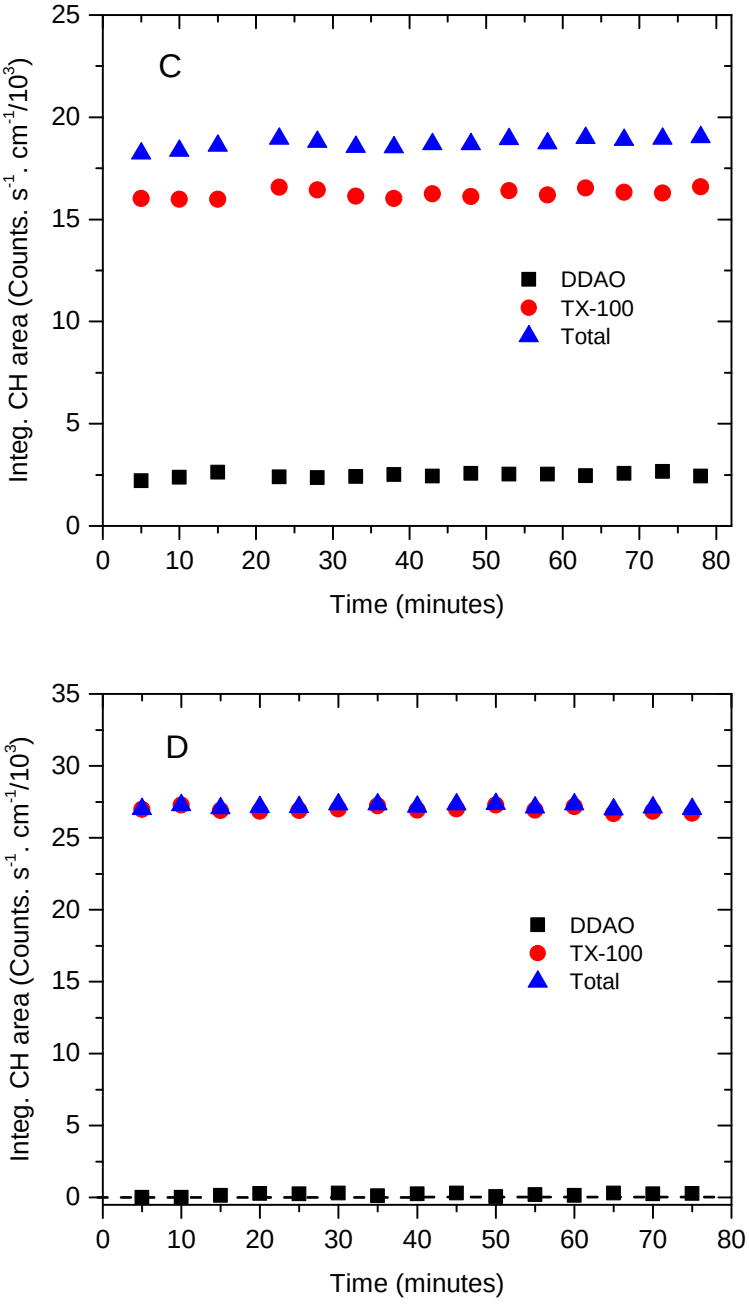

Figure 5.21. Adsorption kinetics of mixtures with two different bulk concentrations of TX-100: (C) 2.44 mM; (D) 18.96 mM. The bulk concentrations of DDAO and NaCl were fixed at 0.30 mM and 0.20 M, respectively.

5.2.4 Adsorption of mixtures at high concentrations of DDAO

A small amount of DDAO in the mixed surfactants has been shown to enhance the adsorption of TX-100 at the hydrophilic silica/water interface. It would be interesting to see the adsorption behavior of TX-100 at higher DDAO concentrations. The current study measured TIR Raman spectra of two different DDAO and TX-100 mixtures in which the TX-100 concentration was constant at 1.05 mM. The DDAO concentrations were 1.05 mM and 2.00 mM in the first and second mixtures, respectively. The concentrations were selected so that the TX-100 concentration was above its cmc in the first mixture and both DDAO and TX-100 above their cmcs in the second mixture. The mixed spectra are shown in Figure 5.22.

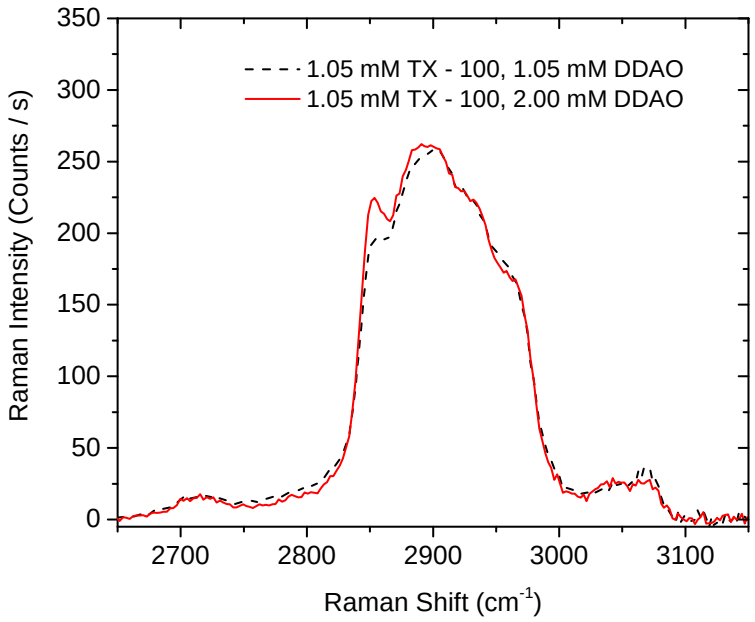

Figure 5.22. TIR Raman spectra of mixtures of TX-100 with DDAO. TX-100 bulk concentration was fixed at 1.05 mM. DDAO bulk concentrations were 1.06 mM and 2.00 mM in the first and second mixtures, respectively.

The Raman intensities of the two mixtures are very close when the DDAO

concentration in the second mixture is about 2 times of that in the first one. The obvious difference between the two spectra is the stronger signal of the symmetric methylene stretching mode (2852 cm^{-1}) of DDAO molecules. This difference indicates that the adsorbed layer is richer in DDAO molecules when DDAO concentration increases. TFA was used to decompose the mixed spectra into single components and results are given in Figure 5.23. This figure shows that the amount of TX-100 at the interface decreases with the increase of DDAO concentration. The adsorption of TX-100 is enhanced by low DDAO concentration and is reduced when the amount of DDAO in the mixed surfactants increases. DDAO molecules have stronger interactions with the silica surface than TX-100 molecules due to the electrostatic interactions and stronger hydrogen bonds. As a result, they tend to adsorb more to the interface when DDAO solution concentration increases. It is also due to the fact that at DDAO concentrations above the cmc, TX-100 is incorporated into the mixed micelles with DDAO in the bulk solution leading to a decrease of interfacial TX-100 molecules.

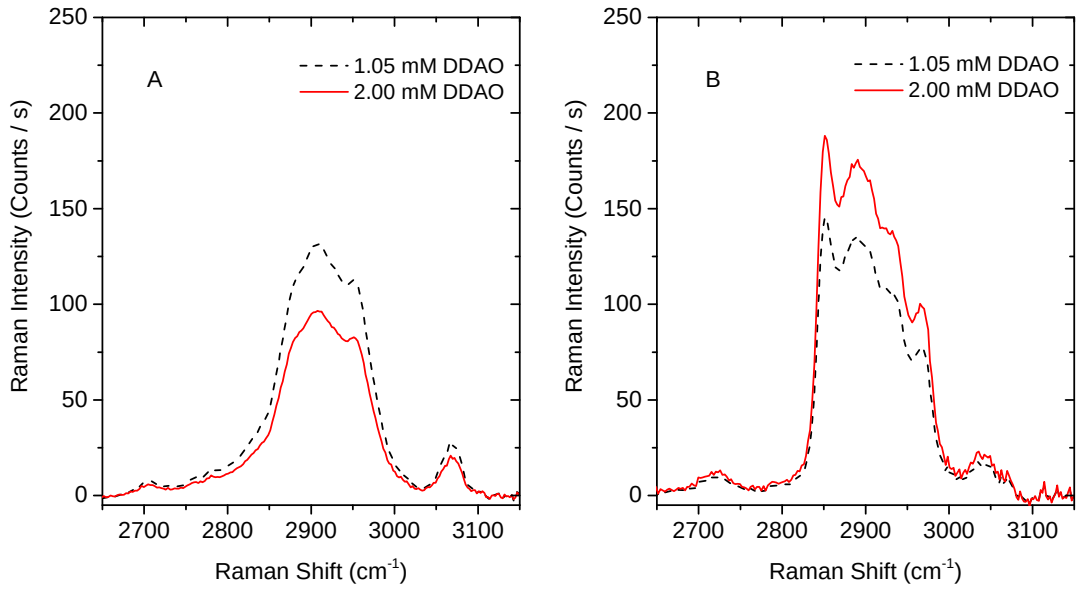

Figure 5.23. Extracted spectra of DDAO and TX-100 from mixtures of TX-100 with high DDAO concentrations. TX-100 bulk concentration was fixed at 1.05 mM. DDAO bulk concentrations were 1.06 mM and 2.00 mM in the first and second mixtures, respectively. NaCl concentration was 0.20 M.

Chapter 6

Conclusions

Total internal reflection (TIR) Raman spectroscopy and target factor analysis (TFA) have been successfully combined to study the adsorption of surfactants and mixed surfactants on the hydrophilic silica surface. The use of a linear vibrational spectroscopic technique gave rise to molecular level information such as the vibrational modes of alkyl chains of DDAO at the interface and orientation and conformation of surface molecules. TFA helped decompose data matrices of mixtures into single components and corresponding component weights (loadings).

In the study of the adsorption of pure surfactants, in the range concentrations studied, the hydrocarbon chains of pure DDAO at the silica/water interface were found to be in a liquid-like medium that is not affected significantly when 0.20 M sodium chloride is added to the surfactant solutions. The changes in conformation and orientation of the alkyl chains are also negligible when the DDAO concentration increases. The adsorption isotherms of DDAO, however, are clearly affected with the addition of 0.20 M NaCl. In comparison to the adsorption curve obtained without an added salt, sodium chloride lowers the DDAO isotherm curve when the DDAO concentration is lower than 0.70 mM due to competitive adsorption between the sodium ions and the DDAO. When

the DDAO concentration is higher than 0.70 mM, the salting-out effect caused by sodium chloride enhances the adsorption of DDAO, leading to a higher amount of DDAO at the interface. The adsorption isotherms of DDAO show maximum values at solution concentrations close to the cmcs, and are an indication of mixed adsorbed layers that have a more efficient coverage of the interface. The adsorption isotherms of TX-100 have an S shape that show a dramatic increase of adsorbed amounts for the TX-100 solutions right below the cmcs. This increase indicated the co-existence of monomers and aggregates on the silica surface.

Adsorption of both DDAO and TX-100 on the silica surface are synergistic at low concentrations and antagonistic at higher concentrations. A lower concentration of DDAO (0.30 mM in this study) is more effective in enhancing the adsorption of mixed surfactants than a higher concentration (1.00 mM in this study). Results from TIR Raman experiments with mixtures of DDAO and TX-100 show the important role of the pre-adsorbed DDAO in the adsorption of the mixtures at low concentrations. DDAO molecules were proposed to adsorb to the interface first and then promote the adsorption of TX-100 via lateral interactions between their hydrocarbon chains.

Target factor analysis has been very useful in the study of mixed surfactants. Results show that it is possible to decompose mixed spectra of two strong overlapping components as long as their pure spectra are different enough.

Appendix A

1-Hexadecyl-3-Methylimidazolium Chloride

The TIR Raman spectra of 1-hexadecyl-3-methylimidazolium chloride (Figure A.1) at the silica/water interface are given Figures A.2 and A.4. The spectra were measured with four different polarization combinations. The Raman measurements of 1-hexadecyl-3-methylimidazolium chloride were to be combined with conductivity measurements to understand the effects of the bulk solution on the surfactant adsorption at the silica/water interface.

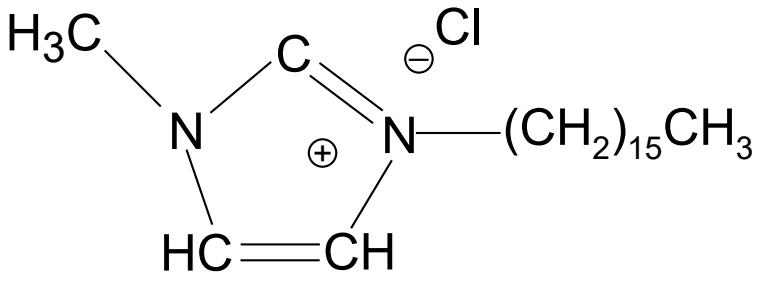

Figure A.1. 1-hexadecyl-3-methylimidazolium chloride

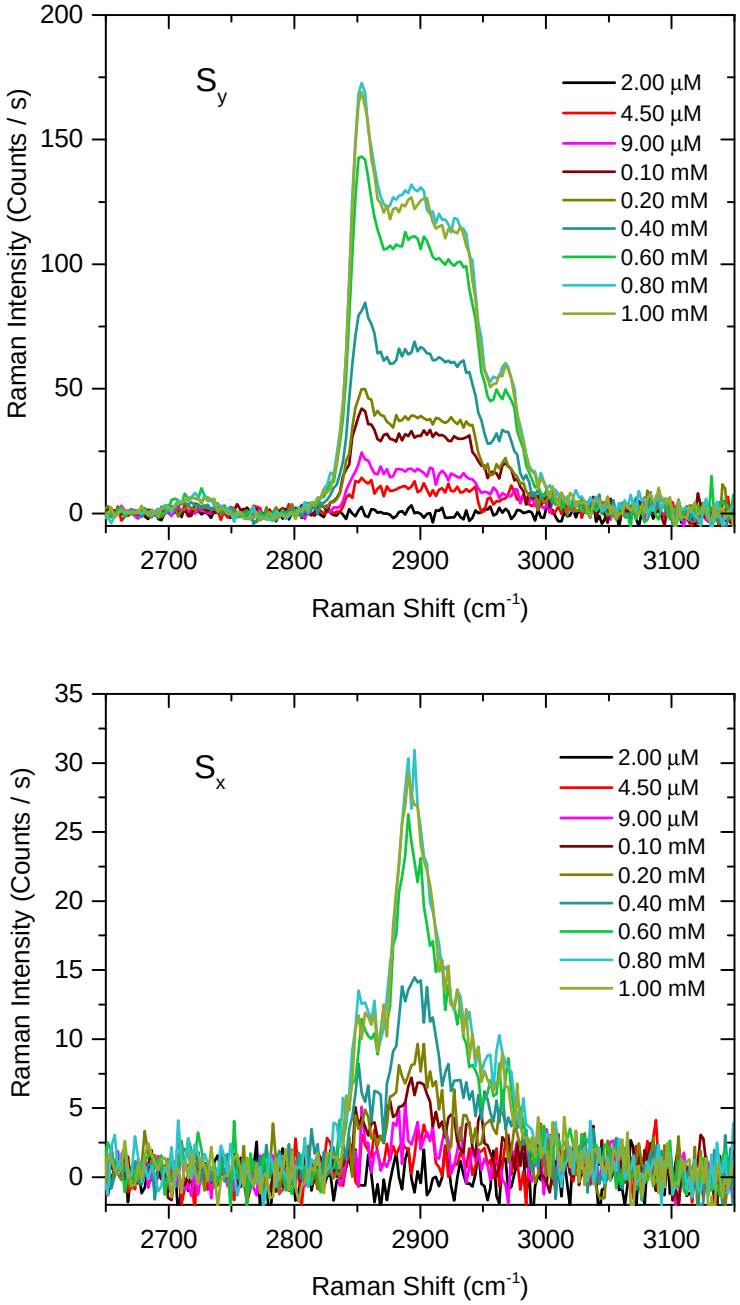

Figure A.2. Background subtracted and baseline corrected TIR Raman spectra of 1-hexadecyl-3-methylimidazolium chloride at the silica/water interface with various solution concentrations. Spectra were collected under the S_x and S_y polarization combinations.

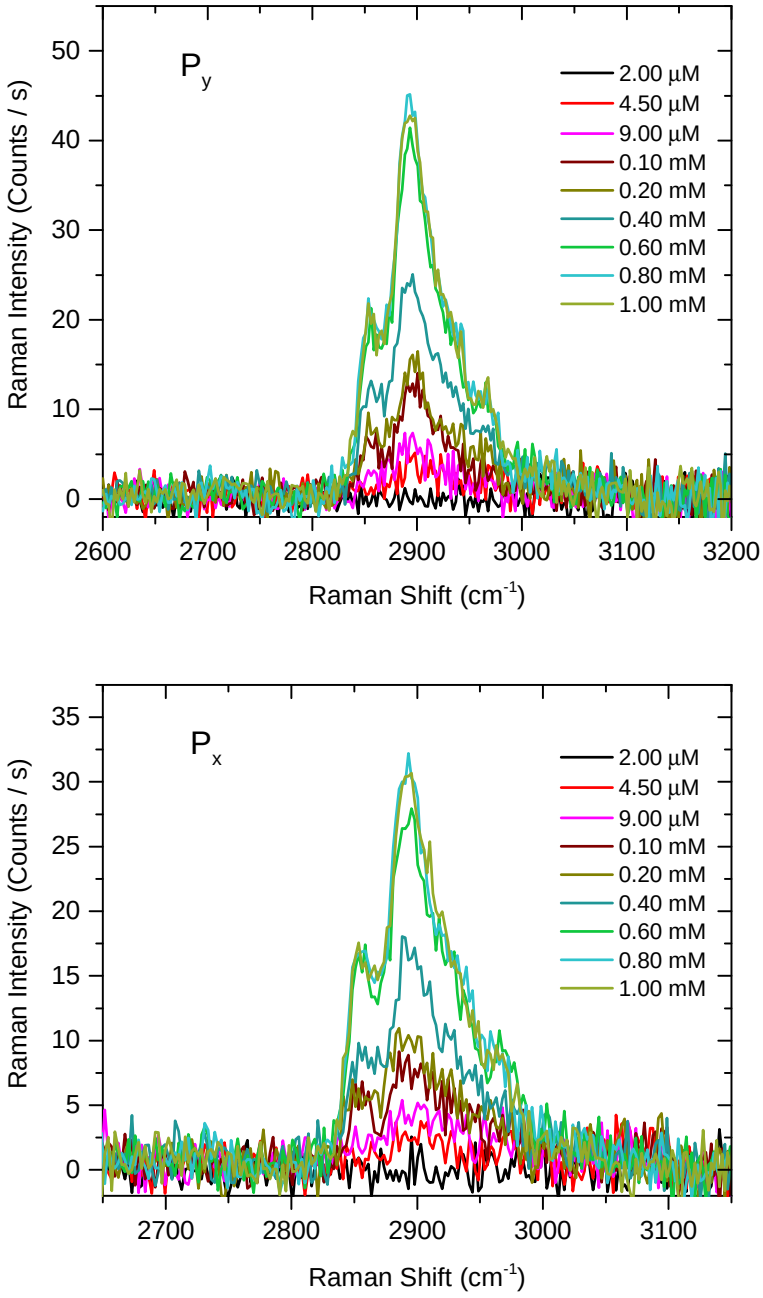

Figure A.3. Background subtracted and baseline corrected TIR Raman spectra of 1-hexadecyl-3-methylimidazolium chloride at the silica/water interface with various solution concentrations. Spectra were collected under the P_x and P_y polarization combinations.

Figure A.4 shows the adsorption isotherm of 1-hexadecyl-3-methylimidazolium chloride at the hydrophilic silica/water interface as a function of concentration. The adsorption isotherm is represented in terms of the integrated CH stretching area of Raman spectra obtained from the S_y-polarized measurements.

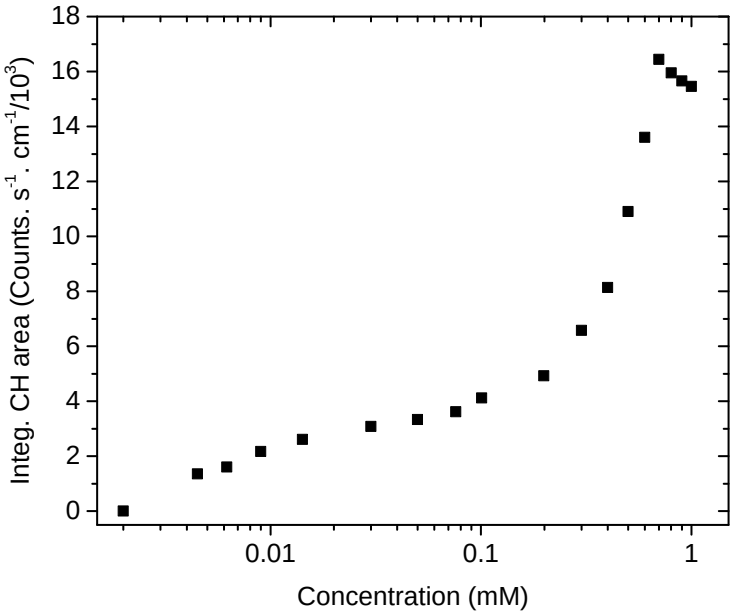

Figure A.4. Integrated CH stretching area of S_y-polarized Raman spectra of 1-hexadecyl-3-methylimidazolium chloride at the hydrophilic silica/water interface as a function of concentration.

Appendix B

Adsorption on the ITO Surface

Figure B.1 shows the cyclic voltammogram (CV) of the ITO coating on the glass surface at a scan rate of 50 mV/s. These CVs reveal that the ITO surface is polarizable in the potential range used in the study.

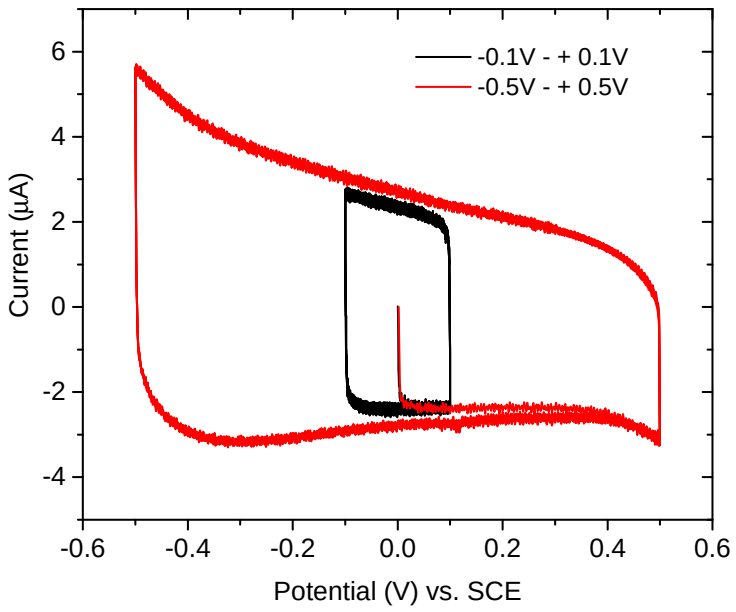

Figure B.1. Cyclic Voltammogram of the ITO coating at a scan rate of 50 mV/s. The measurements were done in 0.1 M KCl solution.

The Raman spectra of cetyl trimethylammonium bromide (CTAB) at the ITO/water interface are given in Figure B.2. The Raman measurements were performed at the open circuit potential (OCP) of the ITO coating and at -0.3 V versus the OCP. Figure B.2 shows that the C-H stretching region of the Raman spectra obtained from these two measurements are insignificantly different. Signal from CTAB was expected to be altered when an external negative potential was applied but it did not occur in these experiments. The laser beam might not have been totally reflected at the ITO/water interface so that the Raman signal was from surfactant molecules in the bulk solution. A better designed experiment would improve this kind of measurement.

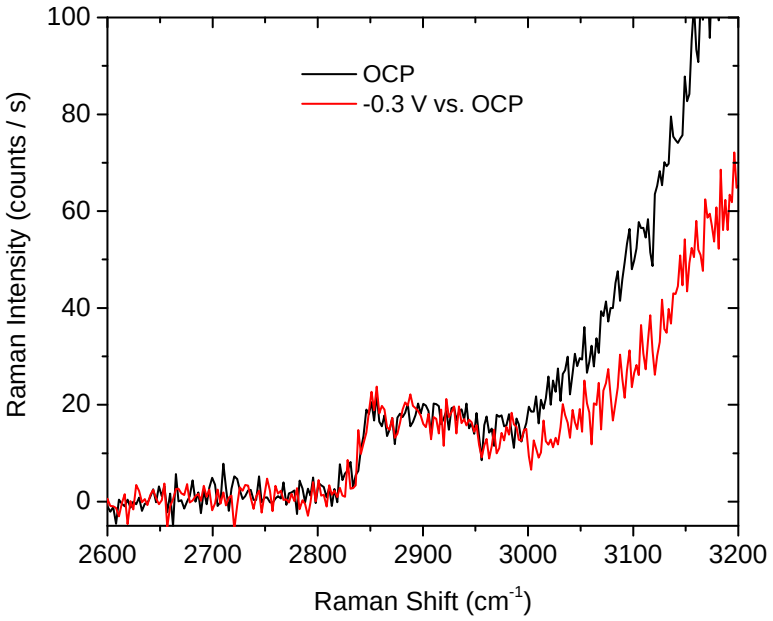

Figure B.2. The Raman spectra of cetyl trimethylammonium bromide (CTAB) at the ITO/water interface.

Bibliography

[1] Pettersson, A.; Rosenholm, J. B. Adsorption of Alkyldimethylamine and Alkyldimethylphosphine Oxides at Curved Aqueous Solution/Silica Interfaces, Studied Using Microcalorimetry. *Langmuir* **2002**, *18*, 8436-8446.

[2] Matsson, M. K.; Kronberg, B.; Claesson, P. M. Enhanced Adsorption of Alkyl Glucosides on the Silica/Water Interface by Addition of Amine Oxides. *Langmuir* **2005**, *21*, 2766-2772.

[3] Zou, Q.; Bennion, B. J.; Daggett, V.; Murphy, K. P. The Molecular Mechanism of Stabilization of Proteins by TMAO and Its Ability to Counteract the Effects of Urea. *J. Am. Chem. Soc.* **2002**, *124*, 1192-1202.

[4] Singh, S. K.; Bajpai, M.; Tyagi, V. K. Amine Oxides: a Review. *J. Oleo Sci.* **2006**, *55*, 99-119.

[5] Gerstein, T. Non-irritating Shampoo Compositions Containing Stearyl Amine Oxide. U.S. Patent 4,033,895, Jul 5, 1977.

[6] Smith, K. R.; Borland, J. E.; Corona, R. J.; Sauer, J. D. High Active Alkyldimethylamine Oxides. *J. Am. Oil Chem. Soc.* **1991**, *68*, 619-622.

[7] Crutcher, T.; Smith, K. R.; Borland, J. E.; Sauer, J. D.; Perine, J. W. Alkyldimethylamine Oxides as Synergistic Fabric Softeners *J. Am. Oil Chem. Soc.* **1992**, *69*, 682-689.

[8] Mel'nikova, Y. S.; Lindman, B. pH-Controlled DNA Condensation in the Presence of Dodecyldimethylamine Oxide. *Langmuir* **2000**, *16*, 5871-5878.

[9] Hunger, J.; Tielrooij, K. J.; Buchner, R.; Bonn, M.; Bakker, H. J. Complex Formation in Aqueous Trimethylamine-N-oxide (TMAO) Solutions. *J. Phys. Chem. B* **2012**, *116*, 4783-4795.

[10] Kocherbitov, V.; Veryazov, V.; Söderman, O. Hydration of Trimethylamine-N-oxide and of Dimethyldodecylamine-N-oxide: An ab Initio Study. *J. Mol. Struct.: THEOCHEM* **2007**, *808*, 111-118.

[11] Kawasaki, H.; Maeda, H. FT-IR Study on Hydrogen Bonds between the Headgroups of Dodecyldimethylamine Oxide Hemihydrochloride. *Langmuir* **2001**, *17*, 2278-2281.

[12] Herder, C. E.; Claesson, P. M.; Herder, P. C. Interaction between Amine Oxide Surfactant Layers Adsorbed on Mica. *J. Chem. Soc. Faraday Trans. 1* **1989**, *85*, 1933-1943.

[13] Poptoshev, E.; Claesson, P. M. Adsorption of Dimethyldodecylamine-N-oxide at the Mica-Solution Interface Studied by Ellipsometry. *Colloids Surf., A.* **2006**, *291*, 45-50.

[14] Rosen, M. J.; Kunjappu, J. T. *Surfactants and Interfacial Phenomena*, 3rd ed.; John Wiley & Sons: Hoboken, NJ, 2004.

[15] Kaimoto, H.; Shoho, K.; Sasaki, S.; Maeda H. Aggregation Numbers of Dodecyldimethylamine Oxide Micelles in Salt Solutions. *J. Phys. Chem.* **1994**, *98*, 10243-10248.

[16] Herrmann, K. W. Micellar Properties and Phase Separation in Dimethyldodecylamine Oxide-Sodium Halide-Water Systems. *J. Phys. Chem.* **1964**, *68*, 1540-1546.

[17] Zhang, H.; Dubin, P. L.; Kaplan, J. I. Potentiometric and Dynamic Light Scattering Studies of Micelles of Dimethyldodecylamine Oxide. *Langmuir* **1991**, *7*, 2103-2107.

[18] Alkorta, I.; Elguero, J. Theoretical Study of Strong Hydrogen Bonds between Neutral Molecules: The Case of Amine Oxides and Phosphine Oxides as Hydrogen Bond Acceptors. *J. Phys. Chem. A* **1999**, *103*, 272-279.

[19] Lair, V.; Bouguerra, S.; Turmine, M.; Letellier, P. Thermodynamic Study of the Protonation of Dimethyldodecylamine N-Oxide Micelles in Aqueous Solution at 298 K. Establishment of a Theoretical Relationship Linking Critical Micelle Concentrations and pH. *Langmuir* **2004**, *20*, 8490-8495.

[20] Bonincontr, A.; Cametti, C.; Marchetti, S.; Onori, G. Influence of the pH-induced Ionization on the Conformation of Dodecyldimethylamine Oxide Micelles: A Radiowave Dielectric Relaxation and Light-Scattering Study. *J. Phys. Chem. B* **2003**, *107*, 10671-10676.

[21] Kathrin, S.; Natalie, P.; Claesson, P. M.; Cosima, S. Effects of Protonation on Foaming Properties of Dodecyldimethylamine Oxide Solutions: a pH-Study. *Soft Matter* **2015**, *11*, 561-571.

[22] Malinowski, E. R. *Factor Analysis in Chemistry*, 3rd ed.; John Wiley & Sons: New York, 2002.

[23] Windsor, R.; Neivandt, D. J.; Davies, P. B. Adsorption of Sodium Dodecyl Sulfate in the Presence of Poly(ethylenimine) and Sodium Chloride Studied Using Sum Frequency Vibrational Spectroscopy. *Langmuir* **2001**, *17*, 7306-7312.

[24] Bain, C. D.; Davies, P. B.; Ward, R. N. In-Situ Sum-Frequency Spectroscopy

of Sodium Dodecyl Sulfate and Dodecanol Coadsorbed at a Hydrophobic Surface. *Langmuir* **1994**, *10*, 2060-2063.

[25] Ward, R. N.; Davies, P. B.; Bain, C. D. Coadsorption of Sodium Dodecyl Sulfate and Dodecanol at a Hydrophobic Surface. *J. Phys. Chem. B* **1997**, *101*, 1594-1601.

[26] Woods, D. A.; Petkov, J.; Bain, C. D. Surfactant Adsorption Kinetics by Total Internal Reflection Raman Spectroscopy. 2. CTAB and Triton X-100 Mixtures on Silica. *J. Phys. Chem. B* **2011**, *115*, 7353-7363.

[27] Long, J. A.; Rankin, B. M.; Ben-Amotz, D. Micelle Structure and Hydrophobic Hydration. *J. Am. Chem. Soc.* **2015**, *137*, 10809-10815.

[28] Nickolov, Z. S.; Earnshaw, J. C.; McGarvey, J. J. Total Internal Reflection Raman Spectroscopy as a Method to Study Water Structure near Langmuir-Blodgett Films. *J. Raman Spectrosc.* **1993**, *24*, 411-416.

[29] Iwamoto, R.; Ohta, K.; Miya, M.; Mima, S. Total Internal Reflection Raman Spectroscopy at the Critical Angle for Raman Measurements of Thin Films. *Appl. Spectrosc.* **1981**, *35*, 584-587.

[30] Beattie, D. A.; Larsson, M. L.; Holmgren, A. R. In Situ Total Internal Reflection Raman Spectroscopy of Surfactant Adsorption at a Mineral Surface. *Vib. Spectrosc.* **2006**, *41*, 198-204.

[31] Woods, D. A.; Bain, C. D. Total Internal Reflection Raman Spectroscopy. *Analyst* **2012**, *137*, 35-48.

[32] Ikeshoji, T.; Ono, Y.; Mizuno, T. Total Reflection Raman Spectra; Raman Scattering due to the Evanescent Wave in Total Reflection. *Appl. Opt.* **1973**, *12*, 2236-2237.

[33] Masamichi, F.; Tetsuo, O. Internal Reflection Resonance Raman Spectroscopy for Studies of Adsorbed Dye Layers at Electrode-Solution Interface. *J. Am. Chem. Soc.* **1976**, *98*, 7850-7851.

[34] Iwamoto, R.; Miya, M.; Ohta, K.; Mima, S. Total Internal Reflection Raman Spectroscopy as a New Tool for Surface Analysis. *J. Am. Chem. Soc.* **1980**, *102*, 1212-1213.

[35] Hölzer, W.; Schröter, O.; Richter, A. Raman Study on Surface Layers and Thin Films by Using Total Reflection Experiments. *J. Mol. Struct.* **1990**, *217*, 253-264.

[36] Fujiwara, K.; Watarai, H. Total Internal Reflection Resonance Raman Microspectroscopy for the Liquid/Liquid Interface. Ion-Association Adsorption of Cationic Mn(III) Porphine. *Langmuir* **2003**, *19*, 2658-2664.

[37] Takenaka, T.; Nakanaga, T. Resonance Raman Spectra of Monolayers Adsorbed at the Interface between Carbon Tetrachloride and an Aqueous Solution of a Surfactant and a Dye. *Langmuir* **1976**, *80*, 475-480.

[38] Lee, C.; Wacklin, H.; Bain, C. D. Changes in Molecular Composition and Packing during Lipid Membrane Reconstitution from Phospholipid-SurfactantMicelles. *Soft Matter* **2009**, *5*, 568-575.

[39] Lee, C.; Bain, C. D. Raman Spectra of Planar Supported Lipid Bilayers. *Biochim. Biophys. Acta* **2005**, *1711*, 59-71.

[40] Woods, D. A.; Petkov, J.; Bain, C. D. Surfactant Adsorption Kinetics by Total Internal Reflection Raman Spectroscopy. 1. Pure Surfactants on Silica. *J. Phys. Chem. B* **2011**, *115*, 7341-7352.

[41] McKee, K. J.; Smith, E. A. Development of a Scanning Angle Total Internal Reflection Raman Spectrometer. *Rev. Sci. Instrum.* **2010**, *81*, 43106.

[42] Meyer, M. W.; Nguyen, V. H. T.; Smith, E. A. Scanning Angle Raman Spectroscopy Measurements of Thin Polymer Films for Thickness and Composition Analyses. *Vib. Spectrosc.* **2013**, *65*, 94-100.

[43] Praveena, M.; Bain, C. D.; Jayaram, V.; Biswas, S. K. Total Internal Reflection (TIR) Raman Tribometer: a New Tool for In Situ Study of Friction-Induced Material Transfer. *RSC Adv.* **2013**, *3*, 5401-5411.

[44] Praveena, M.; Guha, K.; Ravishankar, A.; Biswas, S. K.; Bain, C. D.; Jayarama, V. Total Internal Reflection Raman Spectroscopy of Poly(alpha-olefin) Oils in a Lubricated Contact. *RSC Adv.* **2014**, *4*, 22205-22213.

[45] Israelachvili, J. N. *Intermolecular and Surface Forces*, Elsevier Science, 2015.

[46] Holland, P. M.; Rubingh, D. N. Non-ideal Multicomponent Mixed Micelle Model. *J. Phys. Chem* **1983**, *87*, 1984-1990.

[47] Holland, P. M. Nonideality at the Interface in Mixed Micellar Systems. *Colloids Surf.* **1986**, *19*, 171-183.

[48] Ong, S. W.; Zhao, X. L.; Eisenthal, K. B. Polarization of Water Molecules at a Charged Interface: Second Harmonic Studies of the Silica/Water Interface. *Chem. Phys. Lett.* **1992**, *191*, 327-335.

[49] Darlington, A. M.; Gibbs-Davis, J. M. Bimodal or Trimodal? The Influence of Starting pH on Site Identity and Distribution at the Low Salt Aqueous/Silica Interface. *J. Phys. Chem. C* **2015**, *119*, 16560-16567.

[50] Warring, S. L.; Beattie, D. A.; McQuillan, A. J. Surficial Siloxane-to-Silanol Interconversion during Room-Temperature Hydration/Dehydration of Amorphous Silica Films Observed by ATR-IR and TIR-Raman Spectroscopy. *Langmuir* **2016**, *32*, 1568-1576.

[51] Allen, L. H.; Matijevi, E.; Meties, L. Exchange of Na^+ for the Silanolic Protons of Silica. *J. Inorg. Nucl. Chem.* **1971**, *33*, 1293-1299.

[52] Sulpizi, M.; Gaigeot, M.-P.; Sprik, M. The Silica-Water Interface: How the Silanols Determine the Surface Acidity and Modulate the Water Properties. *J. Chem. Theory Comput.* **2012**, *8*, 1037-1047.

[53] Iler, R. K. *The Chemistry of Silica: Solubility, Polymerization, Colloid and Surface Properties and Biochemistry of Silica*, John Wiley & Sons: New York, 1979.

[54] Azam, M. S.; Weeraman, C. N.; Gibbs-Davis, J. M. Halide-Induced Cooperative Acid-Base Behavior at a Negatively Charged Interface. *J. Phys. Chem. C* **2013**, *117*, 8840-8850.

[55] Azam, M. S.; Weeraman, C. N.; Gibbs-Davis, J. M. Specific Cation Effects on the Bimodal Acid-Base Behavior of the Silica/Water Interface. *J. Phys. Chem. Lett.* **2012**, *3*, 1269-1274.

[56] Dove, P. M.; Craven, C. M. Surface Charge Density on Silica in Alkali and Alkaline Earth Chloride Electrolyte Solutions. *Geochim. Cosmochim. Acta* **2005**, *69*, 4963-4970.

[57] Pfeiffer-Laplaud, M.; Gaigeot, M.-P.; Sulpizi, M. pKa at Quartz/Electrolyte Interfaces. *J. Phys. Chem. Lett.* **2016**, *7*, 3229-3234.

[58] Pfeiffer-Laplaud, M.; Gaigeot, M.-P. Adsorption of Singly Charged Ions at the Hydroxylated (0001) α-Quartz-Water Interface. *J. Phys. Chem. C* **2016**, *120*, 4866-4880.

[59] Pfeiffer-Laplaud, M.; Gaigeot, M.-P. Electrolytes at the Hydroxylated (0001) α-quartz/water Interface: Location and Structural Effects on Interfacial Silanols by DFT-based MD. *J. Phys. Chem. C* **2016**, *120*, 14034-14047.

[60] Chorro, M.; Chorro, C.; Dolladille, O.; Partyka, S.; Zana, R. Adsorption Mechanism of Conventional and Dimeric Cationic Surfactants on Silica Surface: Effect of the State of the Surface. *J. Colloid Interface Sci.* **1999**, *210*, 134-143.

[61] Goloub, T. P.; Koopal, L. K. Adsorption of Cationic Surfactants on Silica. Comparison of Experiment and Theory. *Langmuir* **1997**, *13*, 673-681.

[62] Tyrode, E.; Rutland, M. W.; Bain, C. D. Adsorption of CTAB on Hydrophilic Silica Studied by Linear and Nonlinear Optical Spectroscopy. *J. Am. Chem. Soc.* **2008**, *130*, 17434-17445.

[63] Rennie, A. R.; Lee, E. M.; Simister, E. A.; Thomas, R. K. Structure of a Cationic Surfactant Layer at the Silica-Water Interface. *Langmuir* **1990**, *6*, 1031-1034.

[64] Fragneto, G.; Thomas, R. K.; Rennie, A. R.; Penfold, J. Neutron Reflection from Hexadecyltrimethylammonium Bromide Adsorbed on Smooth and Rough Silicon Surfaces. *Langmuir* **1996**, *12*, 6036-6043.

[65] Wängnerud, P.; Olofsson, G. Adsorption Isotherms for Cationic Surfactants on Silica Determined by In situ Ellipsometry. *J. Colloid Interface Sci.* **1992**, *153*, 392-398.

[66] Eskilsson, K.; Yaminsky, V. V. Deposition of Monolayers by Retraction from Solution: Ellipsometric Study of Cetyltrimethylammonium Bromide Adsorption at Silica-Air and Silica-Water Interfaces. *Langmuir* **1998**, *14*, 2444-2450.

[67] Torres, L. L.; Chauveau, M.; Hayes, P. L. Macromolecular Structure of Dodecyltrimethylammonium Chloride at the Silica/Water Interface Studied

by Sum Frequency Generation Spectroscopy. *J. Phys. Chem. C* **2015**, *119*, 23917-23927.

[68] Hayes, P. L.; Keeley, A. R.; Geiger, F. M. Structure of the Cetyltrimethylammonium Surfactant at Fused Silica/Aqueous Interfaces Studied by Vibrational Sum Frequency Generation. *J. Phys. Chem. B* **2010**, *114*, 4495-4502.

[69] Liu, J. F.; Min, G.; Ducker, W. A. AFM Study of Adsorption of Cationic Surfactants and Cationic Polyelectrolytes at the Silica-Water Interface. *Langmuir* **2001**, *17*, 4895-4903.

[70] Velegol, S. B.; Fleming, B. D.; Biggs, S.; Wanless, E. J.; Tilton, R. D. Counterion Effects on Hexadecyltrimethylammonium Surfactant Adsorption and Self-Assembly on Silica. *Langmuir* **2000**, *16*, 2548-2556.

[71] Atkin, R.; Craig, V. S. J.; Wanless, E. J.; Biggs, S. Mechanism of Cationic Surfactant Adsorption at the Solid-Aqueous Interface. *Adv. Colloid Interface Sci.* **2003**, *103*, 219-304.

[72] Gao, Y. Y.; Du, J. H.; Gu, T. R. Hemimicelle Formation of Cationic Surfactants at the Silica Gel-Water Interface. *J. Chem. Soc., Faraday Trans. 1* **1987**, *83*, 2671-2679.

[73] Somasundaran, P.; Fuerstenau, D. W. Mechanisms of Alkyl Sulfonate Adsorption at the Alumina-Water Interface. *J. Phys. Chem.* **1966**, *70*, 90-96.

[74] Thibaut, A.; Misselyn-Bauduin, A. M.; Grandjean, J., Broze; G.; Jérôme, R. Adsorption of an Aqueous Mixture of Surfactants on Silica. *Langmuir* **2000**, *16*, 9192-9198.

[75] Penfold, J.; Staples, E.; Tucker, I.; Thomas, R. K. Adsorption of Mixed Anionic and Nonionic Surfactants at the Hydrophilic Silicon Surface. *Langmuir* **2002**, *18*, 5755-5760.

[76] Huang, Z.; Yan, Z.; Gu, T. Mixed Adsorption of Cationic and Anionic Surfactants from Aqueous Solution on Silica Gel. *Colloids Surf.* **1989**, *36*, 353-358.

[77] Somasundaran, P.; Snell, E. D.; Fu, E.; Xu, Q. Effect of Adsorption of Non-ionic Surfactant and Non-ionic-Anionic Surfactant Mixtures on Silica-Liquid Interfacial Properties. *Colloids Surf.* **1992**, *63*, 49-54.

[78] Singh, S. K.; Notley, S. M. Adsorption of Nonionic Surfactants (CnEm) at the Silica-Water and Cellulose-Water Interface. *J. Phys. Chem. B* **2010**, *114*, 14977-14982.

[79] Gu, T.; Zhu, B.-Y. The S-type Isotherm Equation for Adsorption of Non-ionic Surfactants at the Silica Gel-Water Interface. *Colloids Surf.* **1990**, *44*, 81-87.

[80] Tiberg, F.; Jonsson, B.; Lindman, B. Ellipsometry Studies of the Self-Assembly of Nonionic Surfactants at the Silica-Water Interface: Kinetic Aspects. *Langmuir* **1994**, *10*, 3714-3722.

[81] Novotny, L.; Hecht, B. *Principles of Nano-optics*, 1st ed.; Cambridge University Press: Cambridge, England, 2006.

[82] Delahay, P.; Tobias, C. W. *Advances in Electrochemistry and Electrochemical Engineering*, Vol. 9; John Wiley & Sons: New York, 1973.

[83] Long, D. A. *The Raman Effect: A Unified Treatment of the Theory of Raman Scattering by Molecules*, 1st ed.; Wiley Online Library: New York, 2002.

[84] Ferraro, J. R. *Introductory Raman Spectroscopy*, Elsevier Science, 2003.

[85] Press, W. H.; Teukolsky, S. A.; Vetterling, W. T.; Flannery, B. P. *Numerical Recipes: The Art of Scientific Computing*, 3rd ed.; Cambridge University Press: New York, 2007.

[86] Curwen, T. D.; Warner, J. A.; Bain, C. D.; Compton, R. G.; Eve, J. K. Adsorption Kinetics in a Dual-Inlet Channel Flow Cell: I. Cetyl Pyridinium Chloride on Hydrophilic Silica. *J. Phys. Chem. C* **2007**, *111*, 12289-12304.

[87] Grenoble, Z. Study of the Adsorption Mechanisms of Surface Active Agents at the Silica-Water Interface by Total Internal Reflection Raman Spectroscopy. Ph.D. Dissertation, University of Houston, Houston, TX, 2012.

[88] ASTM Standard E1840-96, Standard Guide for Raman Shift Standards for Spectrometer Calibration, ASTM International (2014).

[89] Felten, J.; Hall, H.; Jaumot, J.; Tauler, R.; de Juan, A.; Gorzsás, A. Vibrational Spectroscopic Image Analysis of Biological Material Using Multivariate Curve Resolution-Alternating Least Squares (MCR-ALS). *Nat. Protocols* **2015**, *10*, 217-240.

[90] Eilers, P. H. C. Parametric Time Warping. *Anal. Chem.* **2004**, 76, 404-411.

[91] Woods, B. L.; Walker, R. A. pH Effects on Molecular Adsorption and Solvation of p-Nitrophenol at Silica/Aqueous Interfaces. *J. Phys. Chem. A* **2013**, *117*, 6224-6233.

[92] Sharma, B. G.; Basu, S.; Sharma, M. M. Characterization of Adsorbed Ionic Surfactants on a Mica Substrate. *Langmuir* **1996**, *12*, 6506-6512.

[93] Patrick, H. N.; Warr, G. G.; Manne, S.; Aksay, I. A. Self-Assembly Structures of Nonionic Surfactants at Graphite/Solution Interfaces. *Langmuir* **1997**, *13*, 4349-4356.

[94] Somasundaran, P.; Healy, T. W.; Fuerstenau, D. W. Surfactant Adsorption at the Solid-Liquid Interface-Dependence of Mechanism on Chain Length. *J. Phys. Chem.* **1964**, *68*, 3562-3566.

[95] Hillebrandt, H.; Tanaka, M. Electrochemical Characterization of Self-Assembled Alkylsiloxane Monolayers on IndiumTin Oxide (ITO) Semiconductor Electrodes. *J. Phys. Chem. B* **2001**, *105*, 4270-4276.

[96] Inoue, T.; Ebina, H.; Dong, B.; Zheng, L. Electrical Conductivity Study on Micelle Formation of Long-Chain Imidazolium Ionic Liquids in Aqueous Solution. *J. Colloid Interface Sci.* **2007**, *314*, 236-241.

[97] Grenoble, Z.; Baldelli, S. Adsorption of the Cationic Surfactant Benzyldimethylhexadecylammonium Chloride at the Silica-Water Interface and Metal Salt Effects on the Adsorption Kinetics. *J. Phys. Chem. B* **2013**, *117*, 259-272.

[98] Woods, D. A.; Petkov, J.; Bain, C. D. Surfactant Adsorption by Total Internal Reflection Raman Spectroscopy. Part III: d Asorption onto Cellulose. *Colloids Surf A Physicochem Eng Asp.* **2011**, *391*, 10-18.

[99] Woods, D. A.; Bain, C. D. Total Internal Reflection Spectroscopy for Studying Soft Matter. *Soft Matter.* **2014**, *10*, 1071-1096.

[100] Snyder, R. G.; Strauss, H. L.; Elliger, C. A. Carbon-Hydrogen Stretching Modes and the Structure of n-Alkyl Chains. 1. Long, Disordered Chains. *J. Phys. Chem.* **1982**, *86*, 5145-5150.

[101] Snyder, R. G.; Hsu, S. L.; Krim, S. Vibrational Spectra in the C-H Stretching Region and the Structure of the Polymethylene Chain. *Spectrochim. Acta, Part A* **1978**, *34A*, 395-406.

[102] Gaber, B. P.; Peticolas, W. L. On the Quantitative Interpretation of Biomembrane Structure by Raman Spectroscopy. *Biochim. Biophys. Acta, Biomembr.* **1977**, *465*, 260-274.

[103] Herrmann, K. W. Non-ionic-Cationic Micellar Properties of Dimethyldodecylamine Oxide. *J. Phys. Chem.* **1962**, *66*, 295-300.

[104] Maeda, M.; Muroi, S.; Kakehashi, R. Effects of Ionic Strength on the Critical Micelle Concentration and the Surface Excess of Dodecyldimethylamine Oxide. *J. Phys. Chem. B* **1997**, *101*, 7378-7382.

[105] de Keizer, A.; Bohmer, M. R.; Mehrian, T.; Koopal, L. Adsorption of Organic Ions at the Solid-Electrolyte Interface. Interpretation of Common Intersection Points. *Colloids Surf.* **1990**, *51*, 339-357.

[106] Molina-Bolivar, J. A.; Aguiar, J.; Ruiz, C. C. Growth and Hydration Of Triton X-100 Micelles In Monovalent Alkali Salts: A Light Scattering Study. *J. Phys. Chem. B.* **2002**, *106*, 870-877.

[107] Penfold, J.; Staples, E. J.; Tucker, I.; Thomas, R. K. Adsorption of Mixed Cationic and Nonionic Surfactants at the Hydrophilic Silicon Surface from Aqueous Solution: The Effect of Solution Composition and Concentration. *Langmuir* **2000**, *16*, 8879-8883.

[108] Huang, Z.; Gu, T. Mixed Adsorption of Nonionic and Cationic Surfactants on Silica Gel and Methylated Silica Gel. *Colloids Surf.* **1987**, *28*, 159-168.

[109] Soboleva, O. A.; Yaroslavtsev, A. A.; Badun, G. A.; Summ, B. D. Mixed Adsorption Layers of Nonionic and Cationic Surfactants on Quartz. *Colloid J.* **2004**, *66*, 470-476.

[110] Nordstierna, L.; Furo, I.; Stilbs, P. Mixed Adsorption of Fluorinated and Hydrogenated Surfactants. *Langmuir* **2006**, 22, 7969-7974.

[111] Blom, A.; Warr, G. G. Structure and Composition of Cationic-Nonionic Surfactant Mixed Adsorbed Layers on Mica. *Langmuir* **2006**, *22*, 6787-6795.

[112] Hecht, E. *Optics*, 2nd ed.; Addison-Wesley, 1987.

[113] Born, M.; Wolf, E. *Principles of Optics*, 6th ed.; Pergamon Press, 1980.